

***Bi* and it's Chalcogenides for All Solid State *Li*- Ion Batteries**

Ph.D. Thesis

KM. POOJA KUMARI

2015RPY9005



DEPARTMENT OF PHYSICS

MALAVIYA NATIONAL INSTITUTE OF TECHNOLOGY JAIPUR, INDIA

November 2019

***Bi* and it's Chalcogenides for All Solid State *Li*- Ion Batteries**

Submitted in

fulfillment of the requirements for the degree of

Doctor of Philosophy

by

KM. POOJA KUMARI

ID: 2015RPY9005

Under the Supervision of

Dr. Manoj Kumar
Supervisor
MNIT Jaipur, INDIA

Dr. Ankur Jain
External Supervisor
Hiroshima University, JAPAN



DEPARTMENT OF PHYSICS

MALAVIYA NATIONAL INSTITUTE OF TECHNOLOGY JAIPUR, INDIA

November 2019

This thesis is dedicated to my family for their unconditional love and motivation.

DECLARATION

I, **Km. Pooja Kumari**, declare that this thesis titled, “***Bi and it’s Chalcogenides for All Solid State Li-Ion Batteries***” and the work presented in it, are my own. I confirm that:

- This work was done wholly or mainly while in candidature for a research degree at this university.
- Where any part of this thesis has previously been submitted for a degree or any other qualification at this university or any other institution, this has been clearly stated.
- Where I have consulted the published work of others, this is always clearly attributed.
- Where I have quoted from the work of others, the source is always given. With the exception of such quotations, this thesis is entirely my own work.
- I have acknowledged all main sources of help.
- Where the thesis is based on work done by myself, jointly with others, I have made clear exactly what was done by others and what I have contributed myself.

Date:

KM. POOJA KUMARI
(2015RPY9005)

CERTIFICATE

This is to certify that the thesis entitled “***Bi and it’s Chalcogenides for All Solid State Li-Ion Batteries***” being submitted by **Km. Pooja Kumari (2015RPY9005)** is a bonafide research work carried out under our supervision and guidance in fulfillment of the requirement for the award of the degree of **Doctor of Philosophy** in the Department of Physics, Malaviya National Institute of Technology, Jaipur, India. The matter embodied in this thesis is original and has not been submitted to any other University or Institute for the award of any other degree.

Dr. Ankur Jain (External Supervisor)

Associate Professor

Dept. of Natural Science Center

for Basic Research and Development

Hiroshima University, JAPAN

Dr. Manoj Kumar (Supervisor)

Assistant Professor

Department of Physics

MNIT Jaipur, INDIA

Place: Jaipur

Date:

ACKNOWLEDGMENT

“The power of God is with you at all times; through the activities of mind, senses, breathing, and emotions; and is constantly doing all the work using you as a mere instrument.” - (Bhagavad Gita).

First of all, I would like to express my thanks and gratitude to the Almighty, the most beneficent and merciful who granted me health, ability, and strength for successful completion of this venture, which helped me to overcome the troubles and difficulties with vigor and vitality.

I am highly indebted and hence would like to express my sincere gratitude to my supervisor **Dr. Manoj Kumar** (Assistant Professor, Department of Physics, Malaviya National Institute of Technology Jaipur, INDIA) who enlightened my way to complete this work. I feel blessed to have the opportunity to work and learn under his guidance. He is not only an outstanding scientist but above all, a great human being. As a mentor, he knew exactly when to give me the freedom to pursue a new avenue of research, when to cheer me up and exactly how to provide motivate and constructive criticism. It is my pleasant opportunity to place my sincere and warmest thanks to my external joint supervisor **Dr. Ankur Jain** (Associate Professor, Natural Science Centre for Basic Research and Development, Hiroshima University, JAPAN) for his endless support, endurance in guiding me and encouraging me throughout during the entire course of the study. He is a great human being; during my Ph.D. journey, he was like a guardian for me.

I am very thankful to Dr. Kamalendra Awasthi (Assistant Professor, Department of Physics, Malaviya National Institute of Technology Jaipur, INDIA) for his valuable suggestions, constructive criticism, and support throughout the work. I want to express my special thanks to Mrs. Sarika Kashyap, Dr. Shivani Agarwal, and Dr. Anjali Awasthi for their continuous help and moral support throughout my research work. I wish to express my sincere gratitude to Prof. Takayuki Ichikawa (Professor, Graduate School of Engineering, Hiroshima University, JAPAN) for his kind response to my queries and problems faced during my experimental work and in data analysis.

It is my privilege to acknowledge all the faculty members of the Department of Physics, MNIT Jaipur for their continuous support and encouragement. I extend my sincere thanks to

my DREC members for their constant help and permitting me to carry out research activity within or outside the department. Their valuable and critical suggestions were a constant source of encouragement through the entire course of this work. I am also thankful to staff members of the Department of Physics, Mr. Khem Singh, Mr. Firoz Khan, Mr. Ramkishor, Mr. Sunil Kumar, and Mr. Ritesh for their support to make the departmental activities easy and cheerful. I am also thankful to all office and technical staff for their valuable help and support.

I express my heartiest thanks to my seniors Dr. Yogita Kumari, Dr. Lokesh Kumar Jangir, Dr. Anil Kumar, Dr. Shushant Kumar Singh, and Dr. Sonalika Agarwal, who always show me a bright path in the dark side of this study. I am also thankful to my colleagues and my lab mates Anoop MD, Khushboo Sharma, Jyoti Yadav, Dr. Sandeep Gupta, Dr. Rini Singh, Dr. Rajesh Jangir, Prashant Sharma, Nisha Yadav, Sanjay Kumar, Nishel Saini, Rahul Kumar, Priyanka, Himanshu Agarwal, Department of Physics, MNIT Jaipur for their co-operation and making this journey memorable. Pratibha Pal (Research Scholar, Hiroshima University, Japan), deserve for a special thank for helping me for the research work and always available with a solution to my problems. I am thankful to my friends Ranjeet Choudhary, Renu Dhayal, Bulbul Jha, and Dayanand Singh, who gave me a lot of moral support during this journey. I convey my thanks and regards to all members of High-Pressure Physics Lab, Soft Materials Lab MNIT Jaipur, and Advanced Material Science Lab (Hiroshima University, Japan) for insightful, productive, and enjoyable environment provided by them. I am in loss of literary power to express my gratitude to one by one, but they all helped me during my work.

During this work, I visited various research labs, attended workshops, conferences, symposia, and seminars, and came in touch with academicians, scientists, and researchers. I learned many things from them. It is impossible for me to list them. I acknowledge and thank them for the impact they had on my lessons in both science and life.

My deepest sense of gratitude goes to my parents Mr. Yashpal Singh and Mrs. Munesh Devi who were always there during my ups and downs, for their unending support, selfless love and affection, never-ending patience and constant encouragement. I would also like to thank my all teachers, relatives, and well-wishers who supported me by prayers and kindness.

I would like to express my deep and sincere obligations to my elder brother Vinit Malik who deserves a special word of thanks, without whom it would have been almost impossible for

me to pursue and complete this work successfully. The moral support and encouragement provided by my younger brother Amit Malik in countless ways will always be appreciated by me.

This thesis is the end of my journey of obtaining my Ph.D. degree. I have not traveled in a vacuum on this journey. This thesis has been kept on track and been through to completion with the support and encouragement of numerous people, including my teachers, family, well-wishers, friends, and colleagues. At the end of my thesis, I would like to thank all those people who made this thesis possible and unforgettable experience for me.

Date:

Pooja Kumari

Abstract

The current study aimed to fabricate an all solid-state *Li*-ion battery with a highly efficient anode and highly conducting solid electrolyte. A high-performance rechargeable *Li*-ion battery with human safety and long cycle life is significantly required with the rapid progress of information devices like as cell phones and portable electronic devices. *Li*-ion batteries have been accounted for as the most effective and empirical technology as a power source for small electronic/hybrid devices due to their high energy density, high rate capability, flexible design, and long lifespan. The high energy density of a battery essentially depends on the electronic structure of the negative and positive electrode materials. Furthermore, with the expeditious improvements of electronics and an increasing tendency of renewable energy, improved electrode materials for LIBs are required to fulfill the rising demand for larger gravimetric / volumetric capacity, higher energy density, and better cycle performance. To achieve the goals, many efforts have been devoted to the fabrication of several materials for LIB electrodes. At present, all solid state batteries are evolving rapidly because of the volatile and flammable nature of liquid electrolytes, which is one of the critical factors resulting in the safety issues of LIBs. All solid-state battery replace the flammable organic liquid electrolytes with a suitable solid-state electrolyte and allow safe operation.

To improve the energy density and cyclability of *Li*-ion battery, commercial bulk as well as nano *Bi* and *Bi*-based material (Bi_2X_3) were used as anode materials in all-solid-state *Li*-ion battery, since they possess high energy density and high *Li* storage capacity. Although a huge number of solid-state electrolytes have been explored, LiBH_4 has been investigated very intensively due to its remarkably high Li^+ conductivity in the order of 10^{-3} Scm^{-1} for its high-temperature phase around 120°C . The outline of the chapters are as follows:

All the research work has been compiled in 7 chapters. Chapter 1 presents the introduction of rechargeable batteries/LIBs and their challenges. Based on the challenges, all the objectives of the thesis were also sketched in chapter 1. Chapter 2 includes the literature review about the electrodes and electrolytes used in LIBs. All the methods and materials adopted for the synthesis of Bi_2X_3 nanostructures (nanoflowers, nanosheets, nanoparticles, and nanorods), preparation of anode composite material, and fabrication of all solid-state LIB are covered in chapter 3. Chapter 4 describes the electrochemical performance of *Bi* as an anode in all solid-state LIBs, having LiBH_4 as a solid electrolyte. As compare to *Bi*-based

anode material, an improved galvanostatic and volumetric capacity was obtained in case of bulk Bi_2X_3 , which is explained in chapter 5. A further enhancement in the electrochemical performance could be achieved by using nanostructured composite anode which is discussed in chapter 6. At last, the seventh chapter presents the overall conclusion of this work and lists some new dimensions to think over.

CONTENTS

DECLARATION	
CERTIFICATE	
ACKNOWLEDGEMENT	
ABSTRACT	
CONTENTS	
LIST OF FIGURES	
LIST OF TABLES	
LIST OF ABBREVIATIONS	

Chapter-1

Introduction

1.1	General Introduction	1
1.2	Batteries	3
1.2.1	Primary Battery	4
1.2.2	Secondary Battery	4
1.3	<i>Li</i> -ion Battery	5
1.4	Major components of LIBs	8
1.4.1	Anode	8
1.4.1.1	Carbon-based anodes	9
1.4.1.2	Silicon-based anodes	9
1.4.1.3	Bismuth-based anodes	10
1.4.2	Cathodes	12
1.4.3	Electrolyte	12
1.5	The motivation of the research work	15
1.6	Objectives of the Thesis	16

Chapter-2

Literature Review

2.1	Introduction	17
2.2	<i>Bi</i> -based anode	18

2.3 Bismuth chalcogenides Bi_2X_3 ($\text{X} = \text{S}, \text{Se}, \& \text{Te}$) based anode	20
2.3.1 Bi_2S_3 based anode	20
2.3.2 Bi_2Se_3 based anode	21
2.3.3 Bi_2Te_3 based anode	23
2.4 LiBH_4 as a solid electrolyte in all-solid-state LIBs	24

Chapter-3

Materials and Methods

3.1 Introduction	27
3.2 Materials	27
3.3 Methods to synthesized the nanostructured materials	28
3.3.1 Hydrothermal method	29
3.3.2 Solvothermal method	30
3.4 Synthesis of Bi_2X_3 ($\text{X} = \text{S}, \text{Se}, \& \text{Te}$) nanostructures	30
3.4.1 Bi_2S_3 nanoflowers	30
3.4.2 Bi_2Se_3 mixed morphology (nanoparticles & nanosheets)	31
3.4.3 Bi_2Te_3 nanorods	32
3.5 Characterization techniques	33
3.5.1 Scanning Electron Microscopy (SEM)	33
3.5.2 Transmission Electron Microscopy (TEM)	35
3.5.3 X-ray Diffraction Spectroscopy (XRD)	37
3.6 All solid state <i>Li</i> -ion Battery fabrication	39
3.6.1 Preparation of Negative Electrode (Anode)	39
3.6.2 Fabrication of half coin cell	40
3.7 Electrochemical Characterizations	41
3.7.1 Cyclic Voltammetry (CV)	41
3.7.2 Galvanostatic discharge - charge experiments	43
3.8 Summary	45

Chapter-4

Bismuth as a Promising Anode for *Li*-ion Batteries

4.1	Introduction	47
4.2	Cyclic voltammetry	48
4.3	Galvanostatic discharge/charge	49
4.4	Mechanism of lithiation/delithiation of <i>Bi</i> -anode in all-solid-state <i>Li</i> -ion battery	50
4.5	Cyclic stability measurements	52
4.6	Morphological investigations of <i>Bi</i> -anode	54
4.7	Summary	55

Chapter-5

Investigation of Bulk Bi_2X_3 ($\text{X} = \text{S}, \text{Se}, \& \text{Te}$) as Highly Durable Anode Materials

5.1	Introduction	57
5.2	Structural investigations of as prepared Bi_2X_3 anode composites	59
5.3	Cyclic voltammetry	61
5.4	C-rate optimization for Bi_2X_3 anodes	63
5.5	Galvanostatic discharge/charge	64
5.6	Mechanism of lithiation/delithiation of Bi_2X_3 anode in all-solid-state <i>Li</i> -ion battery	66
5.7	Cyclic stability measurements under 0.2-2.5V	70
5.8	Morphological investigations of Bi_2X_3 anode	71
5.9	Cyclic stability measurements under 0.2-1.5V	75
5.10	Summary	78

Chapter-6

Nanostructured Bi_2X_3 Anode with Highly Stable Electrochemical Performance

6.1	Introduction	79
6.2	Morphological studies of the prepared Bi_2X_3 nanostructures	80
6.3	Structural investigation of the prepared Bi_2X_3 nanostructures	84
6.4	Cyclic voltammetry	86
6.5	Cyclic stability measurements under 0.2-2.5V	88
6.6	Cyclic stability measurements under 0.2-1.5V	92

6.7	Summary	97
-----	---------	----

Chapter-7

Conclusions and Future Scope of Work

7.1	Conclusions	98
7.2	Future Scope of Work	102

References

LIST OF FIGURES

Figure 1.1: Classification of different types of energy storage technologies.	2
Figure 1.2: Schematic representation of a battery.	3
Figure 1.3: Comparison of specific as well as volumetric energy densities of different classes of batteries.	5
Figure 1.4: Conventional battery vs. all-solid-state battery.	6
Figure 1.5: Crystal structure representation of <i>Bi</i> & Bi_2X_3 ($\text{X} = \text{S}, \text{Se}, \& \text{Te}$) compounds.	11
Figure 1.6: Crystal structures of the a) LT and b) HT phases of LiBH_4 .	14
Figure 1.7: Arrhenius plot of the electrical conductivity of LiBH_4 at both phases (LT & HT).	14
Figure 3.1: Schematic of sample synthesis by hydrothermal method.	29
Figure 3.2: Schematic for the synthesis of Bi_2S_3 nanoflowers.	30
Figure 3.3: Schematic for the synthesis of Bi_2Se_3 nanostructures.	31
Figure 3.4: Schematic for the synthesis of Bi_2Te_3 nanorods.	32
Figure 3.5: Schematic diagram of SEM.	33
Figure 3.6: Digital images of the SEM instrument (a) NOVA NANO SEM 450 (b) JEOL JSM 6380 (c) SEM holder with a covered sample by polyimide sheet.	34
Figure 3.7: Schematic diagram of the TEM instrument.	36
Figure 3.8: Digital image of TECHNAI T20 FEI TEM instrument.	37
Figure 3.9: Schematic representation of the Bragg's equation.	38
Figure 3.10: Digital image of Rigaku-RINT 2500 XRD system.	39
Figure 3.11: A hardened stainless steel milling pot with 10 SS balls (a) and Fritsch P7 milling machine (b).	40

Figure 3.12: (a) Schematic diagram of various parts for the coin cell assembly and (b) digital photograph of the glove box.	41
Figure 3.13: Schematic representation of Cyclic Voltammetry.	42
Figure 3.14: Digital image of Bio-Logic SAS (SP-150) system for CV measurements.	43
Figure 3.15: Digital image of charge-discharge setup.	44
Figure 4.1: Cyclic Voltammogram of <i>Bi</i> composite electrode scanned at 0.1mVs^{-1} .	49
Figure 4.2: The initial galvanostatic discharge-charge profile for Bi-LiBH ₄ -AB composite negative electrode.	50
Figure 4.3: Ex-situ XRD patterns of Bi-LiBH ₄ -AB composite electrodes at different stages (indicated in Figure 2) of the first electrochemical discharge – charge process.	51
Figure 4.4: (a) The Cyclic galvanostatic discharge-charge profiles for Bi-LiBH ₄ -AB composite electrodes in the voltage range of 0.2-1.5V at 0.1C. Only selected cycles (1,5,10,20,30,40,50,60,70,80,90,100) are shown for clear visibility. (b) Cyclic stability of Bi-LiBH ₄ -AB composite electrodes as shown by Discharge/Charge capacity and the coulombic efficiency vs. cycle number.	53
Figure 4.5: SEM images and corresponding elemental mapping of <i>Bi</i> in the composite electrode surface before cycling.	54
Figure 4.6: SEM images and corresponding elemental mapping of <i>Bi</i> in the composite electrode surface after cycling.	55
Figure 5.1: XRD patterns of (a) bulk Bi ₂ S ₃ and (b) Bi ₂ S ₃ -LiBH ₄ -AB composite electrode.	59
Figure 5.2: XRD patterns of (a) bulk Bi ₂ Se ₃ and (b) Bi ₂ Se ₃ -LiBH ₄ -AB composite electrode.	60
Figure 5.3: XRD patterns of (a) bulk Bi ₂ Te ₃ and (b) Bi ₂ Te ₃ -LiBH ₄ -AB composite electrode.	61

Figure 5.4: Cyclic Voltammograms of bulk (a) $\text{Bi}_2\text{S}_3\text{-LiBH}_4\text{-AB}$ (b) $\text{Bi}_2\text{Se}_3\text{-LiBH}_4\text{-AB}$ (c) $\text{Bi}_2\text{Te}_3\text{-LiBH}_4\text{-AB}$ composite anode material scanned at 0.1 mVs^{-1} . 62

Figure 5.5: First electrochemical galvanostatic charging-discharging profile for bulk $\text{Bi}_2\text{S}_3\text{-LiBH}_4\text{-AB}$ composite electrode at several current rate (a) 1C, (b) 0.5C, (c) 0.2C, & (d) 0.1C. 64

Figure 5.6: The initial galvanostatic discharge-charge profile for (a) $\text{Bi}_2\text{S}_3\text{-LiBH}_4\text{-AB}$ (b) $\text{Bi}_2\text{Se}_3\text{-LiBH}_4\text{-AB}$ (c) $\text{Bi}_2\text{Te}_3\text{-LiBH}_4\text{-AB}$ composite negative electrode in the voltage range of 0.2-2.5V at 0.1C current rate, where (1), (2), (3), (4), (5), (6) & (7) represents the different potential points during discharge-charge measurement. 65

Figure 5.7: Ex-situ XRD patterns of $\text{Bi}_2\text{X}_3\text{-LiBH}_4\text{-AB}$ composite electrode on marked points in Figure 5.6. 68

Figure 5.8: Cyclic performance of the bulk (a) $\text{Bi}_2\text{S}_3\text{-LiBH}_4\text{-AB}$ (b) $\text{Bi}_2\text{Se}_3\text{-LiBH}_4\text{-AB}$ (c) $\text{Bi}_2\text{Te}_3\text{-LiBH}_4\text{-AB}$ composite electrode in the voltage range of 0.2-2.5V at temperature 125°C with 0.1C rate. 71

Figure 5.9: (a-e) SEM images and corresponding elemental mapping of Bi_2S_3 in the composite electrode surface before cycling, and (f) after 13 cycles in the voltage range 0.2-2.5V. 72

Figure 5.10: (a-e) SEM images and corresponding elemental mapping of Bi_2Se_3 in the composite electrode surface before cycling, and (f) after 9 cycles in the voltage range 0.2-2.5V. 73

Figure 5.11: (a-e) SEM images and corresponding elemental mapping of Bi_2Te_3 in the composite electrode surface before cycling, and (f) after 9 cycles in the voltage range 0.2-2.5V. 74

Figure 5.12: Cyclic discharging/charging profile of the bulk (a) $\text{Bi}_2\text{S}_3\text{-LiBH}_4\text{-AB}$ (b) $\text{Bi}_2\text{Se}_3\text{-LiBH}_4\text{-AB}$ and (c) $\text{Bi}_2\text{Te}_3\text{-LiBH}_4\text{-AB}$ composite electrode in the voltage range of 0.2-1.5V at 125°C with 0.1C rate. 76

Figure 5.13: FE-SEM images of bulk $\text{Bi}_2\text{S}_3\text{-LiBH}_4\text{-AB}$ composite anode after galvanostatic electrochemical discharging-charging in the voltage range of 0.2-1.5V (a) 0 cycles and (b) 50 cycles. 77

Figure 5.14: FE-SEM images of bulk $\text{Bi}_2\text{Se}_3\text{-LiBH}_4\text{-AB}$ composite anode after galvanostatic electrochemical discharging-charging in the voltage range of 0.2-1.5V (a) 0 cycles and (b) 50 cycles. 77

Figure 5.15: FE-SEM images of bulk $\text{Bi}_2\text{Te}_3\text{-LiBH}_4\text{-AB}$ composite anode after galvanostatic electrochemical discharging-charging in the voltage range of 0.2-1.5V (a) 0 cycles and (b) 50 cycles. 77

Figure 6.1: (a & b) FE-SEM & TEM images of Bi_2S_3 nanoflowers (c & d) HRTEM & SAED images of nanoflowers. 81

Figure 6.2: (a) & (b) FE-SEM images of as prepared Bi_2Se_3 nanostructures; (c-f) TEM, HRTEM & SAED pattern of nanostructures. 82

Figure 6.3: (a & b) FE-SEM images of Bi_2Te_3 nanorods and (c & d) TEM, HRTEM images of nanorods. 83

Figure 6.4: XRD pattern of (a) as-prepared Bi_2S_3 nanoflowers and (b) Bi_2S_3 nanoflowers- $\text{LiBH}_4\text{-AB}$ composite electrode. 84

Figure 6.5: XRD pattern of (a) as prepared Bi_2Se_3 nanostructures (b) Bi_2Se_3 nanostructures- $\text{LiBH}_4\text{-AB}$ composite electrode. 85

Figure 6.6: XRD pattern of (a) as-prepared Bi_2Te_3 nanorods and (b) Bi_2Te_3 nanorods- $\text{LiBH}_4\text{-AB}$ composite electrode. 86

Figure 6.7: Cyclic Voltammograms of (a) Bi_2S_3 nanoflowers- LiBH_4 -AB composite electrode (b) Bi_2Se_3 nanostructures- LiBH_4 -AB composite electrode (c) Bi_2Te_3 nanorods- LiBH_4 -AB composite electrode scanned at 0.1mVs^{-1} . 87

Figure 6.8: Cyclic performance of the nano (a) Bi_2S_3 - LiBH_4 -AB (b) Bi_2Se_3 - LiBH_4 -AB (c) Bi_2Te_3 - LiBH_4 -AB composite electrode in the voltage range of 0.2-2.5V at temperature 125°C with 0.1C rate. 89

Figure 6.9: SEM images of nano Bi_2S_3 - LiBH_4 composite anode after galvanostatic electrochemical discharging- charging in the voltage range of 0.2-2.5V (a) 0 cycles and (b) 13 cycles. 90

Figure 6.10: FE-SEM images of nano Bi_2Se_3 - LiBH_4 composite anode (a) before and (b) after 10 cycles of galvanostatic electrochemical discharging-charging in the voltage range of 0.2-2.5V. 91

Figure 6.11: FE-SEM images of nano Bi_2Te_3 - LiBH_4 composite anode after galvanostatic electrochemical discharging- charging in the voltage range of 0.2-2.5V (a) 0 cycles and (b) 10 cycles. 91

Figure 6.12: Cyclic performance of the (a) nano Bi_2S_3 - LiBH_4 -AB composite anode material, (b) Cyclic stability (Capacity vs. no. of the cycle) of commercial bulk Bi_2S_3 and Bi_2S_3 nanoflowers. 92

Figure 6.13: FE-SEM images of nano Bi_2S_3 - LiBH_4 composite anode after galvanostatic electrochemical discharging-charging in the voltage range of 0.2-1.5V (a) 0 cycles and (b) 50 cycles. 93

Figure 6.14: Cyclic discharging/charging profile of the (a) Bi_2Se_3 nanostructures- LiBH_4 -AB composite electrode (b) Cyclic stability (Capacity vs. no. of the cycle) of bulk Bi_2Se_3 and nano Bi_2Se_3 . 94

Figure 6.15: FE-SEM images of nano $\text{Bi}_2\text{Se}_3\text{-LiBH}_4\text{-AB}$ composite anode (a) before and (b) after 50 cycles of galvanostatic electrochemical discharging-charging in the voltage range of 0.2-1.5V. 95

Figure 6.16: (a) Cyclic performance of the Bi_2Te_3 nanorods- $\text{LiBH}_4\text{-AB}$ composite electrode (b) (c) Cyclic stability of bulk Bi_2Te_3 (blue curve) and nano Bi_2Te_3 (red curve). 96

Figure 6.17: FE-SEM images of nano $\text{Bi}_2\text{Te}_3\text{-LiBH}_4\text{-AB}$ composite anode (a) before and (b) after 50 cycles of galvanostatic electrochemical discharging-charging in the voltage range of 0.2-1.5V. 96

LIST OF TABLES

Table 1.1: Comparison of key features of various rechargeable batteries.	7
Table 1.2: Comparative study of traditional cathode materials.	12
Table 3.1: List of chemicals used in this thesis work	27

LIST OF ABBREVIATION

AFM	Atomic force microscopy
AB	Acetylene Black
<i>Bi</i>	Bismuth
BiCl ₃	Bismuth chloride
Bi ₂ O ₃	Bismuth oxide
Bi ₂ S ₃	Bismuth sulfide
Bi ₂ Se ₃	Bismuth selenite
Bi ₂ Te ₃	Bismuth telluride
DI	Deionized
DMF	Dimethylformamide
EDS	Energy-dispersive X-ray spectroscopy
EDTA	Ethylenediaminetetraacetic
<i>Li</i>	Lithium
LIBs	Lithium ion batteries
Li ₂ S-P ₂ S ₅	Lithium Sulfide Phosphorus Pentasulfide
NaBH ₄	Sodium borohydride
NaOH	Sodium hydroxide
PFA	Perfluoroalkoxy
<i>S</i>	Sulphur
<i>Sb</i>	Antimony
<i>Se</i>	Selenium
SEM	Scanning electron microscopy
SSBs	Solid state batteries
TEM	Transmission electron microscopy
Tu	Thiourea
<i>Te</i>	Tellurium

TG	Thermogravimetry
XRD	X-ray diffraction
XPS	X-ray photoelectron spectroscopy

1.1 General Introduction

Energy is an essential component in the daily lives of human society, and it can be used in altered forms in our regular activities. Energy production, storage, and supply are the essential features for societal growth; however, the development of cleaner, sustainable sources of energy is one of the major challenges in the twenty-first century. Nowadays, energy demand has increased because of the high energy consumption in several fields like transportation, industry, electricity generation, and household. The present dominating energy generating sources based on nuclear power plants and fossil fuels (oil, natural gas, and coal) have worked and fulfilled almost all the human needs for a long era. However, these fossil fuels and nuclear power sources suffered from several issues such as - the risk of global warming (associated with sulfur dioxide (SO₂), carbon dioxide (CO₂), and nitrogen oxide (NO₂) emission), overpriced, waste handling, safety issues, *etc.* Therefore, the research community is paying attention to develop the alternative energy sources, especially storage of electrical energy produced from the safer sources and the replacement of the traditional energy sources [1, 2]. Additionally, the cost of these energy sources has been increased in the past few years and anticipated to be increased even with a faster pace in the coming years [3], [4].

Furthermore, fossil fuel resources are limited in amount, and it is extensively accepted that most easily extracted assets will be exhausted after a few years [5]. All these problems have developed major political issues and subjects of international consideration and regulation. In this direction, several developments have been made in the previous years. For examples, renewable energy sources, such as wind energy, bioenergy, solar energy, tidal energy, geothermal energy, and hydropower have been developed and are currently being tried to replace fossil fuel energy infrastructure [6]. However, the use of almost all renewable energy

assets is hindered by their high cost. As a result, the technology could not be reached to their extensive use till now.

Furthermore, the use of solar energy, tidal energy, and wind energy is restricted by their unpredictable nature, as they are not available all the time. These issues have led to increasing efforts to find suitable alternative energy storage technologies such as fuel cells, supercapacitors, and batteries [7] (**Figure 1.1**). In this regard, *Li*-ion battery (LIB) currently plays a vital role in

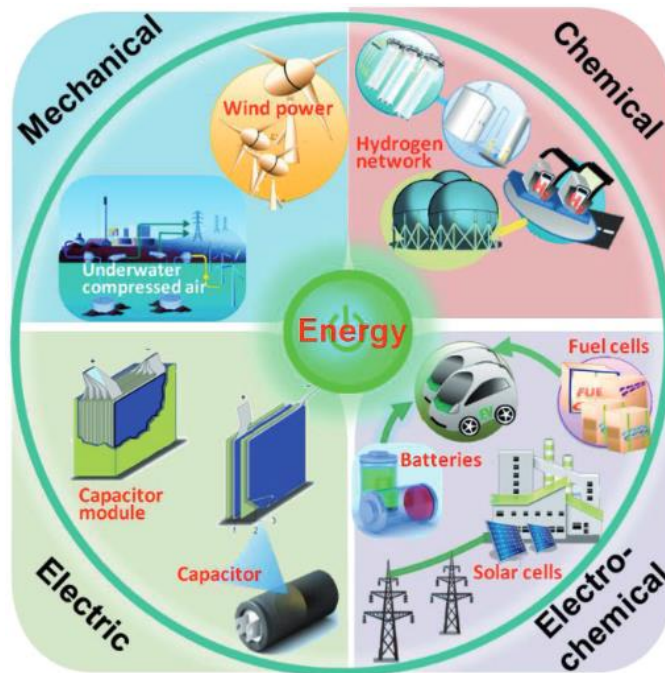


Figure 1.1: Classification of different types of energy storage technologies.

producing alternative energy storage devices, due to its inherent outstanding characteristics such as high energy density, high rate capability, flexible design, and long lifespan. The advanced technology deals with the most significant development potential for automobile industries mainly for electric vehicles (EV) and hybrid electric vehicles (HEV), which substitute electricity for a portion of the petroleum, used to power the vehicles [8], [9]. Moreover, it is attractive for its perspective to decrease greenhouse gases emission and the dependence on oil [10]. Based on the research analysis, although HEV reduces greenhouse emissions by 32% compared to conventional gasoline vehicles [11], they still emit global-warming pollutants.

Recently, LIBs have become an essential part of the technology to assist in the development of portable consumer electronic devices such as laptop, cellular phone, digital camera, video camera, and personal digital assistant around the world. As for the demand for electric vehicles, there is a need for the development of LIBs with high-performance characteristics, like high energy density, high cell voltage, long cycle life, and environmentally friendly. The electrochemical performance of this type of battery is mainly based on the properties (physiochemical and the electrochemical) of electrode materials used inside the battery.

1.2 Batteries

Batteries can be defined as devices, which can store energy in the electrochemical form and contain one or more cells connected in series or parallel or both to attain the desired capacity and voltage. A battery is one of the energy storage devices that can store chemical energy in their active materials and convert them into electrical energy through an electrochemical reaction taking place at the electrodes [12], [13]. Vital parts of a battery are cathode (positive electrode), the anode (negative electrode), an electrolyte (a medium to connect anode and cathode). A schematic representation of a battery is shown in **Figure 1.2**.

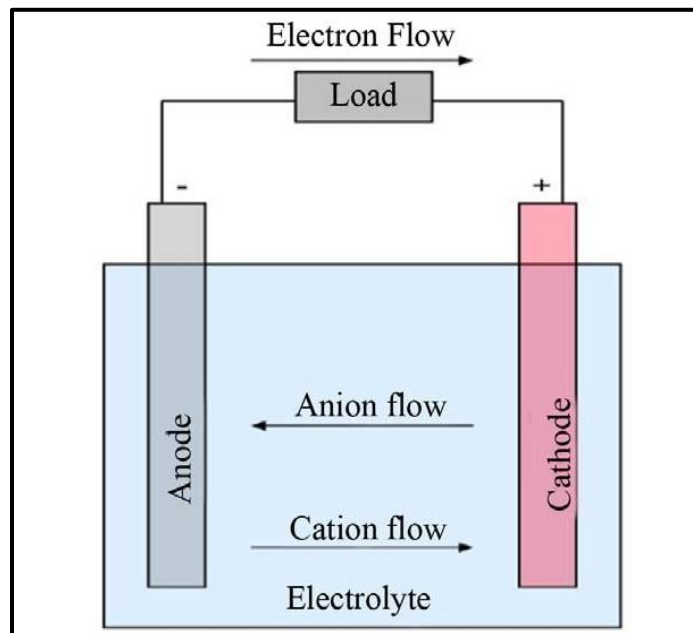


Figure 1.2: Schematic representation of a battery.

The above mentioned electrochemical reaction takes place through the oxidation-reduction reaction in batteries. During the reaction, one of the electrodes (negative electrode) in a battery oxidizes by giving up the electron which is used to reduce the other part (positive electrode). This reaction proceeds spontaneously; once these two electrodes are connected through an external circuit, the current through the flow of electrons in the external circuit can be used to power a resistive load. To shuttle ions between the active materials, the electrolyte also participates in the reaction. Battery technologies play a vital role in our everyday life and various fields of society, for example, electric vehicle propulsion and stationary energy storage [14]. Batteries are of two types (1) primary (non-rechargeable) and (2) secondary batteries (rechargeable) depending on the reversibility of the electrochemical processes [15], [16].

1.2.1 Primary Battery

Primary batteries are those type of cells in which the electrochemical reaction is generally not reversible, and during discharging, the chemical compounds in these batteries are permanently changed so these cells can be used only once and then replaced with new ones [17]. In general, primary batteries have a fixed quantity of energy stored in them during manufacture, and once that energy has been used up, the batteries are thrown away and replaced.

1.2.2 Secondary Battery

Rechargeable batteries/secondary batteries are those type of cells, in which the electrochemical reactions are reversible and give the extended life of the batteries. To recharge this kind of batteries, an external electrical power source is required with a constant voltage higher than that of the batteries to compensate the self-discharge. Secondary batteries are more environmentally friendly than primary batteries since they can be discharged and charged several times before losing their standard performance abilities reducing the amount of battery waste ending up in landfills.

There are different kinds of commercialized rechargeable batteries, and the most common rechargeable batteries are Lead-acid batteries, Nickel-cadmium batteries, Nickel-metal-hybrid batteries, and Lithium-ion batteries.

1.3 Li-ion Battery

Among all of the commercialized rechargeable battery, *Li-ion* batteries (LIBs) can play a very significant role because of its unique properties such as zero memory effect (unlike Ni-MH batteries), low self discharge, ease of maintenance, large specific energy density and high cycle stability in comparison of these batteries (**Figure 1.3**). To elucidate the preeminence of LIBs

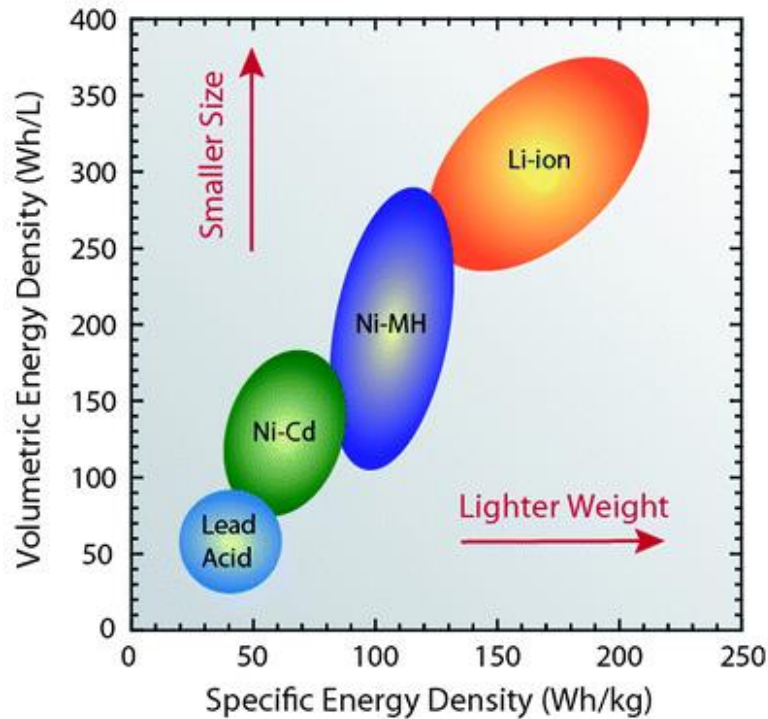


Figure 1.3: Comparison of specific as well as volumetric energy densities of different classes of batteries.

over other class of batteries, a comparative study is given in **Table 1.1**. The first LIB was successfully commercialized by Sony in 1991 by adopting carbon as the anode material [18], [19]. After that, different development activities are being continued on them towards the high performance of LIB. Based on the research analysis, various industrial revolutions have been developed in LIBs, which cause their applicability in high potential applications like an electric vehicle (EV) and hybrid electric vehicle (HEV). To date, for the safe and clean globe, LIB is the main thrust area, gaining the fanatical focus of the research community by employing batteries as the driving force for vehicles. Although LIBs lead the market of electrochemical power sources for portable devices and even deal with the greatest development potential for

electric vehicles and advanced energy storage of clean electricity; this technology suffers from some challenges. The expanded application areas require LIBs to have the features of high power density, long cycling life, and low costs [20], [21]. These challenges of battery technology are directly dependent on the challenges of electrode materials ultimately, and to date, the electrodes do not fulfill the aim for the wide applicability in transport and other practical applications. Replacing the conventional electrode materials with alternative anodes can significantly enhance battery performance. On the other hand, the long-standing challenge for conventional LIBs has been the safety issues related to the flammable organic liquid electrolyte, which limits the mass application of conventional LIBs in electric vehicles (EVs) or other energy storage applications. The ultimate solution to the fire hazard of conventional LIB lies in the implementation of all-solid-state LIBs, where solid-state electrolyte completely replaces the flammable liquid electrolyte (as shown in **Figure 1.4**). In addition to their intrinsic safety and reliability, all-solid-state LIBs also exhibit higher energy density and higher power density [22].

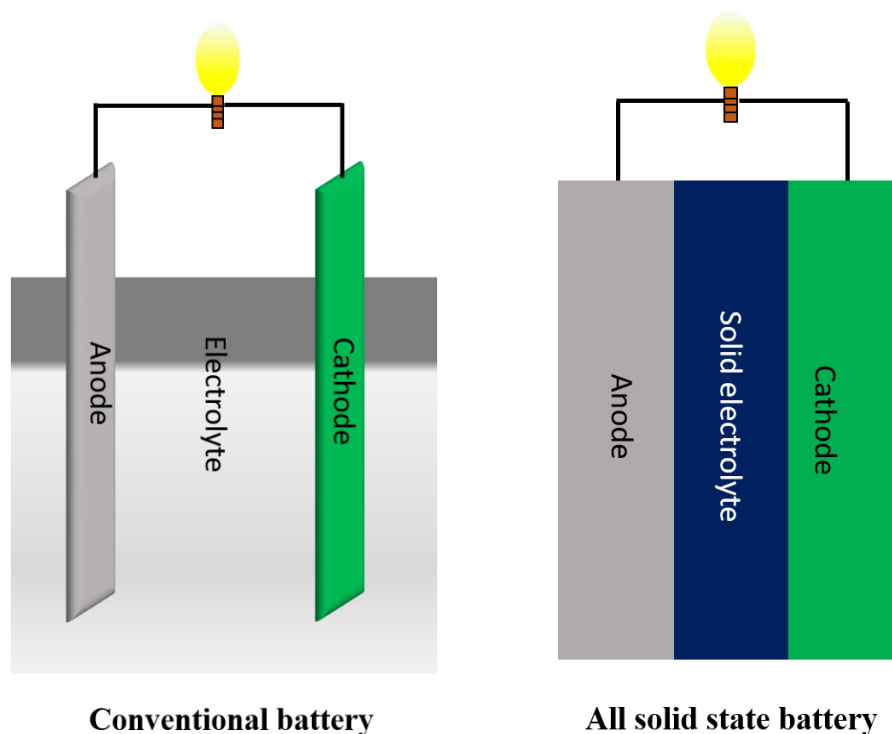


Figure 1.4: Conventional battery vs. all-solid-state battery.

Table 1.1: Comparison of key features of various rechargeable batteries.

Battery Chemistry	Anode	Cathode	Electrolyte	Specific Energy (Wh/kg)	Energy Density (W/kg)	Cell Voltage	Cycles (times)	Self-discharge (per month)	Discharge Efficiency	Efficiency	Life Time (Year)	Ref.
Lead-acid	Lead	Lead Oxide	Dil. H ₂ SO ₄	35-40	150-400	2V	≥ 1000	2-30 %	20-90%	75-90%	05	[23]
Nickel Cadmium	Cadmium	Nickel-Oxide hydroxide	KOH	30-60	80-150	1.2V	≥50,000	5-20%	70-80%	60-70%	15	[23]
Nickel Metal Hydride	Metal hydride	Nickel-Oxide hydroxide	KOH	60-80	200-300	1.2V	~600	Very high	30%	25%	2-3	[23], [24]
Nickel Iron	Iron	Nickel-Oxide hydroxide	KOH	50-60	80-150	1.5V	~2000	20-30%	80%	--	30-50	[25]
Li-ion (Electrodes vary)	Graphite	LiMn ₂ O ₄	LiPF ₆	80-180	200-1000	3.9V	>3000	02-10%	100%	--	5+	[23], [26]

1.4 Major components of LIBs

The essential component of each electrochemical cell in LIB contains the following parts:

- The negative electrode (Anode)
- The positive electrode (Cathode)
- Electrolyte
- Separator
- Current collectors

Among these parts, both the electrodes and electrolyte are the essential performance factor of the LIB, and these underlying factors are discussed in detail in the next sections.

1.4.1 Anode

The anode is one of the most critical components in LIBs which has been intensively studied in recent years. An anode must have the following properties for the excellent performance of a battery:

- High structural stability
- High specific capacity
- High energy densities
- Low potential
- High cycling efficiency and long cycle life
- Highly reversible capacity
- High levels of safety
- low cost, and compatibility with the counterparts of a battery
- Environmental friendly (Non-toxic)
- Adequate electronic and ionic conductivity

Some suitable performing anodes, which satisfy the above-mentioned points, are discussed in the following subsections:

1.4.1.1 Carbon-based anodes

Carbon-based materials such as graphite are presently the dominant anodes in commercial LIBs, which possess various properties such as excellent cyclic performance with high coulombic efficiency, high stability towards different properties like thermal, chemical and electrochemical, *etc.*, easy and inexpensive availability. However, it has several limitations too, *e.g.*, its low theoretical gravimetric as well as volumetric capacities of 372 mAhg^{-1} and 841 mAhcm^{-3} , respectively and safety issues due to its low reaction potential with *Li* (0.3 V vs. *Li/Li*⁺) [27]. Carbon-based material like graphite, being a layered structure, provides an opportunity for intercalation of *Li* ions, which stores up to one *Li*⁺ for every six carbon atoms between its layers and forms *LiC*₆ alloy phase on *Li*-intercalation.

Although another class of carbon, *i.e.*, graphene (delaminated from the layered graphite), provides a high theoretical capacity ($\sim 500\text{-}1100 \text{ mAhg}^{-1}$) than graphite [28], its gapless electronic structure creates a problem for using it into portable electronic devices and electric vehicles. Similar to graphite, graphene also shows excellent cycling stability but suffers from inadequate capacities (gravimetric as well as volumetric), which is needed to be high as per the requirements.

1.4.1.2 Silicon-based anodes

After oxygen, silicon (*Si*) is the most abundant element in the earth's crust, which has a very high gravimetric capacity (4200 mAhg^{-1}) and volumetric capacity (9786 mAhcm^{-3}). *Si* makes an alloy phase (*Li*₂₂*Si*₅) with *Li* during its lithiation at 0.2 V. Although *Si* has excellent electrochemical properties, it suffers from the significant volume expansion (up to 400%) during delithiation/lithiation process [29]. This vast volume expansion limits the anode material life and resulting in capacity fading.

Despite of these, several other anodes are also available such as Germanium (*Ge*)-based, Tin (*Sn*) based and antimony (*Sb*) based anodes, which displays the high specific capacity (*Ge*: 1600 mAhg^{-1} , *Sn*: 993 mAhg^{-1} , and *Sb*: 660 mAhg^{-1}) as well as volumetric capacity (*Ge*: 8517 mAhcm^{-3} , *Sn*: 7259 mAhcm^{-3} , and *Sb*: 4412 mAhcm^{-3}). However, these anode materials also face a problem of structural instability ($\sim 300\text{-}400\%$) during discharging/charging process [30]. The substantial volume change of these alloy materials during *Li*-ion insertion/extraction leads to a loss

of electrical contact and eventually rapid capacity fading upon cycling. To resolve this problem, constructing nanostructured active materials is a frequently proposed method to release stress during *Li*-ion insertion/extraction. As compared to other alloy materials, *Bi*-based materials are supposed to act as potential anodes for LIBs because of an element from the same group as *Sb* and diagonally related to *Sn* [31], [32].

1.4.1.3 Bismuth-based anodes

There are two critical features of *Bi* & *Bi*-based chalcogenide materials for which they can be utilized in electrochemical energy storage. One is that *Bi*-based materials have a unique layered crystal structure that can provide a larger interlayer spacing for comfortable accommodation of *Li*-ions. The other one is a convenience to reduce these to metallic *Bi*, which further alloys with *Li*-ions, originating Li_3Bi [33]. The reversible alloying process of *Bi* alone with *Li*-ions provide a similar gravimetric capacity of 385 mAhg^{-1} to that of conventional carbon anode but gives a very high volumetric capacity of 3800 mAhcm^{-3} (almost five-fold higher than graphite) due to a large packing density of 9.78 g/cm^3 [34]. As we know, limited space is usually available for the power systems in compact electronic devices, so high volumetric capacity of *Bi*-based materials offer a reliable and multifunctional platform to design energy devices that can meet our growing power and energy demands in the future [35].

In order to improve the specific capacities further, Bi_2X_3 ($\text{X} = \text{S}, \text{Se}, \& \text{Te}$) compounds have been deliberated as an anode for the next generation LIBs, which can provide higher gravimetric ($\sim 400\text{-}650 \text{ mAhg}^{-1}$) as well as volumetric ($\sim 4200\text{-}4500 \text{ mAhcm}^{-3}$) capacities. Bi_2X_3 have attracted attention due to their layered crystal structures and narrow bandgap (formed by a periodic arrangement of layers. Each layer is formed by five covalently bonded atomic sheets X-Bi-X-Bi-X , defined as a quintuple layer with a thickness of $\sim 1\text{nm}$ as shown in **Figure 1.5**. All quintuple layers are held together by van der Waals interaction.

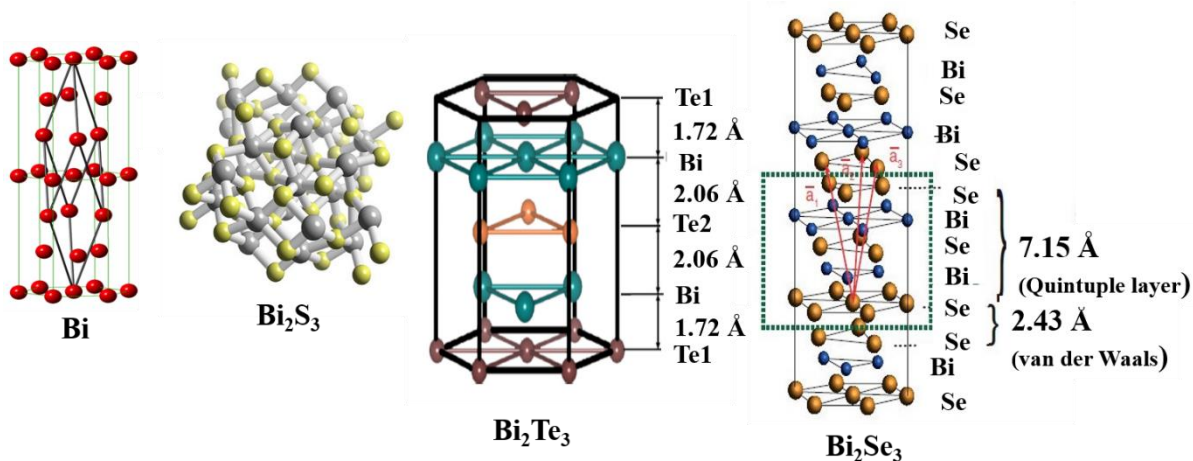


Figure 1.5: Crystal structure representation of Bi & Bi_2X_3 ($X = \text{S}, \text{Se}, \text{Te}$) compounds.

Owing to the layered structure, Bi_2X_3 compounds may allow easy *Li*-ion insertion into the van der Waals gaps and make them potentially applicable in LIBs [36], [37]. Although Bi_2X_3 compounds have many advantages, including high capacity, and low cost, their practical application is hindered by the poor cycling stability due to the significant volumetric expansion [38]. Such a considerable volume variations upon lithiation and delithiation cause severe particle cracking and pulverization, which breaks the electrical contacts in the anode, leading to a drastic capacity fading [39]. Thus, how to improve the cyclability of the Bi_2X_3 materials remains a crucial challenge to be addressed.

1.4.2 Cathodes

Common cathode materials are metallic oxides or sulfides containing *Li*-ions, which undergo oxidation to higher valences on discharging and reduction on charging. The positive electrode (cathode) is one of the crucial component, which affects the energy density, cycle life, safety, voltage, and other basic electrochemical and physicochemical properties in any battery. Few successfully employed cathodes are compared here based on their electrochemical performances (as shown in **Table 1.2**):

Table 1.2: Comparative study of traditional cathode materials.

Cathode	Theoretical Capacity (mAhg ⁻¹)	Reversible Capacity (mAhg ⁻¹)	Discharge potential vs. <i>Li/Li</i> ⁺	Energy density (Wh/kg)	Charge limits	References
LiMn ₂ O ₄	148	120	3.7-3.8V	110-120	4.20V	[40]–[46]
LiFePO ₄	170	165	3.45V	95-140	3.60V	
LiCoO ₂	272	148	3.60V	110-190	4.20V	
LiNi _{1/3} Mn _{1/3} Co _{1/3} O ₂	280	200	3.8V	--	4.6V	
Li ₂ MSiO ₄ (M-Fe/Mn/Co)	330	--	4.0V	--	>4.5V	

1.4.3 Electrolyte

An electrolyte is a medium to connect the two electrodes, and in order to avoid the electric short-circuit, electrolyte should be highly ionic conductive but poorly electronic conductive. The main aim of the electrolyte is to flow *Li*-ions continuously between the electrodes during delithiation/lithiation processes. To achieve excellent performance of a battery, a suitable electrolyte should follow the requirements such as high internal resistance, high ionic conductivity, low melting point, high boiling point, full potential window, and high chemical stability with proper safety [47]. Various kind of electrolytes can be used in LIBs like liquid, solid, gel polymer, and ceramic electrolytes. The mainly used liquid electrolytes are based on *Li*-salt such as Lithium hexafluorophosphate (LiPF₆), Lithium triflate (LiCF₃SO₃), Lithium perchlorate (LiClO₄), Lithium imide (Li₂NH), Lithium hexafluoroarsenate (LiAsF₆), Lithium tetrafluoroborate (LiBF₄) and organic solvents, typically carbonates [48]–[50]. In LIBs, ethylene carbonate (EC), dimethyl carbonate (DMC) and diethyl carbonate (DEC) is the most used solvents [51].

Currently, solid electrolytes are being focused because of the leakage and instability problems associated with liquid electrolytes. Due to the flammable nature and safety issues, liquid electrolyte limits the mass application of conventional LIBs in electric vehicles (EVs) or other energy storage applications. The problems associated with liquid electrolytes can be tackled with solid-state electrolyte materials, as solid electrolytes possess several beneficial properties such as high

stability with high temperatures, easy preparation, easy to alter the shape for making different battery configurations, excellent mechanical property, and good ionic conductivity. In addition to their intrinsic safety and reliability, all-solid-state LIBs also exhibit higher energy density and higher power density [52], [53]. Solid electrolytes allow the movement of ions through the voids or empty crystallographic positions in their crystal lattice structures. The essential requirements for solid electrolytes are (1) high ionic conductivity of above 10^{-4} Scm^{-1} at room temperature, (2) negligible electronic conductivity, and (3) wide electrochemical stability windows.

Based on the available literature, several theories like Anderson-Stuart model, Counter-ion model, Lattice gas models, Jump-diffusion model, *etc.* exist to clarify the charge transfer mechanism in solid electrolytes. Based on these models, in 1990s ORNL (Oak Ridge National Laboratory) introduced a new class of solid electrolyte called as LIPON by incorporating nitrogen into Li_3PO_4 . Although this electrolyte possesses an excellent electrical resistivity with a wide range of thermal and potential stability, it delivers an inferior ionic conductivity (10^{-6} Scm^{-1}) than liquid electrolytes [54]. Hence due to the low ionic conductivity, high interfacial impedance, and rate capability, this material could not be applicable for high-end applications, *e.g.* , EV and HEV. Furthermore, polymer electrolytes, sulfur-based, and oxide-based electrolytes have been investigated in details to achieve the objectives. However, polymer electrolytes are not suitable for high-temperature operations and suffer from mechanical instability. On the other hand, sulfur-based solid electrolytes have high ionic conductivity (10^{-2} Scm^{-1}) at room temperature, but these are not stable in the ambient atmosphere[55]. The LIBs using inorganic oxides based electrolytes such as Perovskite-structured $\text{Li}_3\text{xLa}_{2/3-\text{x}}\text{TiO}_3$ [56], Garnet-structured $\text{Li}_7\text{La}_3\text{Zr}_2\text{O}_{12}$ (LLZO) [57], [58], NASICON-structured $\text{Li}_{1.3}\text{Al}_{0.3}\text{Ti}_{0.7}(\text{PO}_4)_3$ (LATP) are still in the initial phase of research [59].

Although a vast number of solid-state electrolytes have been explored, LiBH_4 (lithium borohydride) has been investigated very intensively due to its remarkably high Li^+ conductivity in the order of 10^{-3} Scm^{-1} for its high-temperature phase at 115°C [60], [61]. LiBH_4 is a complex hydride which has an ionic bonding between $[\text{BH}_4]^-$ and Li^+ ions. Its crystal structures at different temperature are depicted in **Figure 1.6**. As seen in **Figure 1.6 (a & b)**, LiBH_4 crystallizes in an

orthorhombic structure with space group $pnma$ at room temperature/low temperature (LT). At approximately 390K, its structure transforms to hexagonal with space group $p6_3mc$ [62].

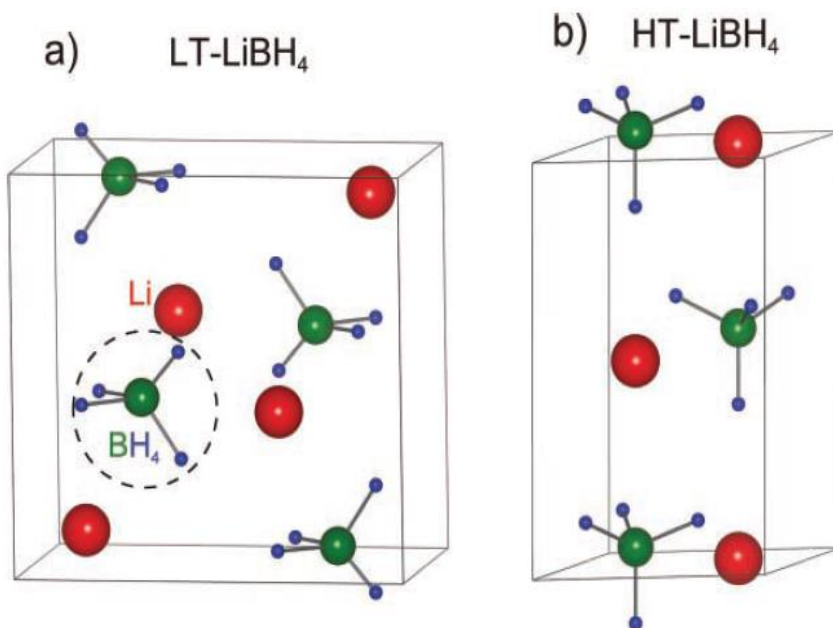


Figure 1.6: Crystal structures of the a) LT and b) HT phases of LiBH₄.

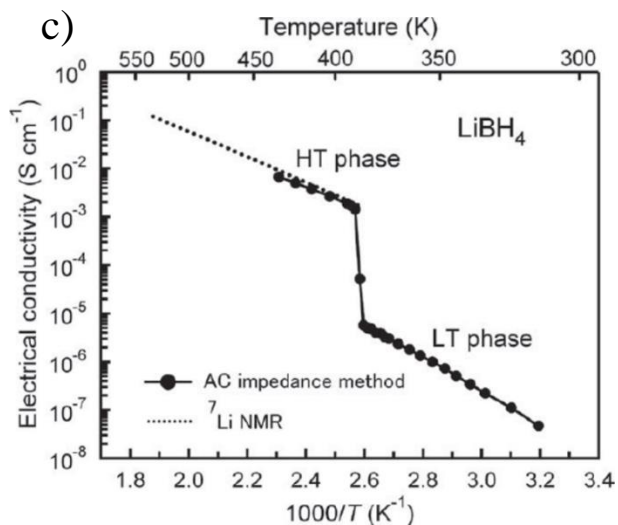


Figure 1.7: Arrhenius plot of the conductivity of LiBH₄ at both phases (LT & HT).

As shown by **Figure 1.7**, the conductivity of LiBH₄ is in the order of 10⁻⁸ Scm⁻¹ - 10⁻⁶ Scm⁻¹ for its LT phase and increased drastically to 10⁻³ Scm⁻¹ at around 390K. In the HT phase of LiBH₄, nearly

free rotation of the complex anion $[\text{BH}_4]^-$ occurs which assists the formation of metastable interstitial lithium site, leaving a lithium vacancy and enabling the material to act as lithium carrier [63]. A percolation of lithium sites in its crystal lattice enables the formation of lithium-ion conduction paths resulting in high lithium ionic conductivity that exceeds 10^{-3} Scm^{-1} for HT phase. The high *Li*-ion conductivity of LiBH_4 at high temperature makes it attractive to be used as a solid electrolyte for LIBs. Despite its high ionic conductivity, LiBH_4 has been employed only for hydride material as a solid-state electrolyte, so far [64], [65] as it was believed that the reaction kinetics could be enhanced due to H-H exchange between LiBH_4 and the hydride materials [66]. In order to extend the use of LiBH_4 to the other electrode materials and establish it as a universal solid electrolyte, it is necessary to investigate its compatibility with them.

1.5 The motivation of the research work

Based on the brief introduction and literature survey on batteries and their essential parts, it is clear that choice of the anode material is the main factor to achieve the target of applying LIBs in high energy applications, where high specific capacity and high structural stability are the two required aspects which should be satisfied by adopted anode materials. To balance these two criteria, *Bi* & *Bi*-based materials were chosen in the present study. In order to solve the problem of massive volume expansion during discharging/charging process, nanostructured anodes were also synthesized by the hydrothermal method because these anodes can release stress during *Li*-ion insertion/extraction. The solid-state electrolyte is also an essential component for the all-solid-state battery assembly. In this regard, LiBH_4 was used as an electrolyte to provide better ionic conductivity and eternal stability to the chemical/thermal environment. It has been observed that no report has focused on the implementation of *Bi*-based anodes in all-solid-state LIBs so far. At the same time, no report focused the generalization of LiBH_4 as universal electrolyte beyond its application with hydride anode materials only.

1.6 Objectives of the Thesis

To realize the above goals, the proposed objectives of the thesis can be pointed out as follows:

1. Evaluation of the electrochemical performance of *Bi* & Bi_2X_3 ($\text{X} = \text{S}, \text{Se}, \& \text{Te}$) in all-solid-state *Li*-ion battery using LiBH_4 as a solid electrolyte and to establish electrochemical reaction mechanism between *Bi*, Bi_2X_3 & *Li*-ion.
2. To evaluate the cyclic stability of *Bi* & Bi_2X_3 in all-solid-state *Li*-ion battery.
3. Synthesis of the Bi_2X_3 nanostructures in order to improve the cycle stability. Optimization of the synthesis parameters (*i.e.*, temperature and time) and methods to control the morphology of the nanostructures is therefore set to be one of the objectives.
4. To elaborate on the effect of nanostructures on the electrochemical performance of all-solid-state *Li*-ion battery.

2.1 Introduction

To date, highly safe, environment-friendly, high power and high volumetric energy density, long life anode materials are the central key for the next-generation *Li*-ion batteries (LIBs), and it has become one of the crucial research hotspots for energy scientist society [67]–[69]. For LIBs as energy storage systems in emerging large-scale applications such as for the electric vehicles and electric hybrid vehicles, only carbon materials cannot satisfy the future requirements due to their limited specific and volumetric capacities (gravimetric capacity; 372 mAhg^{-1} , and volumetric capacity; 840 mAhcm^{-3}) [70]. Furthermore, the considerably low operating voltage poses severe safety issues and also origins poor rate capability resulting from dendritic lithium and the formation of thick solid-electrolyte interphase on the surface of carbon anodes. Transition metals, including their sulfides and oxides, can be used as high capacity anode materials. However, these suffer from enormous volume expansion, poor conductivity, high operating voltages, and slow kinetics throughout the conversion and alloying process [71], [72]. Bismuth (*Bi*) is an exotic pentavalent metal from V-A group, known as a stable element with the highest atomic mass. From the last few years, *Bi* performed as a promising anode material for high energy density Lithium-ion, Sodium-ion, and Potassium-ion batteries, due to its high volumetric capacity (3765 mAhcm^{-3}), low ecotoxicity, and nominal operating voltage [31], [73].

Furthermore, *Bi*-based materials/*Bi*-chalcogenide compounds Bi_2X_3 ($\text{X} = \text{S}, \text{Se}, \text{Te}, \& \text{O}$) also deserve to be discussed as anode materials for *Li*-storage, owing to their unique layered crystal structure that can provide sufficient interlayer spacing to accommodate *Li*-ions and generate Li_3Bi . As per the literature review, Bi_2X_3 reveals the high volumetric capacity ($\sim 4000 - 6000 \text{ mAhcm}^{-3}$) as well as gravimetric capacity ($\sim 400 - 700 \text{ mAhg}^{-1}$) [74]. The theoretical volumetric capacity of *Bi* & Bi_2X_3 is much higher than other attractive anode materials, including *Si* (2190 mAh/cm^3), *Sn* (1991 mAh/cm^3) and *Sb* (1889 mAh/cm^3). Moreover, safety is a big issue in existing commercial

LIBs, which is associated with using highly flammable liquid organic electrolytes [74]. To address the safety issues, all-solid-state LIBs have been introduced, in which currently used liquid organic electrolytes were replaced by the non-flammable and highly stable solid electrolytes. In terms of ionic conductivity, solid electrolytes, *e.g.*, Oxides [75] and sulfides [76] have conductivity similar or just slightly less than that of conventional liquid electrolytes. Although oxides and sulfides based solid electrolytes do not show excellent stability and compatibility as per the demands of current all-solid-state *Li*-ion batteries [77]. Nowadays, complex hydrides based solid electrolyte (LiBH_4) have attracted intense attention for all-solid-state LIBs, which mainly consist of Li^+ and $(\text{BH}_4)^-$ ions [78].

The current thesis work deals with the electrochemical performance of *Bi* & *Bi*-based anode and complex hydride, *i.e.*, LiBH_4 as high conducting electrolyte in all-solid-state battery assembly.

2.2 *Bi*-based anode

Bismuth (as an anode) makes an alloy with lithium to produce Li_3Bi alloy and give a high volumetric capacity (3800 mAh cm^{-3}), which is 4-5 fold higher than commercial graphite anodes, and the high volumetric capacity makes it attractive as an anode. The electrochemical performance of *Bi* & *Bi*-based anodes has been extensively investigated by many researchers. Some of the results are summarized below:

- Zhao *et al.* investigated the electrochemical performance of bulk *Bi-C* composites as high capacity anodes for LIBs with liquid electrolyte [1M LiPF_6 in ethylene carbonate (EC)/diethyl carbonate (DEC) (1: 1 v/v)]. Lithiation/delithiation process was evaluated with an Arbin battery cycler under the galvanostatic condition in the voltage window of 0.05 - 2 V. The *Bi-C* composite electrode reveals a flat discharge potential plateau at 0.9 V vs. Li^+/Li . The initial galvanostatic discharge-charge measurements indicated that the *Bi-C* electrode exhibits a substantial irreversible capacity loss in the first cycle, and the initial coulombic efficiency (ICE) as low as 58 %. Such a low ICE may result from the electrolyte decomposition and formation of SEI on the surface of *Bi* [35]. Moreover, commercially available bulk *Bi-C* electrodes showed significant capacity decay from $\sim 650 \text{ mAhg}^{-1}$ to around 200 mAhg^{-1} after 100 cycles. This capacity decay was originated from a low electronic conductivity and the massive volumetric and structural evolution during the

charge/discharge process. These issues with *Bi* seemed to be responsible for the poor cyclic stability and rate capability of *Bi*.

- It is a well-known fact that the electrode performance of a battery depends upon the crystallinity, phase purity, grain size, particle size, and particle size distribution of the electrode materials [79]. The nanostructured active anode materials give the high surface area and short diffusion path for ionic and electronic transport of *Li*-ions, which results in an improved rate (power) capability and cyclic stability of a battery; hence *Bi* nanostructured anodes were used from the last decades to resolve the issue of volume expansion. For example, C. M. Park *et al.* performed the comparative electrochemical study on the commercially available bulk *Bi*, milled *Bi*, and *Bi/C* nanocomposites and observed that the pure *Bi* electrodes exhibit very poor reversibility. On the other hand, in the case of milled *Bi* sample (prepared by high energy ball milling method), enhanced reversibility was found due to the reduced particle size. However, the capacity fades rapidly after a few cycles. Furthermore, the *Bi/C* nanocomposite electrodes manifested an improved electrochemical charge-discharge behavior than pure *Bi* & milled *Bi* electrodes, with a high volumetric capacity [80].
- Dai *et al.* prepared mesoporous *Bi@C* nanowires by a controlled pyrolysis technique and directly used them as an active anode material in LIBs. The obtained specific capacity of $\sim 250 \text{ mAh g}^{-1}$ at 1 Ag^{-1} proved an enhanced lithium-ion storage performance compared to that of neat *Bi* nanowires ($\sim 50 \text{ mAhg}^{-1}$ at 1 Ag^{-1}) [81].
- Yang *et al.* successfully synthesized the sphere-like *Bi@C* nanocomposites by the aerosol spray pyrolysis technique. During this process, *Bi* nanoparticles having a diameter of 10-20 nm were uniformly distributed in a carbon matrix, and after that, the prepared nanocomposite was used as an anode for LIB. The *Bi@C* composite electrode exhibited excellent cyclic performance, as, after 100 cycles, a reversible capacity was found as high as 280 mAhg^{-1} . Also a remarkable rate performance was obtained at different current densities (at 0.1 Ag^{-1} , 0.2 Ag^{-1} , 0.5 Ag^{-1} , 1 Ag^{-1} , and 2 Ag^{-1} , specific capacities were obtained as 299, 252, 192, 141, and 90 mAhg^{-1} , respectively). Hence, it was concluded that the excellent performance of the *Bi@C* nanocomposite electrode is related to the *Bi* nanosized particles, which gives a shorter ion/electron diffusion way. The carbon matrix

not only enhances the electrical conductivity of the electrode but also buffers the volume change during discharge/charge process [31].

- To improve the electrochemical performance of *Bi*-based anode materials, Zhang *et al.* prepared an *N*-doped graphene/*Bi* nanocomposites using a two-step method, combining the gas/liquid interface reaction with the rapid heat-treatment process. As a result, a high lithium storage capacity (522 mAhg^{-1}) was obtained in the initial cycle under 0.01-3.5V. Furthermore, after 50 cycles, the specific capacity retained was 386 mAhg^{-1} . The obtained excellent electrochemical results of *N*-doped graphene/*Bi* nanocomposite anode concluded that nitrogen-doped graphene provides a high electronic conductivity to the anode composite material and synergetic effect of *Bi* nanoparticles also take an essential part in the improved cyclability [73]. Additionally, some other investigations on *Bi*-based anode materials also exist in the available literature, which encourages the idea to develop more high-performance *Bi*-based composite electrodes for LIBs [82], [83].

2.3 Bismuth chalcogenides Bi_2X_3 ($\text{X} = \text{S}, \text{Se}, \& \text{Te}$) based anode

In the past years, Julien and coworkers investigated the *Li*-storage in bismuth chalcogenides using different electrochemical methods [36]. In terms of the volumetric capacity as well as gravimetric capacity, Bi_2X_3 anode materials give higher values than *Bi* anode.

2.3.1 Bi_2S_3 based anode

Out of *Bi*-chalcogenides, Bi_2S_3 possess the highest capacity, and in addition to LIBs, it has been widely used in many other fields, such as optics [84], [85], photoelectricity [86], [87], photocatalysis [88], [89] and biology [90], due to its direct bandgap of 1.3eV. Bi_2S_3 is proposed as an ideal host for hydrogen [91], [92] and *Li* [93], [94] because of its unique lamellar structure. Layered bismuth sulfide (Bi_2S_3) has emerged as a prime *Li*-storage material due to its high theoretical gravimetric (625 mAhg^{-1} – 2 times of carbon) as well as volumetric capacity (4250 mAhcm^{-3} – 5 times of carbon) and intriguing reaction mechanism. Although Bi_2S_3 has many advantages, including high capacity, nontoxic nature, and low cost, its practical application is hindered by the poor cycling stability due to its sizeable volumetric expansion in lithiation process [95].

- Bi_2S_3 nanorods recorded a high discharge capacity of 810 mAhg^{-1} as reported by Zhou *et al.* for the first time. However, no information on the charge capacity and cycling stability was provided [96]. Later the *Li*-storage capability of dandelion-like Bi_2S_3 microspheres was investigated by Zhang *et al.* and unfortunately, the capacity was decayed very rapidly and retained the value of only 100 mAhg^{-1} after eight cycles [97].
- Similarly, Ma *et al.* investigated the *Li*-storage capability of smooth Bi_2S_3 fabrics, which showed the initial discharge and charge capacities of 1083 and 652 mAhg^{-1} , respectively. However, the capacity was dropped to 366 mAhg^{-1} after ten cycles [98]. It turns out that the significant issue with storing *Li*-ions in Bi_2S_3 is poor cyclability, which is strongly associated with their reaction towards lithium.
- Jung *et al.* have published the reaction mechanism between Bi_2S_3 and *Li*-ion and the results showed that the conversion step presents a high volumetric expansion (90%) with 74% volume increment in subsequent alloying contribution. Such a considerable volume variations upon lithiation and delithiation caused severe particle cracking and pulverization, which broke the electrical contacts in the anode, leading to a drastic capacity fading [95].

Thus, how to improve the cyclability of the Bi_2S_3 materials remains a crucial challenge to be addressed.

2.3.2 Bi_2Se_3 based anode

Bismuth selenide (Bi_2Se_3), with a narrow bandgap of 0.3eV , has attracted significant attention due to its potential applications for thermoelectric generators [99], [100], topological insulators [101], [102] and in optoelectronic devices [103], *etc.* Bi_2Se_3 crystallizes in a layered structure formed by a periodic arrangement of layers, and each layer is formed by five covalently bonded atomic sheets Se-Bi-Se-Bi-Se, defined as a quintuple layer with a thickness of $\sim 1\text{nm}$. All quintuple layers are held by van der Waals interactions, whereas covalent bond forms between atomic sheets. Owing to its layered structure, Bi_2Se_3 may allow easy *Li*-ions insertion into its van der Waals gaps and make it potentially applicable in LIBs [104], [105]. Also, Bi_2Se_3 behaves as a promising host for *Li*- storage due to its high electrical conductivity (10.6 Scm^{-1} at 300K) [106]. However, its

theoretical capacity (491 mAhg^{-1}) is slightly lower than Bi_2S_3 electrode, because of its considerable higher formula weight. To date, several studies on Bi_2Se_3 – based bulk/micro/nanostructures have been investigated to serve as *Li*-storage electrode materials, few of them are discussed herein:

- Bi_2Se_3 sheet-like structures and micro-rods showed a first discharge capacity of 725.6 and 870 mAhg^{-1} , respectively, but the capacity was found to be decrease rapidly with cycling [107], [108]. Also, Xu *et al.* studied the prepared (self-sacrificial template method) Bi_2Se_3 micro rods and observed that the initial discharge capacity of 870 mAhg^{-1} reached down to 55 mAhg^{-1} after 49 cycles. The poor cyclic stability was ascribed to the vast volume expansion during the discharge/charge process.
- The *In*-doped Bi_2Se_3 and Bi_2Se_3 -*S* hierarchical nanostructures showed better cycling performance, with a discharge capacity of 163 mAhg^{-1} after 50 cycles and 109 mAhg^{-1} after 100 cycles, respectively [37]. Similarly, *S*-doped Bi_2Se_3 microspheres were synthesized in the presence of BiCl_3 , *Se* powder, and thioglycol. The prepared microspheres were directly used as a negative electrode in LIB. The specific capacity of *S*-doped Bi_2S_3 microsphere electrode was found to be 109.4 mAhg^{-1} after 100th cycle.
- In addition, Yang *et al.* reported that Bi_2Se_3 nanosheets with a thickness of $\sim 20 \text{ nm}$ exhibit better cycling performance, with a discharge capacity of 123 mAhg^{-1} . However, hierarchical nanosheets of $\text{Bi}_2\text{Se}_{3-x}\text{S}_x$, synthesized by the solvothermal route in a mixed solvent of ethylene glycol (EG) and Diethylenetriamine (DETA) showed even higher *Li*-ion storage performance than other available reports with a discharge capacity of 235 mAhg^{-1} after 30 cycles [109].

The significant volume expansion during delithiation/lithiation process causes the poor cyclic stability of Bi_2Se_3 based anode materials. For practical applications, large specific capacity and cyclic durability of a LIB are crucial factors. Recently, few attempts have been made to achieve these goals; but further improvements are urgently required [110].

2.3.3 Bi₂Te₃ based anode

In last few years, the *Bi*-chalcogenide anode materials have been intensively deliberated for the next-generation LIBs. As mentioned above, bismuth selenide (Bi₂Se₃), and bismuth sulfide (Bi₂S₃) have been studied as anode materials with liquid electrolytes. Similar to the mechanism in the materials mentioned above, bismuth telluride (Bi₂Te₃) can also electrochemically reversibly store *Li*-ions by forming the Li₃Bi and Li₂Te compositions. Although *Bi*-based systems have a higher energy density, they suffer from poor cycling performance. The capacity fading occurs due to the large volume change during charging-discharging and resulting in the loss of the physical contact between the active particles and the current collector during cycling [111]. To address the high volume expansion and contraction problem during cycling, nano-sized materials were used as anode due to their unique properties, such as high surface area, short *Li*⁺ ion diffusion path length, and high electron transportation rate. [28], [112]

- First-time Fangfang Tu *et al.* used the bare Bi₂Te₃ nanoplates (prepared by solvothermal method) as anode material with liquid electrolyte LiPF₆ in ethylene carbonate (EC)/dimethyl carbonate (DMC) (volume ratio 1:1). The electrochemical measurements were performed with a half coin cell which was assembled in an *Ar*-filled glove box using *Li*-foil as a cathode, Bi₂Te₃ nanoplates as an active material, and Celgard 2300 membrane as a separator. The galvanostatic charge/discharge measurements exhibited that the specific capacity of the cell drops to <100 mAhg⁻¹ after ten cycles [39]. In this report, Bi₂Te₃ based anode suffered from low cyclability and low reversibility.
- To improve the cycling stability and reversibility of bare Bi₂Te₃, Tu *et al.* also prepared Bi₂Te₃ nanoplate/Graphene nanosheet (Bi₂Te₃/G) nanohybrid with a sandwich structure. The Bi₂Te₃/G nanohybrid showed the capacity of 200 mAhg⁻¹ and demonstrated as slower capacity decay compared to bare Bi₂Te₃. A specific capacity after the 50th cycle was found as high as 158 mAhg⁻¹ in case of Bi₂Te₃/G, whereas in case of bare Bi₂Te₃ it was decayed rapidly to 33 mAhg⁻¹. This improved cyclic stability is attributed to the buffering effect of graphene and also the electrode kinetics enhanced by the graphene, which shows the relatively high reversibility of the negative electrode.

Based on the literature survey, it is apparent that no report focused on the implementation of Bi & Bi_2X_3 based anodes in all-solid-state Li -ion batteries so far. In this research work, these anode materials were introduced in the all-solid-state battery with $LiBH_4$ as solid electrolyte.

2.4 $LiBH_4$ as a solid electrolyte in all-solid-state LIBs

The rechargeable LIBs with high energy and power densities are deliberated as one of the essential key factors to the extensive application of clean and renewable energy sources, *e.g.*, EV and smart grid [54, 55]. To develop advanced electrolytes with high ionic conductivity, excellent electrode compatibility, and wide electrochemical stability, widespread efforts have been devoted by the researchers [114]. Most of the research focuses on the liquid organic electrolytes, which show high Li -ion conductivity but suffer from some serious issues, *e.g.*, low stability and poor compatibility with electrodes [57, 58]. These drawbacks of the liquid electrolytes cause the reversible capacity decay and severe safety issues, which can be resolved through the implementation of solid electrolytes for LIBs. Solid electrolytes assist the assembly of all-solid-state LIBs with superior thermal and mechanical stability, and can significantly boost battery safety as well as performance [117]. Although several studies were conducted to find a suitable solid electrolyte over the past few decades, a solid electrolyte with high chemical and electrochemical stability remains a challenge. Nowadays, complex hydrides, which predominantly consist Li^+ and $(BH_4)^-$, $(NH_2)^-$, $(B_{12}H_{12})_2^-$, and $(AlH_6)_3^-$ have drawn intense interest as solid electrolytes for all-solid-state LIBs [14, 60–63]. Among them, $LiBH_4$ reveals a probability under an electrochemical stable potential window of 0-5V vs. Li/Li^+ . It shows a very high conductivity in the order of 10^{-3} Scm^{-1} at 120 °C due to its highly conductive $P6_3mc$ phase (discussed in detail in chapter 1). Reports related to $LiBH_4$ as a solid electrolyte in LIBs are summarized below:

- Takahashi and co-workers investigated the applicability of $LiBH_4$ as a solid-state electrolyte in rechargeable LIB for the first time. $LiCoO_2$ was used as a cathode and Li as an anode for the cell assembly, and the battery performance was evaluated at 393 K [78]. Although $LiBH_4$ revealed excellent compatibility with Li -electrodes, a reaction between $LiCoO_2$ and $LiBH_4$ occurred due to their direct contact and resulted in a high interfacial resistance that exceeded the value of $8000 \Omega \text{ cm}^2$ [122]. This issue was solved by using a 25 nm thin interlayer of amorphous Li_3PO_4 between $LiCoO_2$ and $LiBH_4$, which reduced the

interfacial resistance to approximately $16 \Omega \text{ cm}^2$. Furthermore, after particular modifications, the discharge/charge measurements were performed, and the initial discharge capacity was found to be 89 mAhg^{-1} , which decayed by only 3% after the 30 cycles. This shows that LiBH_4 based complex hydride electrolytes may work well with the high voltage oxide-based electrodes by some surface modifications.

- Zeng *et al.* assembled a coin cell, in which they used $\text{MgH}_2\text{-LiBH}_4$ composite material (prepared by high energy ball milling) as negative electrode and LiBH_4 as a solid electrolyte and *Li*-foil as a cathode [66]. The first discharge/charge profile showed a high reversible capacity of 1650 mAhg^{-1} with a very low polarization of 0.05V with an excellent cyclability and rate capability. Additionally, thermogravimetric measurements (TG-DTA) were performed to investigate the thermal stability of the $\text{MgH}_2\text{-LiBH}_4$ composite, which indicated a weight loss of less than 1 wt% at room temperature to 275°C .
- Dao and co-workers investigated the electrochemical properties of $\text{MgH}_2\text{-TiH}_2$ nanocomposites as an active material with different molar ratios and LiBH_4 as a solid electrolyte in LIB [123]. In this study, a coin cell was assembled by using lithium as a negative electrode, LiBH_4 as a solid electrolyte and $\text{MgH}_2\text{-TiH}_2$ nanocomposite as a positive electrode. The galvanostatic discharge/charge measurements were performed at 120°C under 0.05-1V at a rate of C/50. This study was based on the nanocomposites as a function of molar ratio. Hence the initial reversible capacity was found to be more than 1700 mAhg^{-1} from *Mg*-rich nanocomposites (*e.g.*, $0.7 \text{ MgH}_2+0.3 \text{ TiH}_2$), whereas TiH_2 rich composites ($0.2 \text{ MgH}_2+0.8 \text{ TiH}_2$) revealed better cycling stability. Overall an excellent electrochemical performance of $\text{MgH}_2\text{-TiH}_2$ was obtained by the use of solid electrolyte LiBH_4 and high operating temperature.
- Huen *et al.* investigated the electrochemical performance of Mg_2FeH_6 in solid-state *Li*-ion batteries using LiBH_4 as a solid electrolyte and compared it with the standard liquid electrolyte [124]. Mg_2FeH_6 was prepared by ball milling method in the presence of *Mg* and *Fe* in a 2:1 molar ratio. The cyclic measurements were performed under 0.3-1.0V at C/50 rate for solid-state LIB, while the conventional battery was tested between 0.2-1.0V. Although initial discharge profile exhibited an excellent specific capacity as 1100 mAhg^{-1} in conventional LIB, it decayed rapidly to 90 mAhg^{-1} after ten repeated cycles with a low coulombic efficiency of $\sim 27\%$ only. Interestingly, the coulombic efficiency was increased

to 67% in solid-state LIB as compared with the previous reports [125], [126] and after 10th cycles, the capacity was more than three times higher than conventional liquid electrolyte based battery.

As per the reports mentioned above, LiBH₄ works as an excellent solid electrolyte due to its high conductivity in its high-temperature phase (>120°C). Further improvement in the room temperature (RT) conductivity of LiBH₄-based materials is still highly desired for their practical applications [127], [128]. Modifying LiBH₄ is one essential strategy to increase the *Li*-ion conductivity at RT.

3.1 Introduction

This chapter describes the procedure adopted for the preparation and characterization of anode composite materials using bulk and/or nano *Bi* & Bi_2X_3 ($\text{X} = \text{S}, \text{Se}, \& \text{Te}$), Lithium borohydride (LiBH_4), and conductive carbon (Acetylene Black AB) for *Li*-ion battery application. The procedure for assembling the coin cell using solid-state electrolyte LiBH_4 is also described step by step. Also, the details of used materials, equipment, and approved protocols for the synthesis of Bi_2X_3 based nanostructured anodes are also presented herein. Since characterization techniques are an essential part of the research work to understand the properties of the materials and their applications, so all the characterization tools employed for analyzing the various properties of the anode materials in this work are discussed in terms of their principle and the necessary details.

3.2 Materials

All the raw materials/chemicals, used for the synthesis of the nanostructured anode material, for the preparation of anode composite materials are listed herein in **Table 3.1**:

Table 3.1: List of chemicals used in this thesis work

S. No.	Raw Materials	Chemical Formula	Brand	Purity (%)
1	Bismuth	<i>Bi</i>	Alfa Aesar	99.999%
2	Lithium borohydride	LiBH_4	Sigma Aldrich	95%
3	Bismuth Telluride	Bi_2Te_3	Alfa Aesar	99.98%
4	Bismuth Selenide	Bi_2Se_3	Alfa Aesar	99.995%
5	Bismuth Sulfide	Bi_2S_3	Alfa Aesar	99.9%
6	Bismuth Chloride	BiCl_3	Aldrich	98%

S. No.	Raw Materials	Chemical Formula	Brand	Purity (%)
7	Tellurium Powder	<i>Te</i>	Aldrich	99%
8	Sodium Ethylenediaminetetraacetate	Na ₂ -EDTA (C ₁₀ H ₁₄ N ₂ Na ₂ O ₈ .2H ₂ O)	Scientific	98%
9	Sodium Hydroxide	NaOH	Fisher Scientific	97%
10	Sodium Borohydride	NaBH ₄	Loba Chemie	97%
11	Hydrazine hydrate	N ₂ H ₄	Fisher Scientific	99%
12	N,N-Dimethylformamide	DMF	Emplura	99%
13	Selenium dioxide	SeO ₂	Sigma Aldrich	99.8%
14	Polyvinyl pyrrolidone	PVP	Loba chemie	95%
15	Sodium Tellurite	Na ₂ O ₃ Te	Alfa Aesar	99.5%
16	Thiourea	CH ₄ N ₂ S	CDH	97%
17	Triethanolamine	(HOCH ₂ CH ₂) ₃ N	Emplura	99%
18	Bismuth Nitrate Pentahydrate	Bi(NO ₃) ₃ .5H ₂ O	Loba Chemie	99.99%
19	Ethylene Glycol	C ₂ H ₆ O ₂	Emplura	99%
20	Ethanol	C ₂ H ₅ OH	Analytical	99.9%
21	Selenium powder	<i>Se</i> (pellets < 5mm)	Aldrich	> 99.99%
22	Ammonium Chloride	NH ₄ Cl	Fisher Scientific	99%
23	Sodium o - dodecyl benzenesulfonate; Dodecyl benzene sulfonic acid	SDBS	Loba Chemie	98%

3.3 Methods to synthesized the nanostructured materials

In present work, the hydrothermal and solvothermal methods were used to prepare different morphologies of Bi₂X₃. The present section describes the details of these methods.

3.3.1 Hydrothermal method

The hydrothermal synthesis method is a well-known process for the nanomaterial formation, which is based on solution reaction. In this method, the morphology of nanomaterials can be controlled by altering the synthesis conditions such as room temperature to high temperature, low pressure to high-pressure conditions, depending upon the vapor pressure of the main composition in the reaction. A schematic of sample synthesis is shown in **Figure 3.1**. There are various significant advantages of the hydrothermal synthesis method over others, such as:

- (1) The compositions of the nanomaterials can be well controlled during hydrothermal synthesis along with liquid phase or multiphase chemical reactions.
- (2) The morphology of the nanomaterials can be easily controlled by variation of parameters like temperature and pressure.
- (3) The loss of materials during synthesis is minimum in this method as compared to others.
- (4) The hydrothermal method can also synthesize those nanomaterials, which are not stable at elevated temperatures.

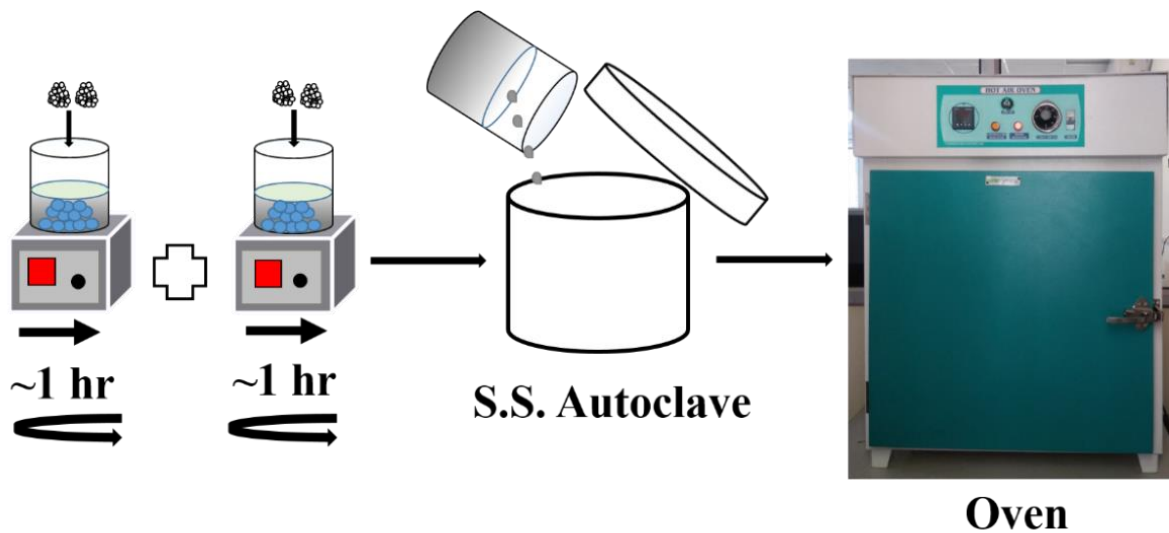


Figure 3.1: Schematic of sample synthesis by hydrothermal method.

3.3.2 Solvothermal method

Similar to the hydrothermal method, the solvothermal method is defined as a process of performing chemical reactions in the solvent contained in a sealed vessel. The only difference between the hydrothermal method and solvothermal method is based on the solvent used in the process. The use of water as solvent termed the method as a hydrothermal method, whereas the use of organic liquids as a solvent makes it a solvothermal method.

3.4 Synthesis of Bi_2X_3 ($\text{X} = \text{S}, \text{Se}, \& \text{Te}$) nanostructures

3.4.1 Bi_2S_3 nanoflowers

The hydrothermal method was used to synthesize the Bi_2S_3 nanoflowers [129]. Bismuth nitrate pentahydrate (0.61g) and thiourea (0.25 g) were first dissolved into 60 ml deionized (DI) water. To form a homogeneous solution, the obtained solution was stirred at 250 rpm for 1hr. After stirring, the solution was transferred into a Teflon lined stainless steel autoclave with a capacity of

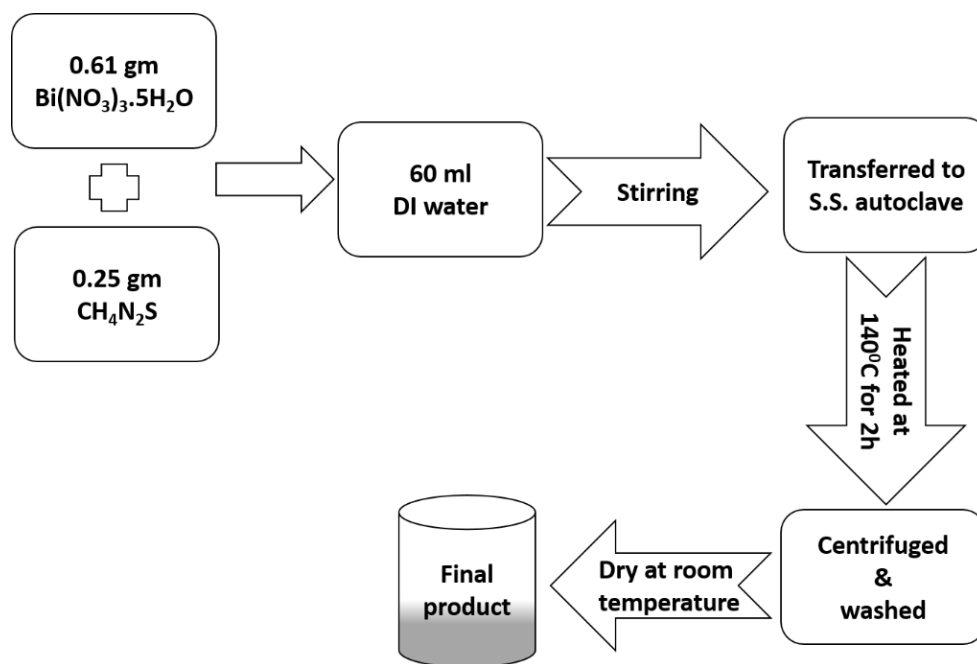


Figure 3.2: Schematic for the synthesis of Bi_2S_3 nanoflowers.

100 ml. The autoclave was then sealed and heated at 140°C for two hours. After the chemical reaction, the autoclave was cooled down to room temperature. Finally, the black color precipitate was collected by filtration and washed with deionized water and ethanol several times, then dried at room temperature before characterizations. A schematic of the sample preparation is shown in **Figure 3.2**.

3.4.2 Bi₂Se₃ mixed morphology (nanoparticles & nanosheets)

Bi₂Se₃ nanostructures were prepared by the solvothermal method[130]. To prepare the Bi₂Se₃ nanostructures, Bi(NO₃)₃·5H₂O (2.6 mmol) was triturated in triethanolamine (complexing agent) and was stirred for 15 min continuously. Then 15 mmol of NaOH was dissolved in DMF, and 7.4 mmol of Se powder was added to it under the constant stirring condition for 1.5 hr, followed by the addition of hydrazine hydrate (reducing agent). The resultant solution was transferred into a Teflon-lined autoclave of 100 ml capacity filled with 80 ml DMF. After that, the

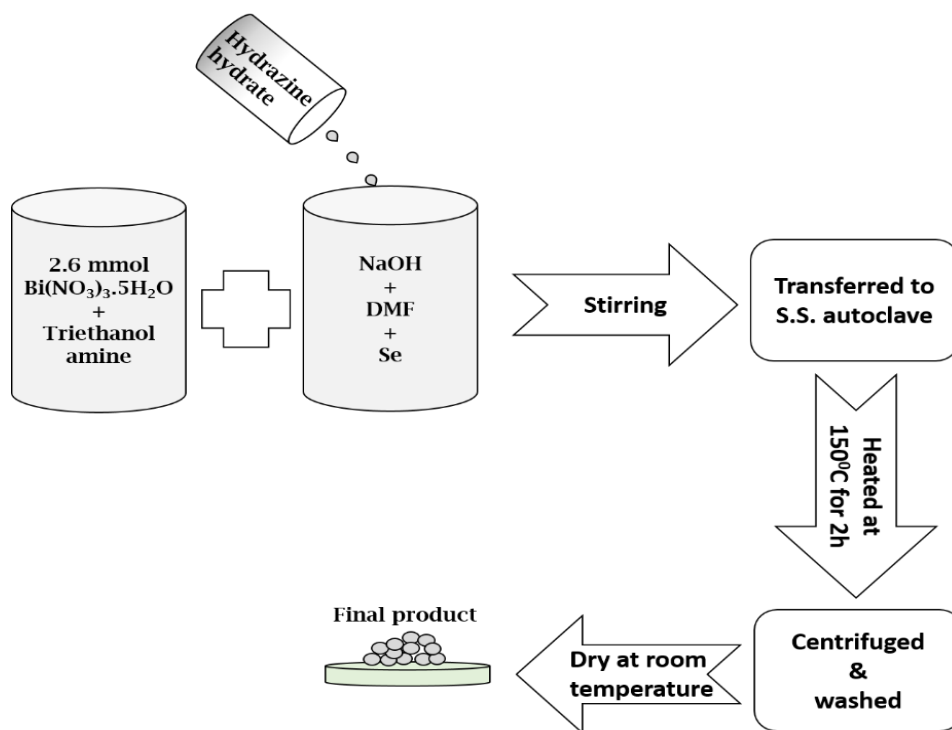


Figure 3.3: Schematic for the synthesis of Bi₂Se₃ nanostructures.

autoclave was sealed and kept at 150°C for 2h, followed by cooling to room temperature (**Figure 3.3**). The black precipitate was carefully collected after filtration, then washed with deionized water and ethanol several times, and finally dried at room temperature before characterizations.

3.4.3 Bi₂Te₃ nanorods

The Bi₂Te₃ nanorods were synthesized by the hydrothermal method [131]. The complete process of the nanostructure synthesis is shown in **Figure 3.4**. High purity (99.99%) bismuth chloride (BiCl₃) (75.67 mg), tellurium (*Te*) powder (45.93 mg) and 1g sodium ethylenediaminetetraacetate (Na₂-EDTA) were dissolved in 60 ml deionized (DI) water. The resulting mixture was stirred at 250 rpm for 10 min. Meanwhile, 0.8 g sodium hydroxide (NaOH) was dissolved in 0.8 g sodium borohydride (NaBH₄) in another 100 ml beaker and put on stirring for 30 min. To achieve the final precursor, both the solutions were quickly mixed and transferred to the Teflon lined autoclave. The autoclave was then sealed and heated at 180°C for 27 hrs. The autoclave was cooled down to room temperature (naturally) after the chemical reaction. The obtained black color precipitate was collected by filtration and washed with deionized water and ethanol several times, then dried at room temperature before characterizations.

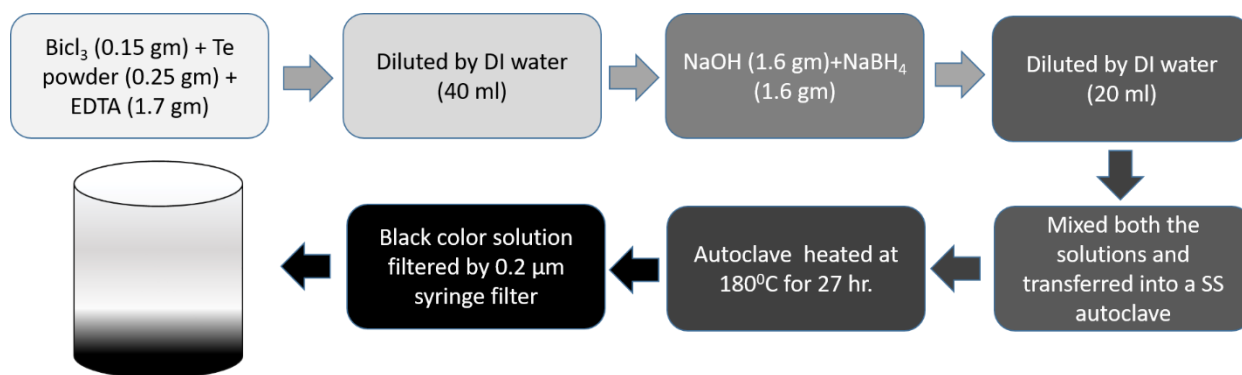


Figure 3.4: Schematic for the synthesis of Bi₂Te₃ nanorods.

3.5 Characterization techniques

3.5.1 Scanning Electron Microscopy (SEM)

SEM is an electron microscope launched in 1938 by Von Ardenne, and some additional features of scanning were added in 1965. Electron microscopy is relevant and promising microscopy technique over other light microscopes due to its high magnification and resolving power. For procuring the morphological information of the required sample, highly energetic electron beams interact with the sample surface. A focused beam of electrons is expended for producing signals on the sample surface. During the electron-sample interaction, some specific signals are obtained to provide information about the morphology, topology, chemical composition, etc. of the material. To avoid the scattering of the electrons during the experiment, the arrangement of the scanning system is kept vacuum isolated. The schematic diagram of the SEM is shown in **Figure 3.5**.

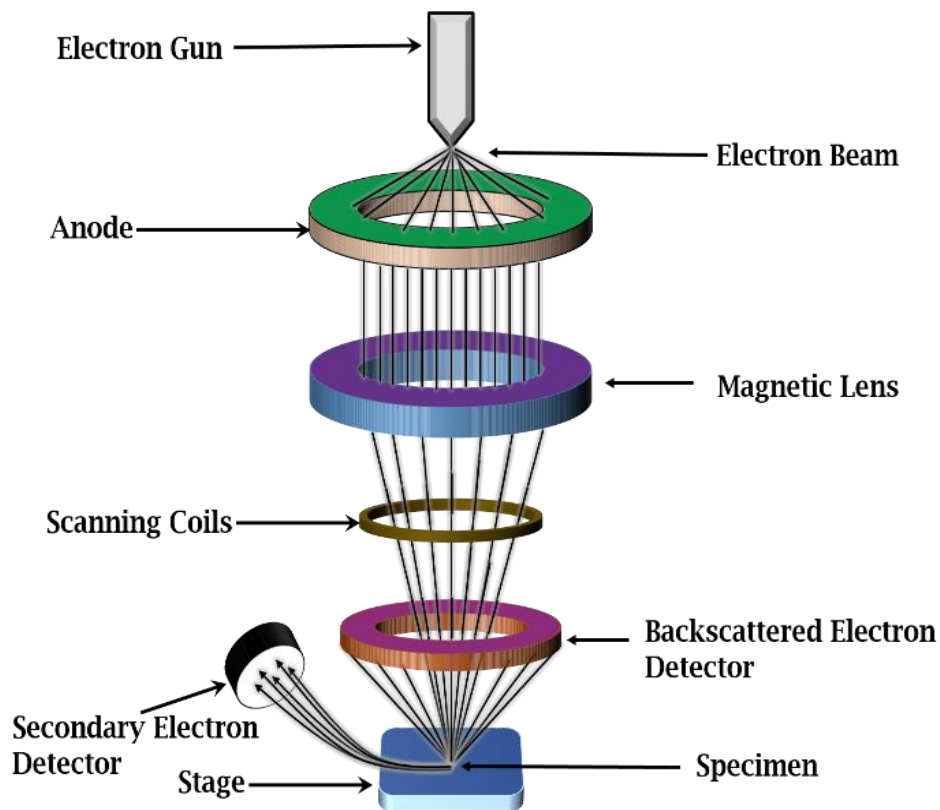


Figure 3.5: Schematic diagram of SEM.

The wavelength of the electron beam can be regulated easily with operating voltage. Operating voltage precedes to accelerate the electrons in the direction of the sample. In this instrument, a source of monochromatic electron beam known as electron gun is placed at the top. The electron beam is passed through a vertical path and focused on the material surface using electromagnetic field generated through two condenser lenses. The first condenser lens is used to control the electron beam and exclude the high-angle electrons from the electron beam while the second lens is used to form very reedy, tight, and coherent beam [132]. Mainly, there are two types of mode deliberated for scanning the image, *i.e.*, secondary electron mode and backscattered electron mode.

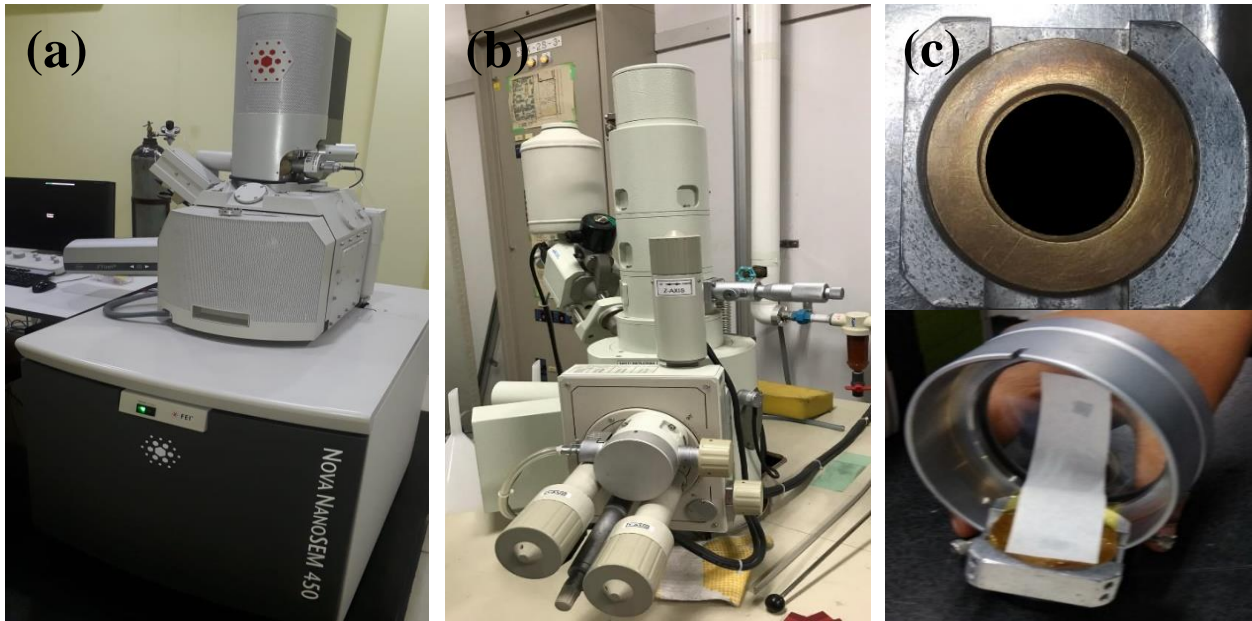


Figure 3.6: Digital images of the SEM instrument (a) NOVA NANO SEM 450 (b) JEOL JSM 6380 (c) SEM holder with a covered sample by polyimide sheet.

The secondary electron mode is one of the most common modes for imaging in high resolution with a full description of the surface morphology of the sample. On the other hand, backscattered electron images are used to a quick assessment of phases in multiphase samples. A detector that produces the final image accumulates secondary and backscattered electrons. There are some limitations of SEM, *e.g.*, the particular dimension of the sample; sample must be solid,

an electrically conductive coating is necessary for the insulating samples, operated only in a vacuum.

In this thesis work, Bi_2X_3 ($\text{X} = \text{Te}, \text{Se}, \& \text{S}$) nanostructures, *i.e.*, nanoparticles, nanorods, nanosheets, and nanoflowers were characterized by SEM (Nova Nano FE-SEM 450 FEI) with an accelerating voltage of 15 kV. In addition to it, another instrument JEOL JSM 6380 was used to observe the surface morphology of anode material before and after the electrochemical cycling (used instrument images are shown in **Figure 3.6**).

3.5.2 Transmission Electron Microscopy (TEM)

TEM is another esteemed technique to investigate the crystallinity and intermolecular arrangements of the sample. To perform TEM measurements, the sample needs to be very thin, less than 100 nm; so that, electrons can easily pass through the samples. TEM systems have three essential parts: (1) an electron gun, which provides electron beam along with condenser lens system, which centers the beam onto the sample (2) the image processing system, including the objective lens, movable specimen stage, and standard and projector lenses. Projector lenses focus the electron beam passing through the specimen to form a real and highly magnified image, and (3) image recording system, converts the electron image into some form perceptible to the human eye. **Figure 3.7** exhibits the schematic diagram of TEM. The sharp electron beam is accelerated by a high potential anode with the potential $\sim 100\text{-}400$ kV, generated by an electron gun, which consists a filament, primary circuit, and extraction anode. LaB_6 and tungsten filaments are typically used due to their low work function and high melting point.

In principle, when a collimated (by the different magnetic lenses) beam incident on the sample, then these electrons are either scattered or transmitted through the sample. After transmission, these electrons fall on the CCD sensor which response to form a very high-resolution image of the sample. Excellent control of the electron beam is managed by the different condenser/objective lens assembly, and a magnificent electron beam is obtained which can travel through the specimen and collect the information about the sample [132]. Generally, the TEM system is working on two imaging mode: (a) Bright-field image mode, (b) Darkfield image mode. Most commonly bright-field image mode is used for the microstructural analysis, while the dark field image is used when the direct beam is blocked by the aperture and pass one or more diffracted beam. Interplanner

spacing and the lattice planes can be easily identified by selected area diffraction pattern (SAED) mode [133]. The wavelength of the incident electron beam can be easily controlled by the accelerating voltage as

$$\lambda = h/p = 12.25 \times 10^{-10} / \sqrt{V} \quad (1)$$

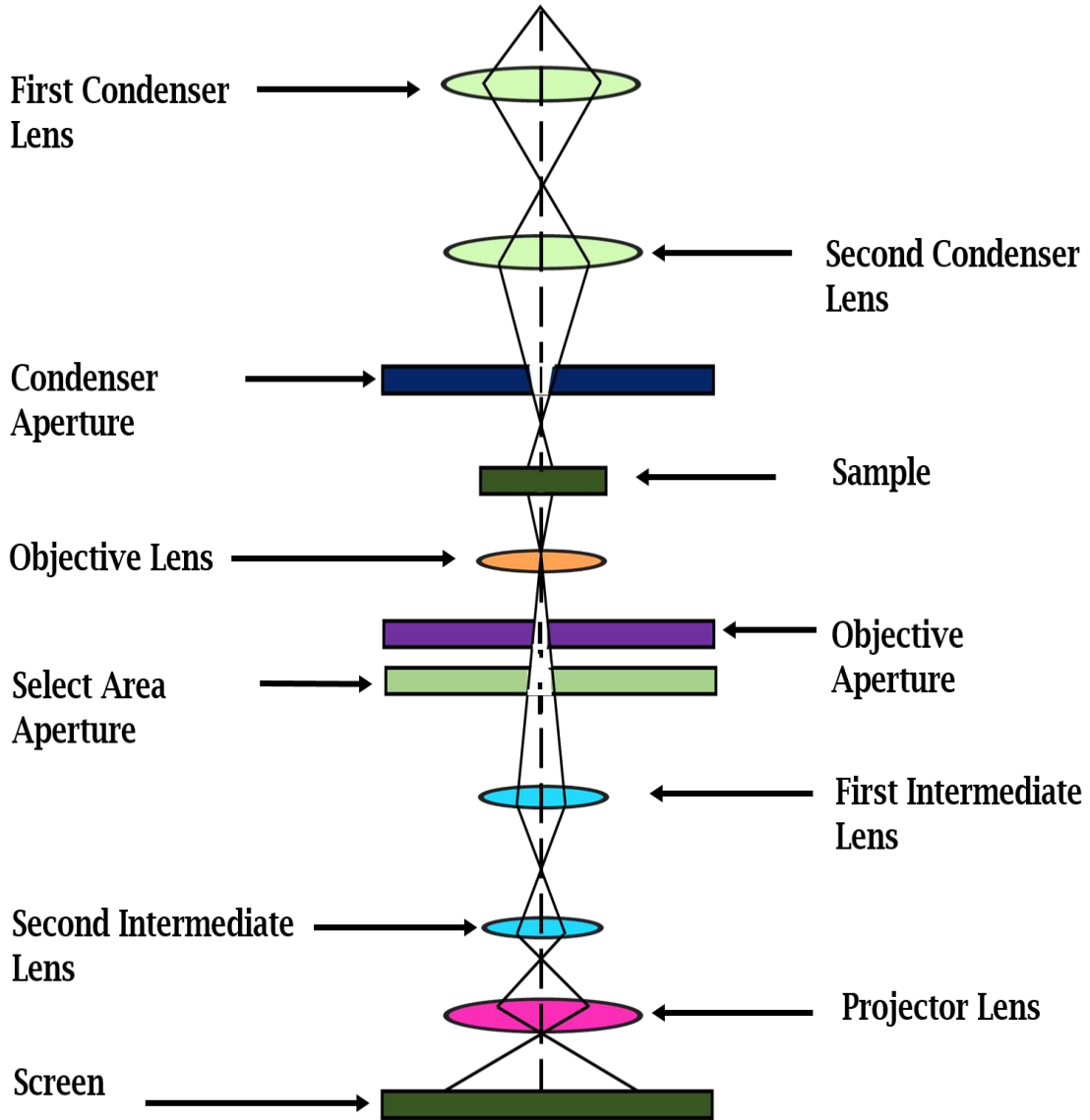


Figure 3.7: Schematic diagram of the TEM instrument.

Herein, Technai T20 FEI system which operates at 200 kV, equivalent to 2.51 pm wavelength was used for TEM experiments to analyze the nanostructure morphology, size, and distribution with crystallinity (as shown in **Figure 3.8**).



Figure 3.8: Digital image of TECHNAI T20 FEI TEM instrument.

3.5.3 X-ray Diffraction Spectroscopy (XRD)

X-ray diffraction is a fundamental technique which is used for the study of crystal structures and atomic spacing. In 1912, Max von Laue discovered that crystalline material act as three-dimensional diffraction gratings for X-ray wavelengths which are of the same order of the spacing of planes in a crystal lattice. XRD is based on the constructive interference of the monochromatic X-rays diffracted through a crystalline sample. These X-rays are produced by a cathode ray tube,

filtered and collimated to focus and directed to the sample. According to the Bragg's law, a monochromatic X-ray beam incident on the specimen at an angle θ and diffracted with 2θ angle (as shown in **Figure 3.9**). The path difference between the incident beam and the diffracted beam gives information about the occurrence of constructive interference or destructive interference [134]. Constructive interference occurs when the interaction between the incident X-rays and the sample satisfies the conditions of Bragg's Law

$$n\lambda = 2d \sin\theta \quad (2)$$

Where, n = order of reflection, λ = wavelength of incident X-rays, d = interatomic spacing between lattice plane and θ = diffraction angle.

Bragg's law establishes a relation between the wavelength of electromagnetic radiation to the diffraction angle and the lattice spacing in a crystalline sample. The diffracted beam is collected by the detector and gives the crystallographic knowledge about the lattice structure.

The average crystallite size of the nanostructures can be calculated by the following equation known as Debye-Scherrer's formula [135]:

$$D = \frac{0.9\lambda}{\beta \cos\theta} \quad (3)$$

Where, λ = wavelength of X-rays, β = full width at half maxima of a diffracted peak, θ = diffraction angle.

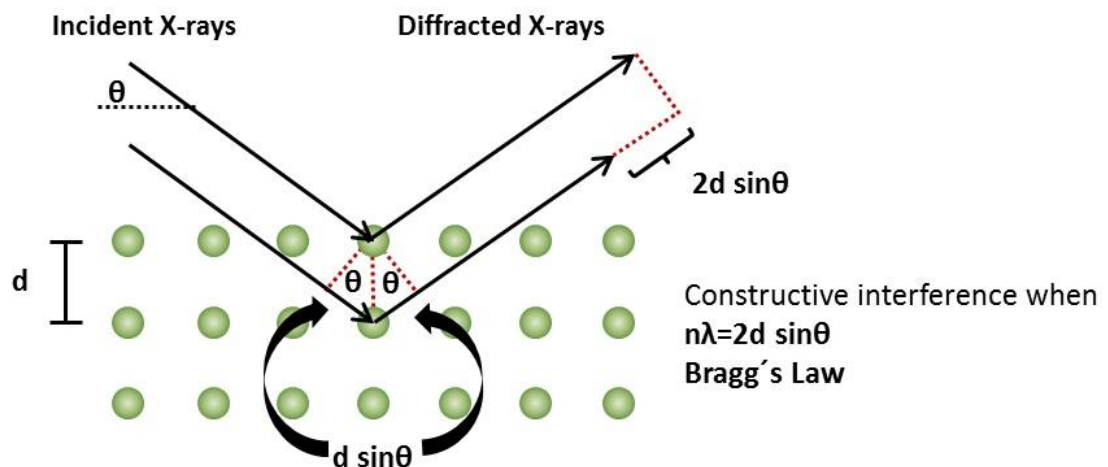


Figure 3.9: Schematic representation of the Bragg's equation.

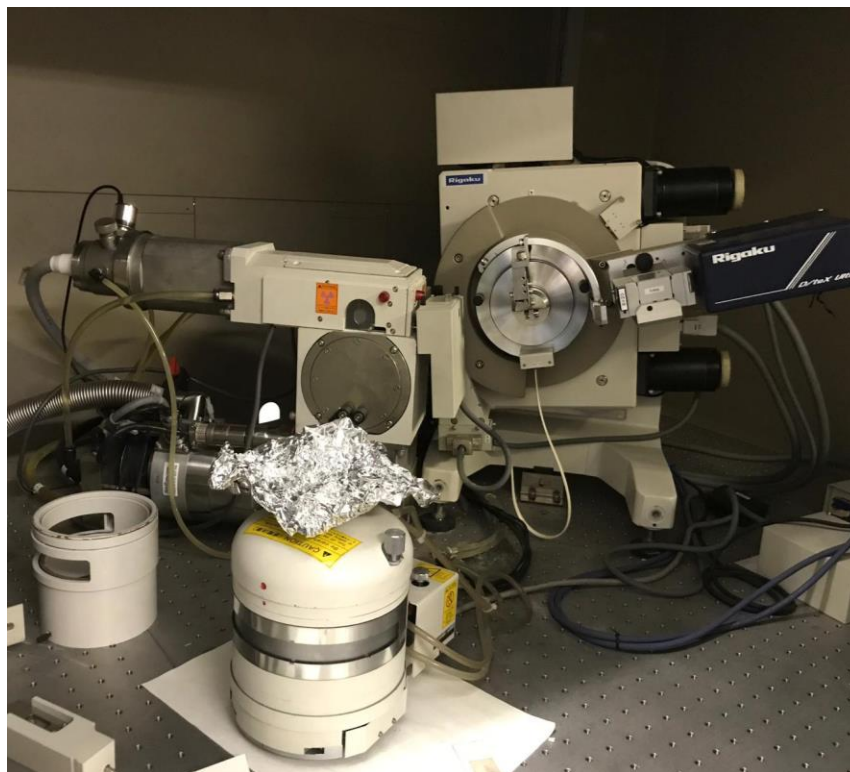


Figure 3.10: Digital image of Rigaku-RINT 2500 XRD system.

In this thesis, all the sample handling was done in high purity Ar-filled glove box. All the materials used in this work are characterized for their structure by X-ray diffraction (XRD) using a Rigaku-RINT 2500 diffractometer equipped with $\text{CuK}\alpha$ radiation (as shown in **Figure 3.10**). The samples were covered by a polyimide sheet (Dupont-Toray Co. Ltd., Kapton) to protect them from atmospheric exposure.

3.6 All solid state *Li*-ion Battery fabrication

3.6.1 Preparation of Negative Electrode (Anode)

To investigate the electrochemical properties of the *Bi*-based anode material with a solid electrolyte, firstly, anode composite materials were prepared by high energy ball milling method. A hardened stainless steel milling pot was used with 10 SS balls of 7 mm diameter for the preparation of 200 mg sample. The milling was performed at 370 rpm using Fritsch P7 milling machine (as shown in **Figure 3.11**) for a total of 2 hours milling with a 1hour work and 30 min

rest pattern. In this process, active material Bi & Bi_2X_3 , AB, and $LiBH_4$ (Sigma Aldrich, 95%) were used in the weight ratio of 40:30:30. Before preparation of anode composite material, $LiBH_4$ and AB were dried under vacuum at $200^\circ C$ & $300^\circ C$ respectively to avoid all the moisture content. All the handling of materials during preparation was done in Ar-filled glove box with oxygen and moisture content less than 1 ppm.

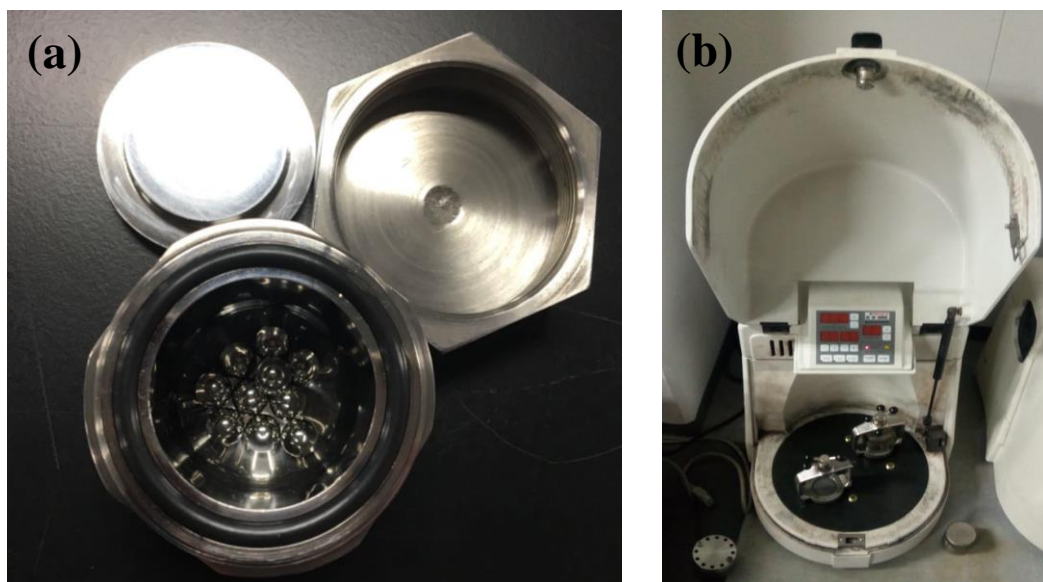


Figure 3.11: A hardened stainless steel milling pot with 10 SS balls (a) and Fritsch P7 milling machine (b).

3.6.2 Fabrication of half coin cell

A coin cell was assembled in an argon-filled glove box with oxygen and moisture level less than 1 ppm. A coin cell consists of several parts, as shown in **Figure 3.12 (a)**. Apart from the assembling parts, the working electrode-electrolyte assembly was fabricated by using a three-layer pellet. This three-layered pellet was prepared in a Die of diameter 15 mm, and a plunger is used to press the sample. First, Li -foil with a thickness of 0.1 mm on SS plate (diameter 15.5 mm and thickness 0.52 mm) was used as the first layer, which works as a cathode. The second layer was prepared by spreading the solid electrolyte $LiBH_4$ (around 80 mg) on Li -foil and applying a uniform pressure of 10 MPa for 5 min. At last, the prepared anode composite powder (around 10

mg) was spread on the two-layered pellet and pressed under 40 MPa pressure for 5 min. A uniform pellet of diameter 15 mm was obtained, which was placed and sealed in a coin cell using Perfluoroalkoxy (PFA) gasket by a crimping machine. The assembled coin cells are taken out for charge/discharge measurements. An overall assembly of various parts of the coin cell and the digital image of the used glove box are shown in **Figure 3.12**.

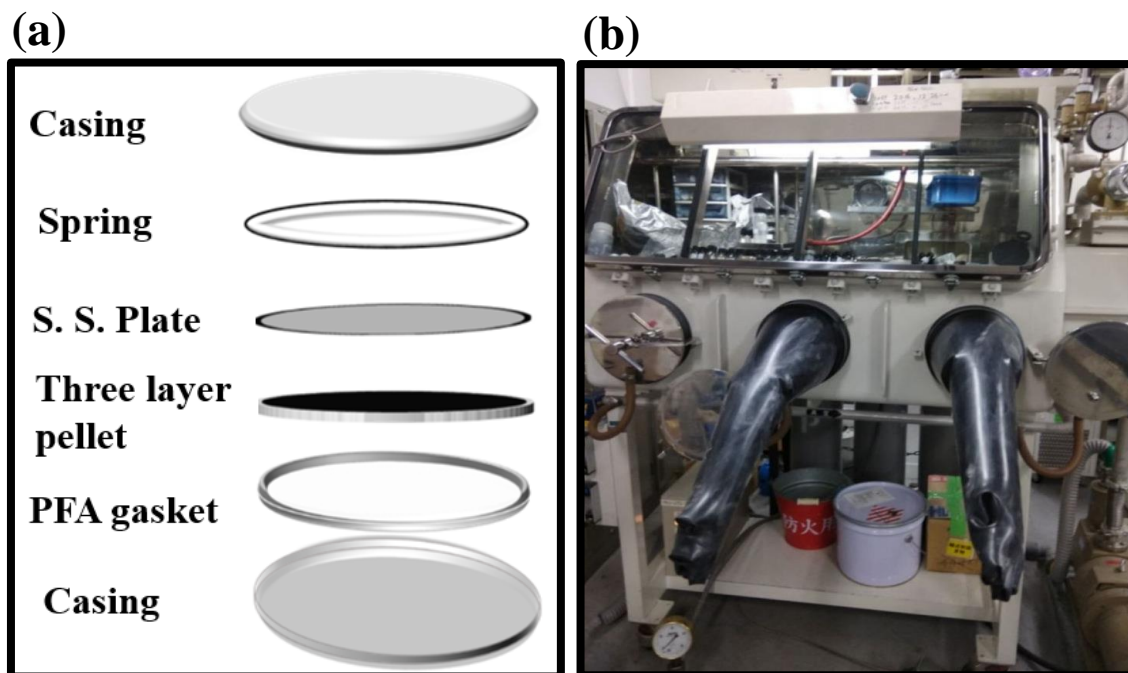


Figure 3.12: (a) Schematic diagram of various parts for the coin cell assembly and (b) digital photograph of the glove box.

3.7 Electrochemical Characterizations

3.7.1 Cyclic Voltammetry (CV)

Cyclic voltammetry is an electrochemical method to study the electrode processes and measure the current versus voltage, which develops in an electrochemical cell under the conditions predicted by the Nernst equation [136]:

$$E = E^0 - \ln Q_c \frac{RT}{nF}$$

Where E = Cell potential under given conditions

E^0 = Standard cell potential

R = Universal gas constant (8.314 J/mol-K)

T = Temperature in kelvin

n = Number of electrons transferred in the half cell reaction

F = Faraday's constant (95,484.56 C/mol)

Q_c = Reaction quotient of the cell reaction

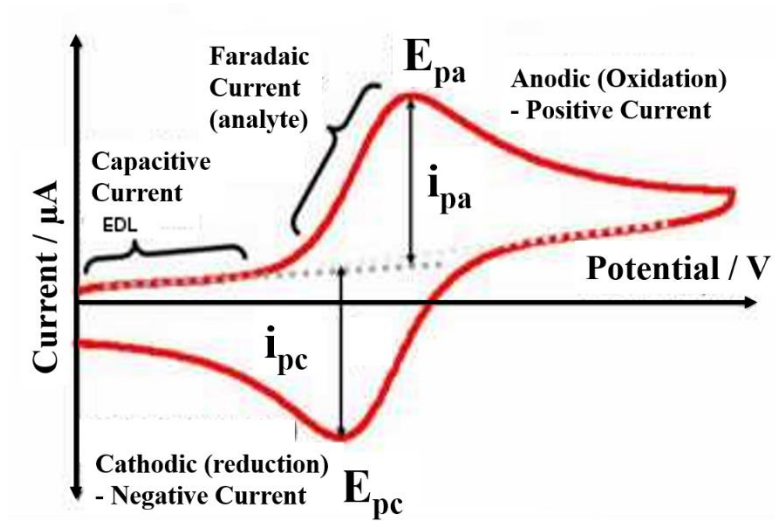


Figure 3.13: Schematic representation of Cyclic Voltammetry.

Cyclic voltammetry is generally employed as the primary technique to characterize the new system. This method is widely used for observing the electrode processes, such as the determination of the kinetics and thermodynamics of the electron transfer at the electrode-electrolyte interface. To observe the electrochemical cycling performance of the cell, an optimized potential window is required, in which the cell is to be cycled. The optimized potential is applied to the working electrode and continuously changed at a constant rate known as the scan rate. The potential sweep can be described by its initial, switching, and final potentials as well as the scan rate. To avoid the electrolyte decomposition, the choice of this potential window should be decided based on the stability range of the chosen electrolyte [137]. In CV plot, the current flow versus the potential is measured, which gives the information about an increment in the current response

at the potential where an electrochemical reaction takes place. A schematic representative of CV is shown in **Figure 3.13**. As per the graph (**Figure 3.13**), the obtained curves under and above the zero line is for the discharging (or cathodic) and charging (or anodic), respectively, of the anode material. The total amount of charge flow is proportional to the surface under the curve. Oxidation and reduction of the working electrode are originated due to a positive and negative sweep rate, respectively.

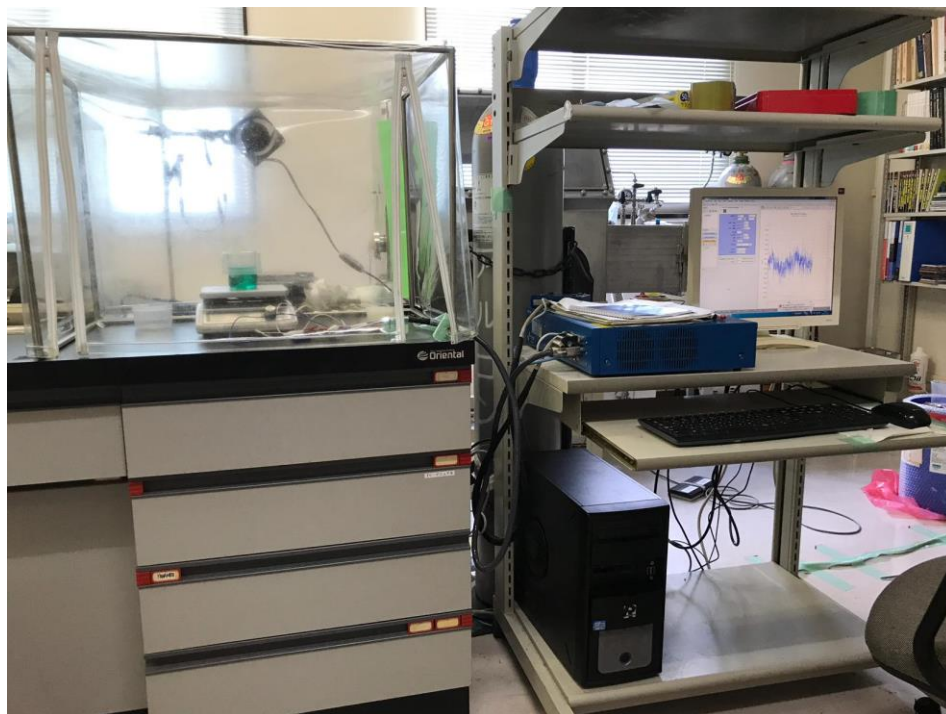


Figure 3.14: Digital image of Bio-Logic SAS (SP-150) system for CV measurements.

In this study, the cyclic voltammetry was performed on the assembled coin cell using a Biologic SAS (SP-150) system (as shown in **Figure 3.14**). All the CV measurements were done at 120 °C by using a silicon oil bath as a heating source.

3.7.2 Galvanostatic discharge - charge experiments

Galvanostatic discharge-charge testing is used to investigate the battery capacity, cyclic performance, and the rate capability of the electrode material under a constant current density. This

characterization tool gives a plot between the specific capacity and voltage, which gives information about the suitable operational condition and the performance. In addition, the specific capacity can also be plotted as a function of cycle number, indicating the cycle life of the anode material. The charge-discharge capacities can be obtained by this formula:

$$Q = I \times t \quad (1)$$

Where, Q = capacity, I = current density, and t = charge-discharge time

A cut-off potential should be pre-determined to discharge the cell with a constant current, and the voltage response exhibits the changes in the electrode processes observing at its interface. A constant current applied to the electrode causes the oxidation or reduction at a constant rate. The potential shifts towards the characteristic value of the Ox/Red couple, which differ with time by varying the ratio between the concentrations of the oxidized and reduced species at the electrode surface[138].

Herein, the galvanostatic discharge-charge testing voltage window was used as 0.2 V – 2.5 V for anode materials. The C-rate was optimized by performing discharging charging curves at different discharge/charge current densities. In this work, all the electrochemical measurements were done by a charge-discharge analyzer ((HJ1001SD8, Hokuto Denko Co.). To obtain the fast Li^+ conduction from $LiBH_4$, the discharge/charge measurements were done at 120°C; thus a silicon oil bath has been used as a heating source, and the required setup is shown in **Figure 3.15**.



Figure 3.15: Digital image of charge-discharge setup.

3.8 Summary

This chapter summarizes the information about the preparation of anode composite materials with bulk and nanostructured based active materials followed by the assembly of half coin cell. The adopted methods and the used techniques for the analysis of the prepared anode composite material and fabricated all-solid-state *Li*-ion battery have also been discussed here.

Chapter Four

Bismuth as a Promising Anode for Li-ion Batteries

4.1 Introduction

At present, rechargeable LIBs are fascinating power sources for mobile devices. Although its market has also expanded to large scale applications like energy storage systems for grid support and electric vehicles, the safety issues due to the use of organic liquid electrolyte, still need to be solved. All-solid-state LIBs are evolving rapidly due to their advantages over conventional liquid electrolyte based LIBs in terms of safety, stability, and energy density [60], [139], [140]. However, all-solid-state battery suffers from the most significant challenges, *i.e.*, their low current drains/low power density, which originates from the low ionic conductivity of the solid electrolytes. Considerable research has focused on identifying those solid electrolytes which have high ionic conductivity. However, none of them led to the high performance of solid-state LIBs. Recently, LiBH_4 has attracted much more attention as a solid electrolyte due to its high ionic conductivity, which was observed in the order of 10^{-3} Scm^{-1} at its high temperature (HT) phase at 390K [61], [139]. LiBH_4 has been successfully employed as an electrolyte for hydride based anode materials so far [64], [65]. It was believed that the reaction kinetics is improved because of H-H exchange between LiBH_4 and the hydride materials [141]. Besides of hydride, other electrode materials need to be explored with LiBH_4 , in order to extend its use as a universal solid electrolyte. To date, carbon-based material has been widely accepted as commercial anode material although, it has several limitations, *e.g.* , its low specific capacity, safety issues, and limited cycle life [142]. In order to replace the graphite, several alternative anode materials such as *Si, Ge, Sn, P*, metal oxides, *etc.* have attracted more attention due to the formation of the alloy in a much higher mole ratio at safer potentials and these anodes can deliver much higher capacities *i.e.* 2-10 times more than that of commercially adopted graphite [143]. As compared to the other group elements, bismuth (*Bi*) has been considered as a favorable anode material for LIBs since it is diagonally related to Sn and reveals relatively more stability in the moisture/air atmosphere at room temperature than other alloying materials. *Bi* has a comparable gravimetric capacity of about 386 mAhg^{-1} to that of the

commercially available carbon anode (372 mAhg^{-1}) [32]; whereas, it has a benefit of substantially high volumetric capacity (3765 mAhcm^{-3}), which is 4 fold higher than the carbon ($840.72 \text{ mAhcm}^{-3}$). It is important to note that the volumetric capacity is equally important as the gravimetric capacity for various practical stationary as well as portable applications of battery systems like electronic mobile devices and electronic vehicles *etc.*

The above key points make it a promising anode material for LIBs, and several studies have been carried out to improve its properties as a negative electrode. Although *Bi* has been studied with different liquid electrolytes so far, it is not employed in all-solid-state batteries yet to the best of our knowledge. In the present chapter, we have investigated the first ever electrochemical performance of all-solid-state *Li*-ion battery using *Bi* as anode and LiBH_4 as a solid electrolyte [144].

4.2 Cyclic voltammetry

Cyclic voltammetry is a potentiodynamic electrochemical measurement technique, which is used to investigate the electrochemical behavior of an electrode within a certain potential range. CV measurements are used to study the mass and electron transport properties of the materials. Any system which exhibits rapid oxidation/reduction reaction with electrode material is termed as a reversible electrochemical couple. Electrochemical properties of the *Bi*-based anode composite material have been tested through Cyclic Voltammetry (CV) analysis. **Figure 4.1** shows the CV scan profile of the *Bi*/ LiBH_4 /AB composite electrode at 0.1 mVs^{-1} between 0.2V to 1.5V (Li^+/Li) potential window, which was decided according to the theoretical potential for the lithiation of *Bi* [34], [35]. The open-circuit voltage (OCV) of the cell was observed as 1.27 V. Initially, during the discharging/lithiation scan of *Bi*/ LiBH_4 /AB composite electrode, two cathodic/reduction peaks were observed at 0.79V and 0.72V, which are expected to be the alloying reaction of *Bi* to LiBi and finally to Li_3Bi phases, respectively as per the theoretical voltage values. A broad peak with a very small current variation was also observed in between 0.6 – 0.2V, which corresponded to the lithiation of carbon, presented in the composite material. In reverse scan/during the charging process, no broad peak was observed unlike to the discharge reaction. The anodic/oxidation peaks at 0.85V and 0.88V correspond to the delithiation reactions of Li_3Bi returning to metallic *Bi*-phase through the formation of LiBi phase as an intermediate state. Herein, the CV scan profile exhibited

all the oxidation and reduction peaks in between 0.2V – 1.5V potential window, which was used as an evidence to perform all the electrochemical measurements under this potential window [144].

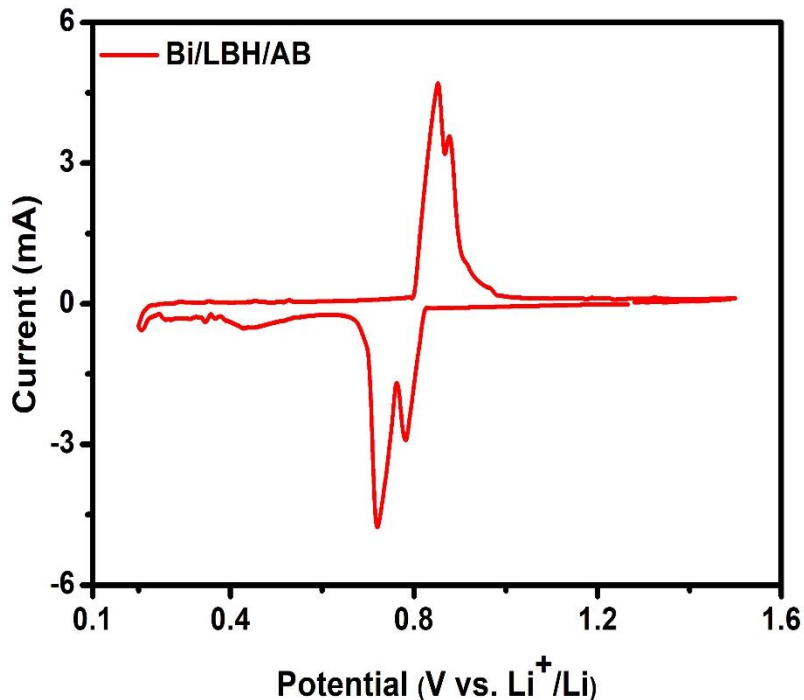


Figure 4.1: Cyclic Voltammogram of Bi composite electrode scanned at 0.1mVs⁻¹.

4.3 Galvanostatic discharge/charge

An assembled coin cell has a specific open-circuit voltage, but in battery operation, it reveals different cell voltages under the discharging and charging processes. A cell exhibits a lower cell voltage in a discharging process, due to the internal impedance which derives from the polarization at the electrodes and the ohmic resistance in the current collectors, electrolyte and active materials. The polarization losses occur at each electrode, while the ohmic resistance exists in the circuit of batteries. **Figure 4.2** exhibits the typical galvanostatic discharge–charge profile of Bi-LiBH₄-AB composite electrode in the first cycle between the potential window 0.2 - 1.5 V vs. Li^+/Li at 0.1C rate. The initial discharge and charge capacity of the Bi-LiBH₄-AB composite was observed as 4681.7 mAhcm⁻³ (478.7 mAhg⁻¹) and 4510.5 mAhcm⁻³ (461.2 mAhg⁻¹) respectively, with a coulombic efficiency of 96.3%. The obtained capacity for Bi-LiBH₄-AB composite was slightly

higher than the theoretical value, which could be attributed to the side reaction / the contribution from carbon lithiation. The polarization between *Li*-insertion and extraction was <0.1V, which was much smaller than that of the *Bi*-electrodes with an organic liquid-based electrolyte. Such a low polarization could be achieved by the fast diffusion of species and the high working temperature of 120°C, which brings better kinetic properties to the *Bi* alloying reaction. Two voltage plateaus at 0.82V and 0.78V were obtained during discharge scan. Similarly, during charging, both the plateaus occurred exactly in the opposite direction. The electrochemical reaction mechanism behind these obtained plateaus was investigated through the *ex-situ* XRD measurements at different potentials / capacities.

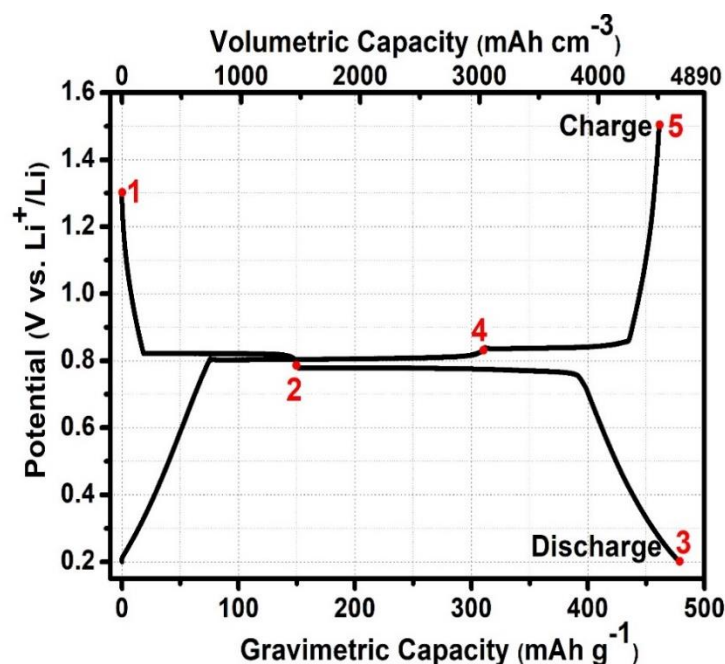


Figure 4.2: The initial galvanostatic discharge-charge profile for *Bi-LiBH₄-AB* composite negative electrode.

4.4 Mechanism of lithiation/delithiation of *Bi*-anode in all-solid-state *Li*-ion battery

Ex-situ XRD measurements were performed at the specified potentials, as shown by numbers 1, 2, 3, 4, and 5 in the galvanostatic discharging/charging profile (**Figure 4.2**) to understand the

mechanism behind the obtained plateaus. In addition to the other phases at different points, the XRD pattern exhibited the peaks corresponding to LiBH_4 for all the points, which was due to the presence of LiBH_4 in anode composite material with a sufficient amount (30%) as well as an electrolyte. In the XRD pattern of prepared anode composite material corresponding to point 1, all

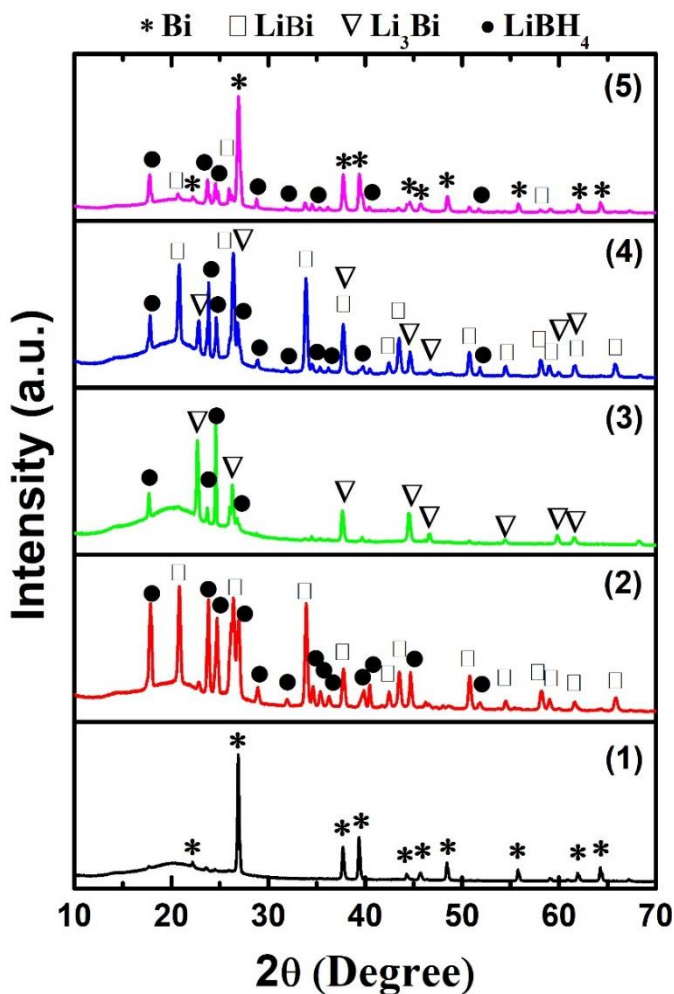
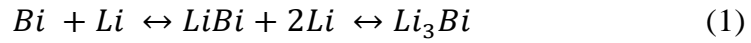


Figure 4.3: Ex-situ XRD patterns of Bi- LiBH_4 -AB composite electrodes at different stages (indicated in Figure 2) of the first electrochemical discharge – charge process.

the high-intensity peaks could be indexed to *Bi*, suggesting no reaction between the components of anode composite material. Initial discharge profile showed that on the discharge curve (Li^+ incorporation into *Bi*), the potential gradually dropped to around 0.82 V showing a long flat plateau

until point 2, where the *Li*-ion moved from the positive electrode (cathode) to negative electrode (anode) and reacted with *Bi* and made LiBi phase (**Figure 4.3**, Point 2). The next discharge plateau was observed at 0.78V, immediately after the 1st plateau and very close to it. This plateau ended with a capacity of 400 mAhg⁻¹, after which the voltage gradually reduced to 0.2V at point 3, corresponding to the LiBi → Li₃Bi reaction as according to XRD profile (**Figure 4.3**, point 3). The opposite reaction occurred precisely in the opposite direction during charging, as observed from the presence of two plateaus during the charging process (*Li*⁺ extraction) and XRD profiles at point 4 & 5 of charging curve, which suggested high reversibility of the reaction *Li* ↔ Li₃Bi. The above results indicated that the existence of LiBH₄ significantly promotes the *Bi* alloying reaction, as shown in equation (1), resulting in a low polarization and a high coulombic efficiency.



4.5 Cyclic stability measurements

Cyclic stability of Bi-LiBH₄-AB composite electrode was investigated for 100 cycles under the potential window 0.2V-1.5V at a 0.1C rate, to further explore the capability of the prepared composite electrodes in practical applications. **Figure 4.4 (a)** shows the cyclic galvanostatic discharge-charge profiles of Bi-LiBH₄-AB composite electrode up to 100 cycles. The capacity was found to decrease down to 3853.3 mAhc⁻³ (394 mAhg⁻¹) after 100 cycles from 4681.7 mAhc⁻³ (478.7 mAhg⁻¹) in the first cycle, which is only 18%. **Figure 4.4 (b)** represents the stable coulombic efficiency with unchanged plateau potential over several cycles suggesting the superior performance of *Bi* anode in the all-solid-state battery. The capacity became almost stable after 70 cycles. On comparing these results with the available reports, it can clearly be seen that Bi-LiBH₄-AB composite electrode has shown a drastic improvement in the cyclic stability with very high capacity in comparison to the bare *Bi* nanoparticles with liquid electrolyte [LiPF₆ in ethyl methyl carbonate (EMC)/ ethylene carbonate (EC)/ diethyl carbonate (DEC)] where it exhibits poor cyclic stability and retains only 60 mAhg⁻¹ after 100 cycles [34]. Also, the commercially available bulk *Bi-C* electrode shows a large capacity decay from~ 650 mAhg⁻¹ to around 200 mAhg⁻¹ after 100 cycles [35].

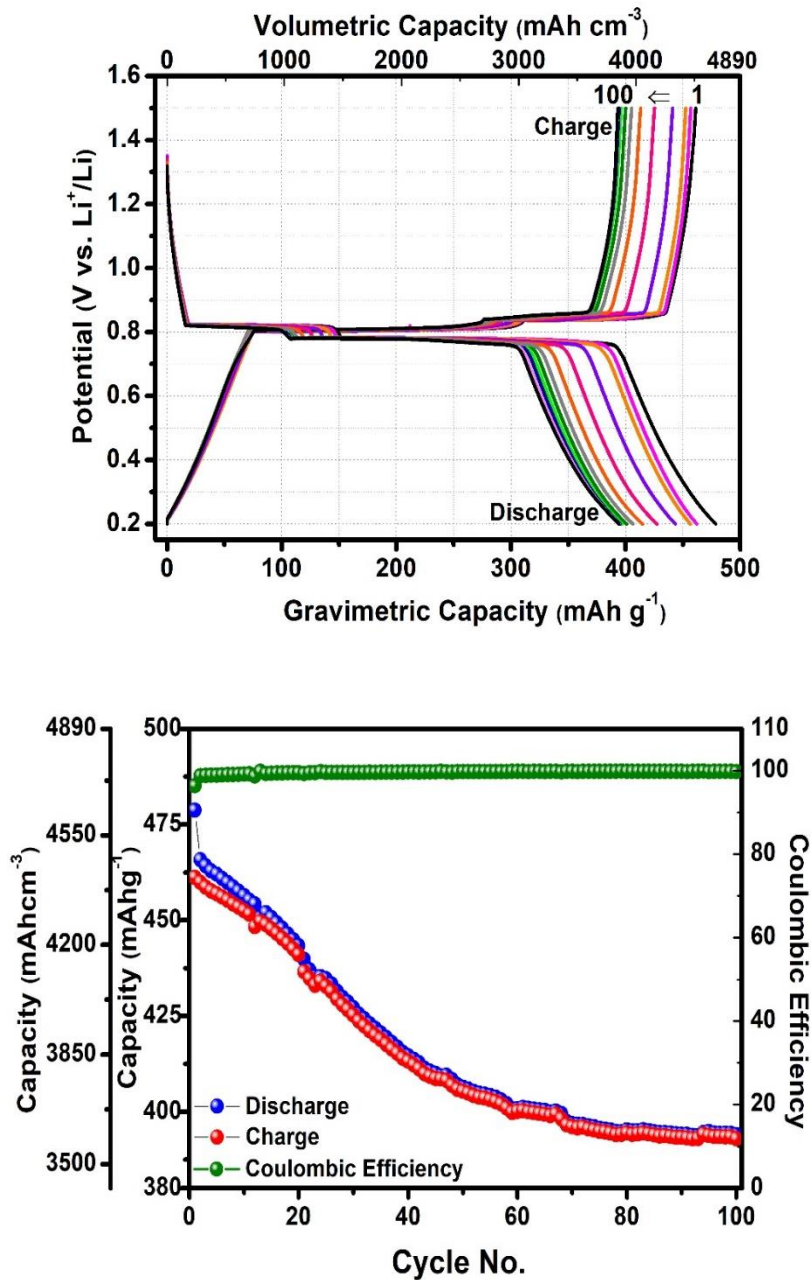


Figure 4.4: (a) The Cyclic galvanostatic discharge-charge profiles for Bi-LiBH₄-AB composite electrodes in the voltage range of 0.2-1.5V at 0.1C. Only selected cycles (1,5,10,20,30,40,50,60,70,80,90,100) are shown for clear visibility. (b) Cyclic stability of Bi-LiBH₄-AB composite electrodes as shown by Discharge/Charge capacity and the coulombic efficiency vs. cycle number.

4.6 Morphological investigations of *Bi*-anode

The biggest problem with these anode materials is the large volume expansion and contraction associated with $Bi \leftrightarrow Li_3Bi$ transformation during the electrochemical cycling. This volume change generates several cracks in the electrode and causes the loss of physical connectivity between electrodes and electrolytes [39], [81]. To observe the actual condition of the negative electrode, SEM studies were performed on the coin cell before and after cycling. **Figure 4.5** shows the SEM micrographs and elemental mapping of the Bi-LiBH₄-AB composite electrode before cycling. No cracks were observed before cycling, and the elemental mapping suggested that *Bi* was present homogeneously throughout the electrode.

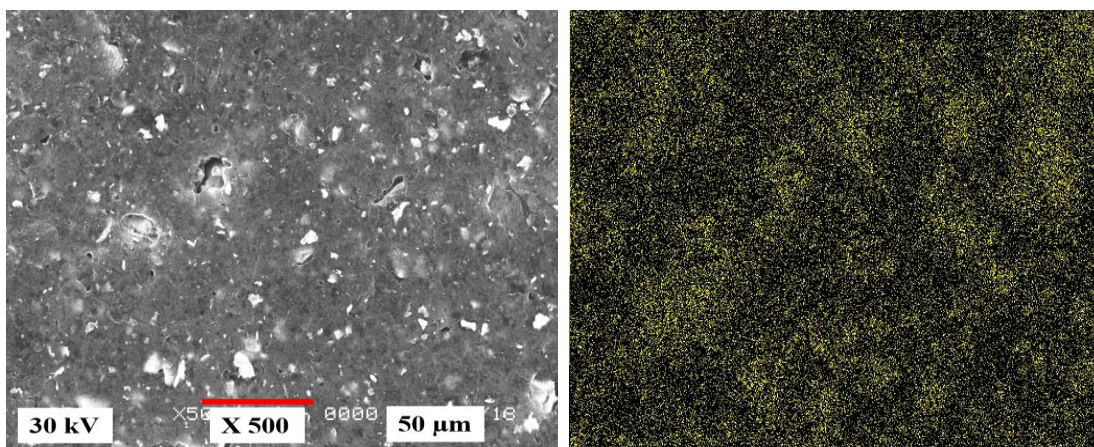


Figure 4.5: SEM images and corresponding elemental mapping of *Bi* in the composite electrode surface before cycling.

A smooth crack free surface could be observed even after cycling (**Figure 4.6**). The elemental mapping suggested homogeneous distribution of *Bi* throughout the electrode surface even after cycling. It might be due to the presence of LiBH₄ in the electrode which along with carbon (AB) works as a binder and provides a cushioning effect. It consequently helps to accommodate the volume change comfortably, which drastically improves the cyclic stability.

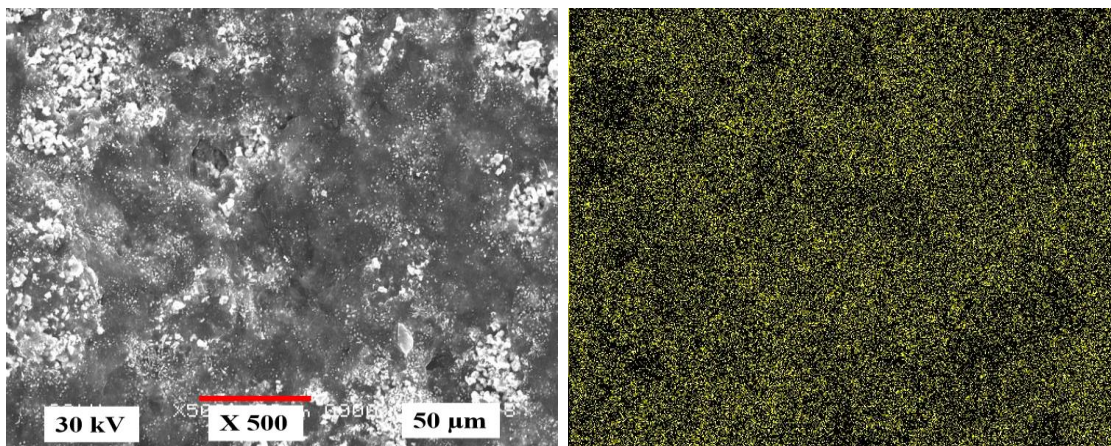


Figure 4.6: SEM images and corresponding elemental mapping of Bi in the composite electrode surface after cycling.

4.7 Summary

In this chapter electrochemical reaction mechanism between *Li*-ion & *Bi*-based anode for all-solid-state *Li*-ion battery was established successfully. The cyclic stability performance of *Bi*-based anode with LiBH_4 as a solid electrolyte has also been investigated. In summary, it could be concluded that this anode material exhibits outstanding volumetric capacity and superior stability. LiBH_4 and AB, contained in the composite electrode material, provides the high stability to this system due to the cushioning effect apart from the enhancement in the ionic & electrical conductivity of the anode material. It is worth to mention here that a hydride-based (LiBH_4) electrolyte with the *Bi*-based anode materials was investigated for the first time. This opens up a path to utilize it to other high capacity anode materials and can be helpful for the development of rechargeable LIBs with high-safety.

Chapter Five

Investigation of Bulk Bi_2X_3 ($X = S, Se, \& Te$) as Highly Durable Anode Materials

5.1 Introduction

The growth of portable electronic devices and hybrid electric vehicles (HEVs) has generated an increased demand for batteries with a large gravimetric as well as volumetric capacity. In this regard, rechargeable lithium-ion batteries (LIBs) have been widely studied because of their high energy density, high rate capability, and environmentally friendly nature [12]. The high energy efficiency of LIBs may also allow their use in various electric grid applications, including the improvement of energy quality harvested from wind, solar, geothermal and other renewable sources, thus contributing to their more widespread use and building an energy-sustainable economy. Therefore LIBs are having intense interest from both industry and government funding agencies, and research in this field has abounded in recent years [46].

Although LIBs have the highest energy density, they typically suffer from low power by reversible coulombic reactions occurring at both electrodes, involving charge transfer and ion diffusion in bulk electrode materials [145]. Hence LIBs which can be used in hybrid electric vehicles and pure electric vehicles, require two to five times the higher energy density than the present LIBs. The increased energy density can be achieved by either using high voltage cathode active materials as electrodes or by developing new high capacity anode materials. The negative electrode is an inherent component in batteries to enhance their energy and power density [146]. However, due to lack of electronically superior conductivity and high electrochemical stability, most of the materials are unsuitable as an electrode in LIBs [28]. In particular, a carbon-based material, *i.e.*, graphite is the most commonly used anode in commercial LIBs. However, it has various limitations such as its low gravimetric and volumetric capacities (372 mAhg^{-1} & $840.72 \text{ mAhcm}^{-3}$ respectively), and safety issues because of its low reaction potential with *Li* for LIBs. Therefore, it is essential to introduce other suitable anode materials to deliver the high energy density, high specific capacity, and higher potential to react with *Li*. Recently, several metals,

including *Si*, *Sn*, *Sb*, *Ge*, *Al*, and *Bi*, have been attracting much more attention as an anode material because of their high theoretical capacities compared to graphite. The elements *Si*, *Sn*, *Sb*, *Al*, and *Ge* have very high theoretical gravimetric capacity than the commercially available graphite through the formation of $\text{SiLi}_{4.4}$ (4200 mAhg^{-1}), $\text{SnLi}_{4.4}$ (993 mAhg^{-1}), SbLi_3 (660 mAhg^{-1}), LiAl (994 mAhg^{-1}) and $\text{Li}_{2.2}\text{Ge}_5$ (1600 mAhg^{-1}) as well as high volumetric capacities as 2190 mAhcm^{-3} , 1991 mAhcm^{-3} , 1889 mAhcm^{-3} , 1383 mAhcm^{-3} , and 2180 mAhcm^{-3} respectively as compared to graphite (756 mAhcm^{-3}) [147], [148] which is also necessary parameter for the electric vehicles. Besides these metals, *Bi* delivers a high volumetric capacity of 3765 mAhcm^{-3} (far higher than other metal anodes and four-fold higher than graphite), due to its unique layered crystal structure that can provide a sufficient interlayer spacing to accommodate *Li*-ions and to generate Li_3Bi [81], [149], [150]. The high volumetric capacity of *Bi* makes it attractive for the applications of portable electronics, mobile electric and electric/hybrid devices, *etc.* or where high volumetric energy densities are required [80], [151], [152]. However, as observed in the previous chapter, its specific capacity (385 mAhg^{-1}) is not so high, thus to fix this issue, *Bi*-based materials as Bi_2X_3 ($\text{X} = \text{O}$, *Se*, & *S*) have been intensively studied as a negative electrode with liquid electrolytes in the last few years. According to the available reports, Bi_2X_3 compounds exhibit high volumetric ($\sim 4000 - 6000 \text{ mAhcm}^{-3}$) as well as gravimetric capacities ($\sim 400 - 700 \text{ mAhg}^{-1}$) [110], [153], [154]. Similar to the mechanism in the materials mentioned above, bismuth telluride (Bi_2Te_3) can also electrochemically store *Li* reversibly by forming the Li_3Bi and Li_2Te composition [39]. Although there are several studies on the electrochemical performance of these materials, these are limited to the use of liquid electrolyte only.

Herein, the bulk Bi_2X_3 ($\text{X} = \text{S}$, *Se*, & *Te*) has been investigated as an active anode material in combination with solid electrolyte (LiBH_4) in order to enhance the specific capacity as well as volumetric capacity. In this chapter, electrochemical performance of all-solid-state LIB having Bi_2X_3 as anode and LiBH_4 as a solid electrolyte have been discussed [155]–[157]. A complete electrochemical reaction mechanism was also established in between Bi_2X_3 and *Li*-ions. All the electrochemical measurements in this work were performed at 125°C to obtain the fast Li^+ conduction through LiBH_4 [62].

5.2 Structural investigations of as prepared Bi_2X_3 anode composites

Figure 5.1(a) shows the XRD pattern of as purchased bulk Bi_2S_3 (Sigma Aldrich with 99% purity), in which all the obtained diffraction peaks can be well indexed to the trigonal Bi_2S_3 (JCPDS: 01-089-8963) with R-3m (166) symmetry [155]. The XRD analysis revealed the lattice parameters as $a = b = 4.143\text{\AA}$, $c = 28.636\text{\AA}$. The obtained sharp peaks designated the good crystallinity of the sample without the presence of any impurity phases. **Figure 5.1(b)** shows the XRD pattern of prepared composite anode material with as-received bulk Bi_2S_3 , heat-treated acetylene black (AB) and heat-treated LiBH_4 . It was observed that a mechanochemical reaction took place during the milling as evident from the presence of Bi and Li_2S peaks in addition to the starting material, *i.e.*, Bi_2S_3 & LiBH_4 .

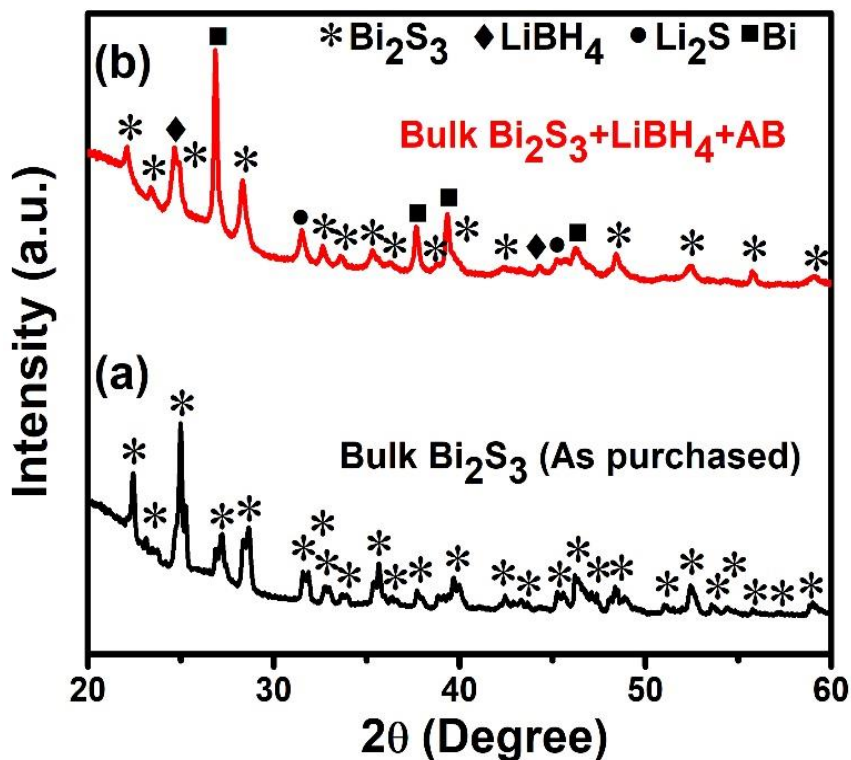


Figure 5.1: XRD patterns of (a) bulk Bi_2S_3 and (b) Bi_2S_3 - LiBH_4 -AB composite electrode.

The XRD pattern of as purchased bulk Bi_2Se_3 (Alfa Aesar with a purity of 99.995%) is shown in **Figure 5.2 (a)**. All the obtained diffraction peaks were corresponding to the trigonal Bi_2Se_3

(JCPDS card no. 01-089-2008) with (R3m) symmetry with the lattice parameters $a = b = 4.143 \text{ \AA}$, $c = 28.636 \text{ \AA}$ [156]. The observed sharp peaks depicted that the sample has good crystallinity. **Figure 5.2 (b)** shows the XRD pattern of prepared composite anode material by using purchased bulk Bi_2Se_3 , heat-treated AB, and heat-treated LiBH_4 . The individual peaks of both Bi_2Se_3 and LiBH_4 components confirmed no chemical reaction had taken place at the time of milling.

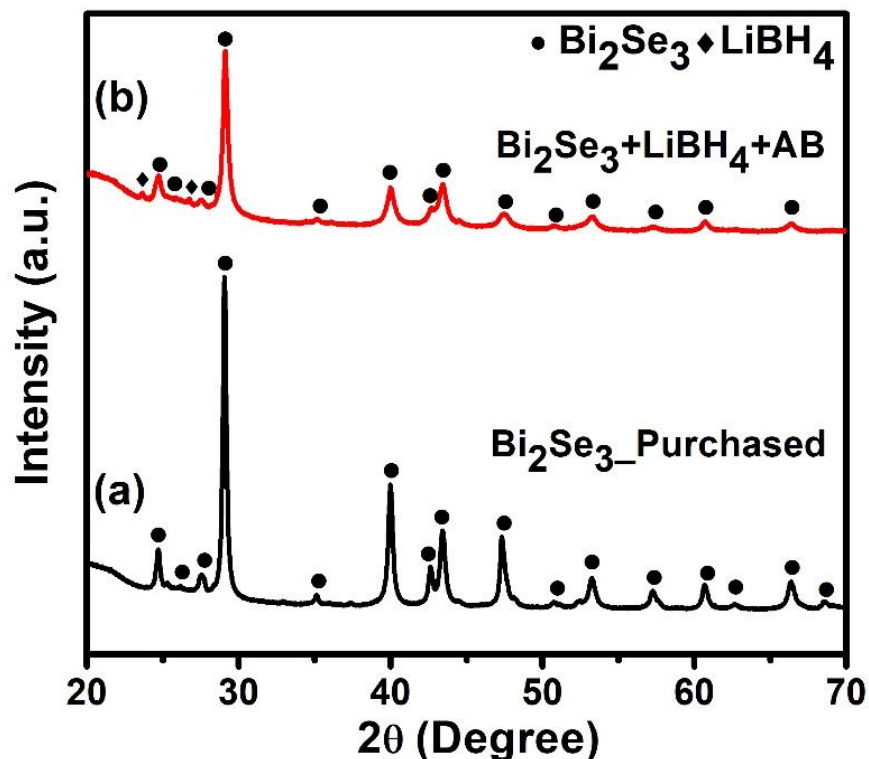


Figure 5.2: XRD patterns of (a) bulk Bi_2Se_3 and (b) $\text{Bi}_2\text{Se}_3\text{-LiBH}_4\text{-AB}$ composite electrode.

The XRD pattern as shown in **Figure 5.3 (a)** could be indexed to the Bi_2Te_3 phase (JCPDS no. 01-082-0358) with trigonal (R3m) symmetry and the noticeable sharp peaks indicated that the sample has good crystallinity [157]. As shown in **Figure 5.3 (b)**, the presence of individual peaks corresponding to trigonal Bi_2Te_3 (JCPDS no. 01-082-0358) and LiBH_4 (JCPDS no. 01-070-9017) confirmed that no reaction occurred between them during milling. The peak intensity corresponding to the LiBH_4 phase was relatively low in comparison to the peaks of Bi_2X_3 in all these patterns, which must be due to the low scattering factor of LiBH_4 .

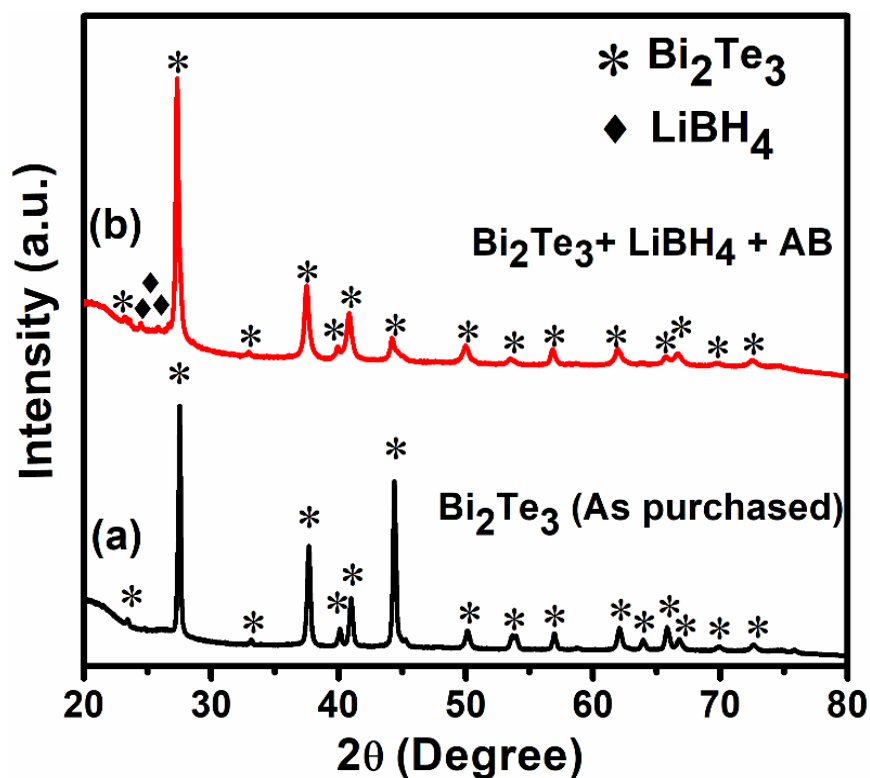


Figure 5.3: XRD patterns of (a) bulk Bi_2Te_3 and (b) $\text{Bi}_2\text{Te}_3\text{-LiBH}_4\text{-AB}$ composite electrode.

5.3 Cyclic voltammetry

Figure 5.4 shows the CV scan profile for the bulk Bi_2X_3 , which is obtained in between 0.2 – 2.5 V (Li^+/Li) potential window at a scan rate of 0.1 mVs^{-1} . The open-circuit voltages (OCV) of the cells containing bulk Bi_2S_3 , Bi_2Se_3 , and Bi_2Te_3 composite electrode material were 1.56 V, 1.76V, and 1.56V, respectively. Figure 5.4 (a) depicts the cyclic voltammogram of bulk Bi_2S_3 -based composite electrode sample. In the first cathodic scan of the bulk sample, a slightly weak peak at 1.42V could be ascribed to the Li_2S formation, while the peaks at 0.79 V and 0.72 V were due to the formation of LiBi followed by Li_3Bi phase. On the other hand, the reverse anodic scan process showed two peaks around 0.85 V and 0.88 V corresponding to the delithiation of Li_3Bi to LiBi and Bi respectively. Further delithiation gave rise to a broad peak with much noise between 1.86 – 2.01 V corresponding to the transformation of Li_2S to S . However, the noise in this reason suggested the possibility of additional side reactions to the electrochemical reaction. CV profile of bulk Bi_2Se_3 sample is presented in Figure 5.4 (b).

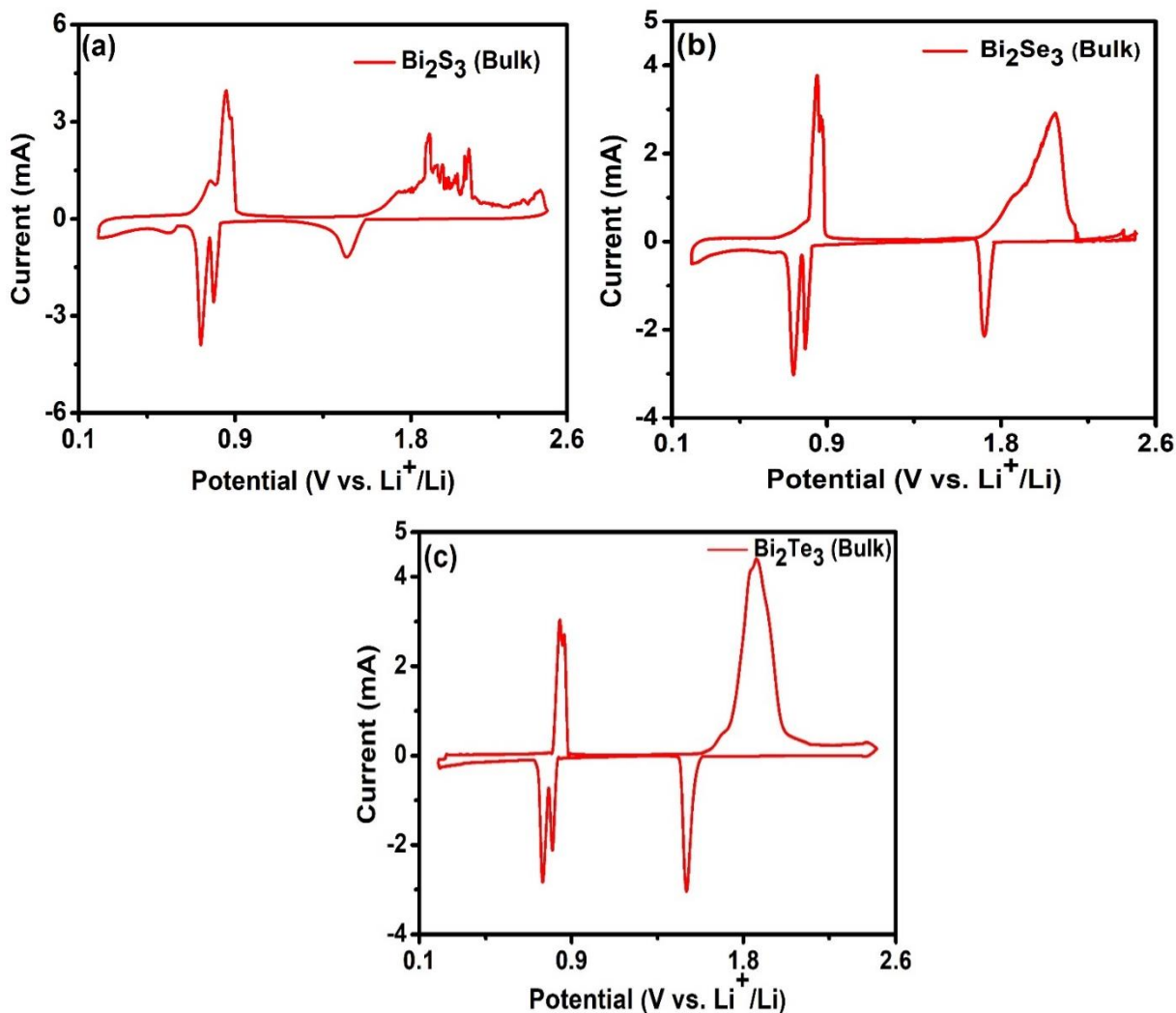


Figure 5.4: Cyclic Voltammograms of bulk (a) $\text{Bi}_2\text{S}_3\text{-LiBH}_4\text{-AB}$ (b) $\text{Bi}_2\text{Se}_3\text{-LiBH}_4\text{-AB}$ (c) $\text{Bi}_2\text{Te}_3\text{-LiBH}_4\text{-AB}$ composite anode material scanned at 0.1 mVs^{-1} .

The open-circuit voltage (OCV) of the cell, containing the bulk Bi_2Se_3 composite anode was observed to be 1.76 V. It showed the first discharging peak at 1.71 V corresponding to Li_2Se formation followed by two peaks around 0.78 V and 0.72 V corresponding to the lithiation of *Bi* to form LiBi and Li_3Bi successively. During the reverse scan, *i.e.*, charging process, two peaks appear at 0.84 V and 0.87 V corresponding to delithiation of Li_3Bi and LiBi . A broad peak, which possibly corresponding to the transformation of Li_2Se to *Se*, appeared in the voltage range of 1.7 – 2.2 V.

Similar to Bi_2S_3 and Bi_2Se_3 , CV measurements were also performed on Bi_2Te_3 electrodes to optimize a suitable potential window for all electrochemical studies. **Figure 5.4 (c)** shows the CV scan profile of the Bi_2Te_3 electrodes. At first, during the lithiation (Discharging) scan of $\text{Bi}_2\text{Te}_3/\text{LiBH}_4/\text{AB}$ electrode, the first cathodic peak, located at 1.5 V could be ascribed to the Li_2Te formation, while the others peaks at 0.8 V and 0.74 V were expected due to the alloying reaction of *Bi* to LiBi and Li_3Bi phases, respectively as per the theoretical voltage values. During the charging process, anodic peaks at 0.83V and 0.86V exhibited the delithiation reactions of Li_3Bi returning to metallic *Bi* through LiBi as an intermediate state. Further delithiation gave rise to a broad peak with some noise between 1.73 – 2.01 V, which should correspond to the transformation of Li_2Te to *Te*. Herein, the CV scan profile exhibit all the oxidation and reduction peaks in between 0.2V – 2.5V potential window, which could, therefore, be used to perform all the electrochemical measurements under this potential window.

5.4 C-rate optimization for Bi_2X_3 anodes

In order to optimize the C-rate for all Bi_2X_3 anode, the discharge/charge measurements were performed at 1, 0.5, 0.2 and 0.1 C, and the first discharging/charging profiles for Bi_2S_3 composite anodes are shown in **Figure 5.5 (a-d)**. It was observed that there is much noise during the discharging and charging process for the C-rates of 1, 0.5, and 0.2 C, which does not seem right for the cell operation. Moreover, the cell got opened during the measurements (as shown in the inset of **Figure 5.5 a)** for all the above rates due to unknown reason. The discharging/charging curve at 0.1 C rate was observed quite smooth without opening of the cell. This behavior was obtained for all Bi_2X_3 anodes, although only Bi_2S_3 discharge-charge curves at different C-rate are shown here. Thus, 0.1 C rate was adopted for all the further experiments of electrochemical discharging/charging cycles.

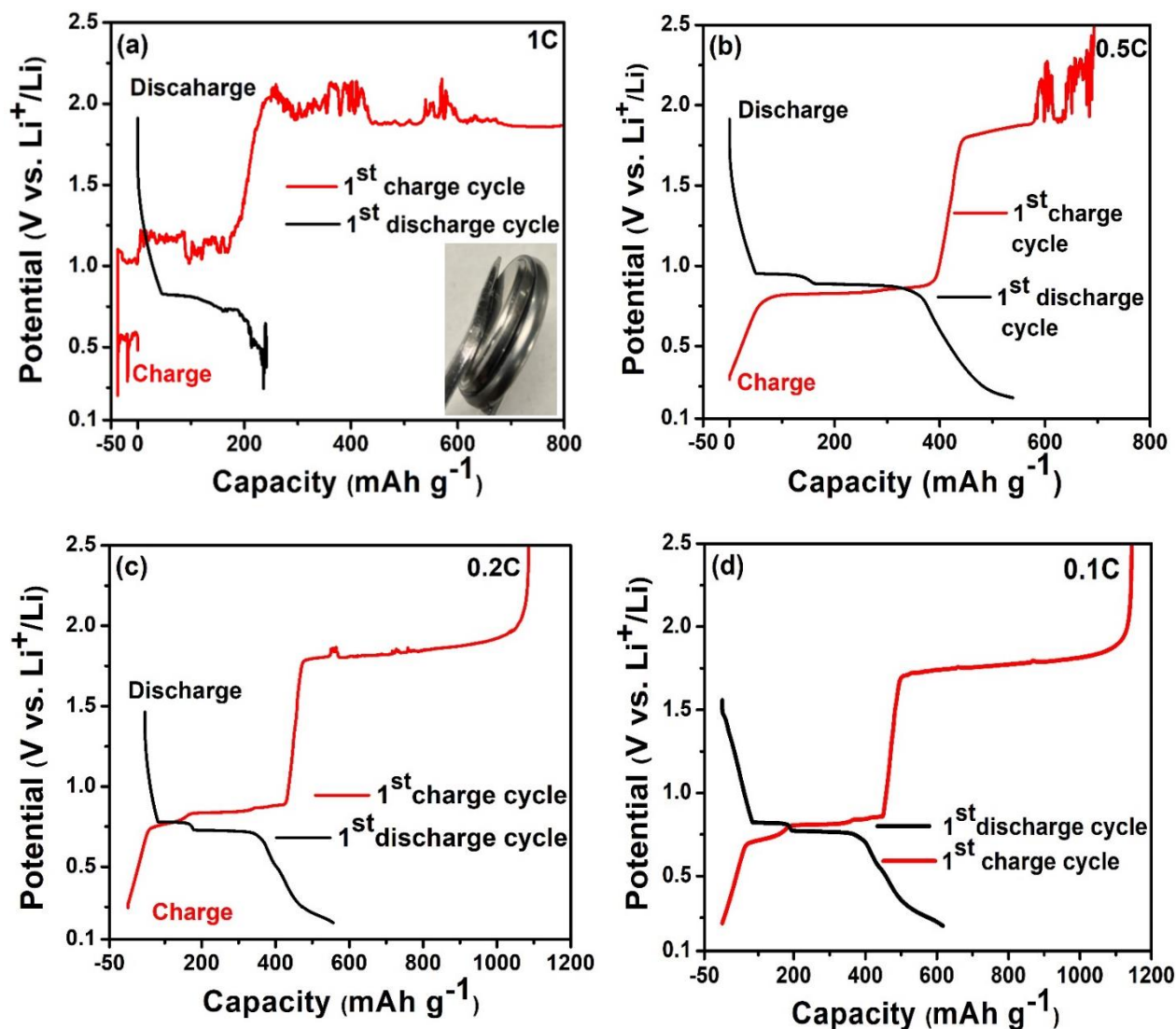


Figure 5.5: First electrochemical galvanostatic charging-discharging profile for bulk $\text{Bi}_2\text{S}_3\text{-LiBH}_4\text{-AB}$ composite electrode at several current rate (a) 1C, (b) 0.5C, (c) 0.2C, & (d) 0.1C.

5.5 Galvanostatic discharge/charge

To observe the electrochemical performance of above anode composite materials, galvanostatic discharge and charge characterizations were performed on the assembled coin cell at 125°C within the potential window 0.2-2.5V with the rate of 0.1C. **Figure 5.6 (a)** exhibits the first galvanostatic discharge-charge profile of bulk $\text{Bi}_2\text{S}_3\text{-LiBH}_4\text{-AB}$ composite anode material, and the obtained

discharge capacity of the prepared anode recorded as 617 mAhg^{-1} (volumetric capacity: 4183 mAhcm^{-3}), which is very close to the theoretical capacity (625 mAhg^{-1})[155].

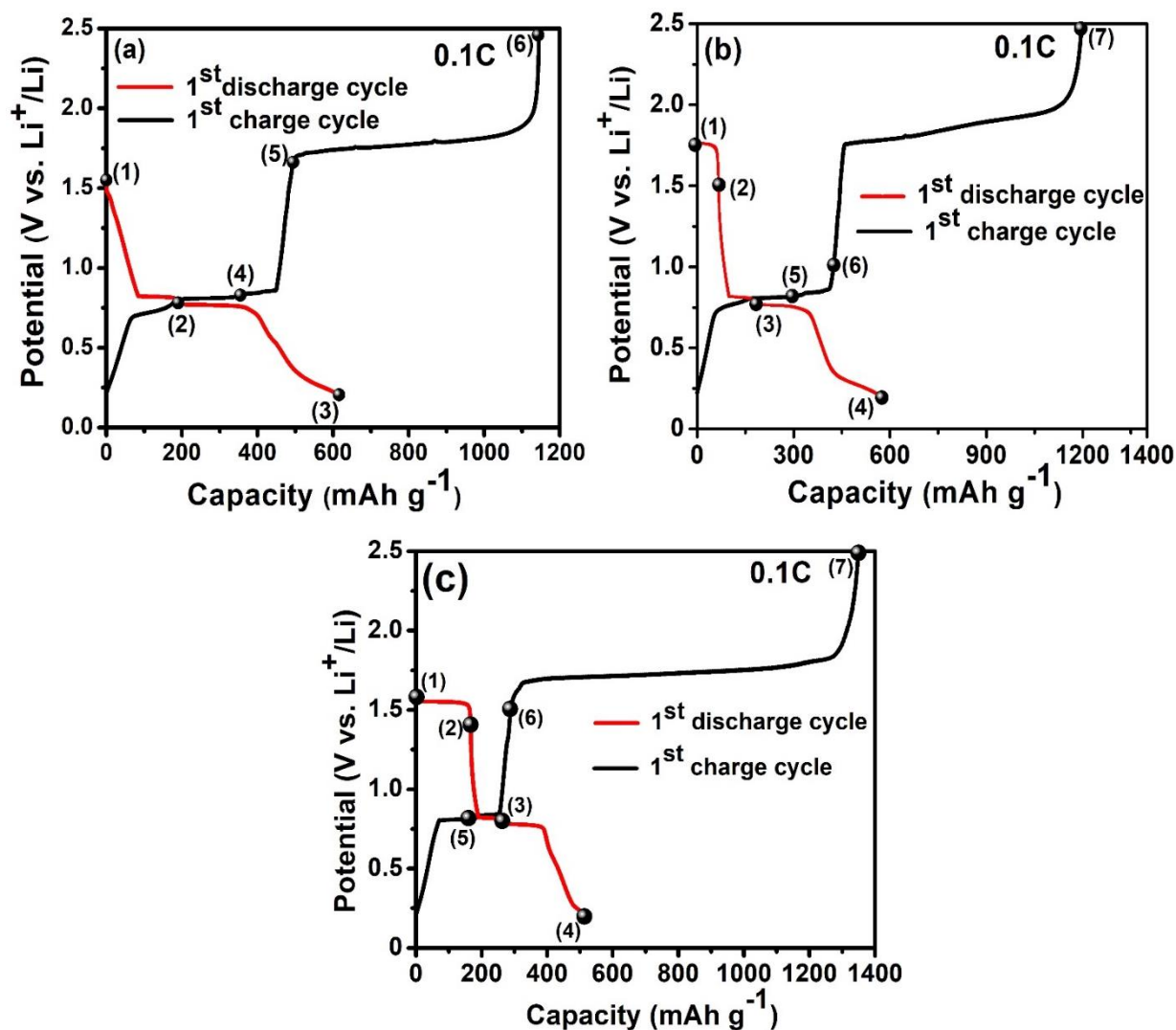


Figure 5.6: The initial galvanostatic discharge-charge profile for (a) $\text{Bi}_2\text{S}_3\text{-LiBH}_4\text{-AB}$ (b) $\text{Bi}_2\text{Se}_3\text{-LiBH}_4\text{-AB}$ (c) $\text{Bi}_2\text{Te}_3\text{-LiBH}_4\text{-AB}$ composite negative electrode in the voltage range of 0.2-2.5V at 0.1C current rate, where (1), (2), (3), (4), (5), (6) & (7) represents the different potential points during discharge-charge measurement.

However, the first charge capacity is found to be 1145 mAhg⁻¹, which is much larger than the discharge capacity. **Figure 5.6 (b)** shows the first discharge-charge profile of Bi₂Se₃-LiBH₄-AB composite electrode at optimized C-rate and potential window [156]. The prepared anode showed a discharge capacity of about 621 mAhg⁻¹ whereas the first charge capacity was 1346 mAhg⁻¹. The obtained discharge capacity was slightly higher than the theoretical capacity (491 mAhg⁻¹) of Bi₂Se₃, which must be due to the carbon contribution / some other side reaction. On the other hand, the charge capacity was found to be much higher than the discharge capacity. **Figure 5.6 (c)** shows the first discharge-charge profile for the cell containing the bulk Bi₂Te₃-LiBH₄-AB composite as negative electrode between the potential window 0.2 - 2.5 V vs. Li⁺/Li 0.1C. The first discharge capacity was observed as 515 mAhg⁻¹, which is again higher than the theoretical capacity of 401 mAhg⁻¹. The slightly higher capacity can be originated from the side reaction / the contribution from carbon lithiation. The first charging capacity was found more substantial than the discharging capacity, *i.e.*, 1349 mAhg⁻¹, similar to the other two anode composite materials [157].

As per the findings, the obtained charge capacity was very high than the theoretical values and discharge capacities for all the anode materials. The higher charging capacity can be attributed to some unknown/thermochemical reaction, which is occurred simultaneously with the electrochemical reaction.

5.6 Mechanism of lithiation/delithiation of Bi₂X₃ anode in all-solid-state Li-ion battery

To understand the mechanism behind the obtained high charge capacity and plateaus, the ex-situ XRD was performed at the selected potentials as indicated by numbers in **Figure 5.6**. The XRD pattern of the prepared composite anode material with as purchased bulk Bi₂S₃, AB, and LiBH₄ are shown in **Figure 5.7**. As shown in **Figure 5.1 (b)**, the spectra for as milled composite could be indexed by Bi and Li₂S phases in addition to the starting material, *i.e.*, Bi₂S₃ & LiBH₄, which must be due to a mechanochemical reaction during the milling. Since a mechanochemical reaction between Bi₂S₃ and LiBH₄ was observed during the milling, the XRD experiment was also performed after 1 hr heating (time for which the cell was kept before all the experiments in order to stabilize the temperature) at 125°C in oil bath before starting the discharging process, which is indicated by point 1 at 1.56V in **Figure 5.7 (a)**. The obtained XRD pattern (point 1) gives the

information about the reduction reaction of Bi_2S_3 to *Bi* and Li_2S (**Figure 5.7 a**) ultimately. Thus the starting material Bi_2S_3 was transformed entirely to *Bi* and Li_2S via mechanochemical and thermochemical reaction during the milling and 1hr heating process respectively. This was in line with the non-existence of expected 1st discharge plateau at around 1.6V, as shown in **Figure 5.6 (a)**. The second plateau has appeared at 0.79V which corresponded to the alloying reaction of *Bi* with *Li* to form LiBi as suggested by XRD profile at point 2. Further discharge down to 0.2V (point 3) proceed through further lithiation of *Bi* and LiBi to form Li_3Bi (plateau at 0.75V), which was confirmed from the XRD pattern of the discharging point 3. In the reverse scan, *i.e.*, during charging, these two plateaus are observed again, which correspond to lithium extraction from Li_3Bi to form LiBi and then to form *Bi* at 0.82V, which was evident from XRD at point 4 and point 5 respectively. Although the significant phases at point 5 are *Bi* and Li_2S , some peaks corresponding to LiBi are also visible, which probably due to the unreacted remaining part. The XRD experiment at point 6 was performed after charging the coin cell up to 2.5V, which also showed the existence of *Bi* and Li_2S rather than the starting material, *i.e.* Bi_2S_3 . This finding strengthens our above speculation of thermochemical reaction between LiBH_4 and freshly produced sulfur from Li_2S . Besides, the peaks corresponding to LiBH_4 were also visible in all the patterns as it was presented as a solid electrolyte in addition to anode composite material.

In case of Bi_2Se_3 electrode, the first plateau was observed at 1.75V that corresponded to the reduction reaction of Bi_2Se_3 to *Bi* and Li_2Se , as confirmed from the XRD pattern at point 2 (**Figure 5.7 b**). However, the plateau width was smaller than the calculated lithiation of *Se* to form Li_2Se ; thus XRD experiment was performed immediately before starting the discharging process, *i.e.*, after placing the coin cell in an oil bath at 125°C for 1 hr, which is indicated by point 1 in **Figure 5.7 (b)**. The XRD profile suggested the existence of Li_2Se and *Bi* in addition to unreacted Bi_2Se_3 , which suggested a thermochemical reaction between Bi_2Se_3 and LiBH_4 , thus transforming Bi_2Se_3 to Li_2Se and *Bi* partially. The next two plateaus were observed very close to each other, *i.e.*, at 0.82V and 0.77V corresponding to the alloying reaction of *Bi* with *Li* to form LiBi and finally Li_3Bi phases respectively as confirmed from the XRD pattern at point 3 and 4 of discharging profile. These three plateaus were also observed in the reverse scan or at the time of charging, and the reverse pattern of the formation of the compounds through delithiation was found to occur.

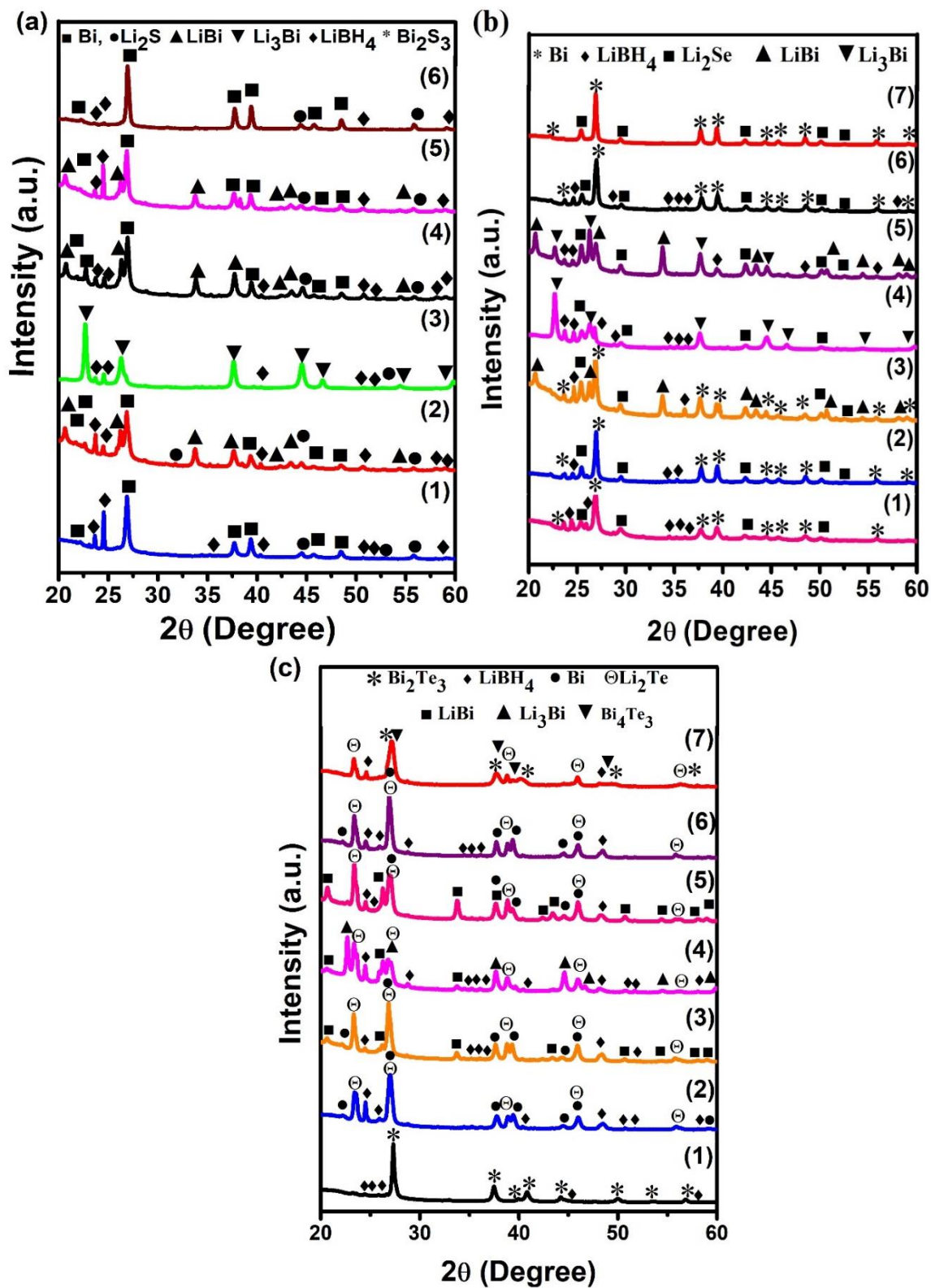
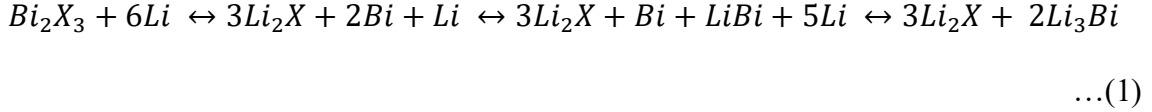


Figure 5.7: Ex-situ XRD patterns of $\text{Bi}_2\text{X}_3\text{-LiBH}_4\text{-AB}$ composite electrode on marked points in Figure 5.6.

The XRD pattern at point 5, *i.e.*, after first charging plateau at 0.80V suggested the formation of LiBi in addition to Li₂Se and Li₃Bi phases, although the peaks corresponding to Li₃Bi was reduced in comparison to point 4, which suggested the delithiation of Li₃Bi. The next plateau appeared immediately after and very close to the first plateau, *i.e.*, at 0.85V suggesting the delithiation of LiBi to form *Bi* as confirmed from the XRD pattern at point 6. On further charging to 2.5 V a long plateau (similar to Bi₂S₃) is appeared in between 1.7 – 2.0 V and the XRD experiment at point 7 suggested the existence of *Bi* and Li₂Se phases. The existence of Li₂Se even after charging up to 2.5 V indicated a possibility of thermochemical reaction between the LiBH₄ and freshly formed *Se* as a result of delithiation during the charging process. The freshly generated *Se* reacted with LiBH₄ and formed Li₂Se followed by delithiation of Li₂Se again. This process continued until the full consumption of LiBH₄. It caused a large capacity than the theoretical capacity during the charging process. Similar to Bi₂S₃, the peaks corresponding to LiBH₄ were also visible in all the XRD patterns.

Similar to Bi₂S₃ and Bi₂Se₃, the ex-situ XRD measurements (**Figure 5.7 c**) of the prepared bulk Bi₂Te₃-LiBH₄-AB composite anode material were performed at selected potentials, as indicated in the galvanostatic discharging/charging profile (**Figure 5.7 c**). It is noteworthy here that no thermochemical reaction was observed between LiBH₄ and Bi₂Te₃, unlike the case for Bi₂S₃ and Bi₂Se₃, which suggest less reactivity of Bi₂Te₃ with LiBH₄ in comparison to the other two materials. The XRD profile (**Figure 5.7 c**) at point 2 suggested the existence of two phases from the active material, *i.e.*, *Bi* and Li₂Te in addition to LiBH₄. It also suggested the first reaction to take place corresponding to the first plateau at 1.54 V, where the *Li*-ion moves from the positive electrode (cathode) to negative electrode (anode) and react with *Te* first to form Li₂Te, while *Bi* was unreacted with *Li*-ions at this potential. Since LiBH₄ was used as an electrolyte as well as in anode composite material with a sufficient amount (30%), so the peaks corresponding to the LiBH₄ phase were present at all stages. The next plateaus were observed at 0.82 – 0.75 V, thus the XRD was performed after discharging the cell up to 0.8V (point 3) and 0.2V (point 4) in which *Li*-ions reacted with *Bi* atoms also and formed LiBi followed by Li₃Bi. During the charging of the cell, the Li₃Bi phase disappeared first, and the LiBi phase started to reappear in the XRD pattern (point 5). Further charging up to 1.5 V extracts *Li* more and the XRD profile at point 6 showed the existence of *Bi* and Li₂Te phases. At the fully charged state (point 7, 2.5V), the peaks corresponding to Bi₂Te₃ phase were observed with the traces of Bi₄Te₃ & Li₂Te.

Based on the above ex-situ XRD results, the reaction involved in the first discharge and charge verified the excellent reversibility of the alloying reaction between Bi_2X_3 and Li -ion. The established electrochemical reversible reaction may be shown as equation (1):



On the other hand, the charging of the coin cell up to 2.5V showed a 2-3 fold high capacity than the theoretical value. Notably, the second plateau at ~ 1.7-1.8 V was quite long in comparison to the theoretical value of $\text{Li}_2\text{X} \leftrightarrow \text{X}$ reaction (as shown in **Figure 5.6**). It can be proposed based on the simultaneous thermochemical reaction between LiBH_4 (in composite anode material) and X ($\text{X} = \text{S}, \text{Se}, \& \text{Te}$) (generated electrochemically during the de-lithiation process). This thermochemical reaction generates Li_2X followed by electrochemical $\text{Li}_2\text{X} \leftrightarrow \text{X}$ conversion until the full consumption of LiBH_4 in the composite. The capacity is well matched with the amount of LiBH_4 in the composite as per the following reactions:



The presence of this thermochemical reaction was also confirmed by the thermogravimetric analysis and reported elsewhere [158], [159].

5.7 Cyclic stability measurements under 0.2-2.5V

After successfully establishing the reversible electrochemical reaction, the cyclability of the prepared composite anode materials was investigated under 0.2-2.5V at 0.1C-rate. The cyclic discharge-charge profiles are shown in **Figure 5.8**. Whereas the initial discharge-charge profile depicted the excellent electrochemical performance of the electrode (**Figure 5.6**), the cyclability for all the composite anodes was found very poor. All the cells stopped working after 8-13 cycles, which must be due to the above mentioned thermochemical reaction and the consumption of LiBH_4 , thus affecting the Li -ion mobility through the anode material in successive cycles, which was visible during the discharging charging cycling (**Figure 5.8**). The thermochemical reaction

caused the electrolyte decomposition, which developed the cracks on the surface of anode material and thus lost the connectivity after around 10 cycles; consequently, the cell stopped working.

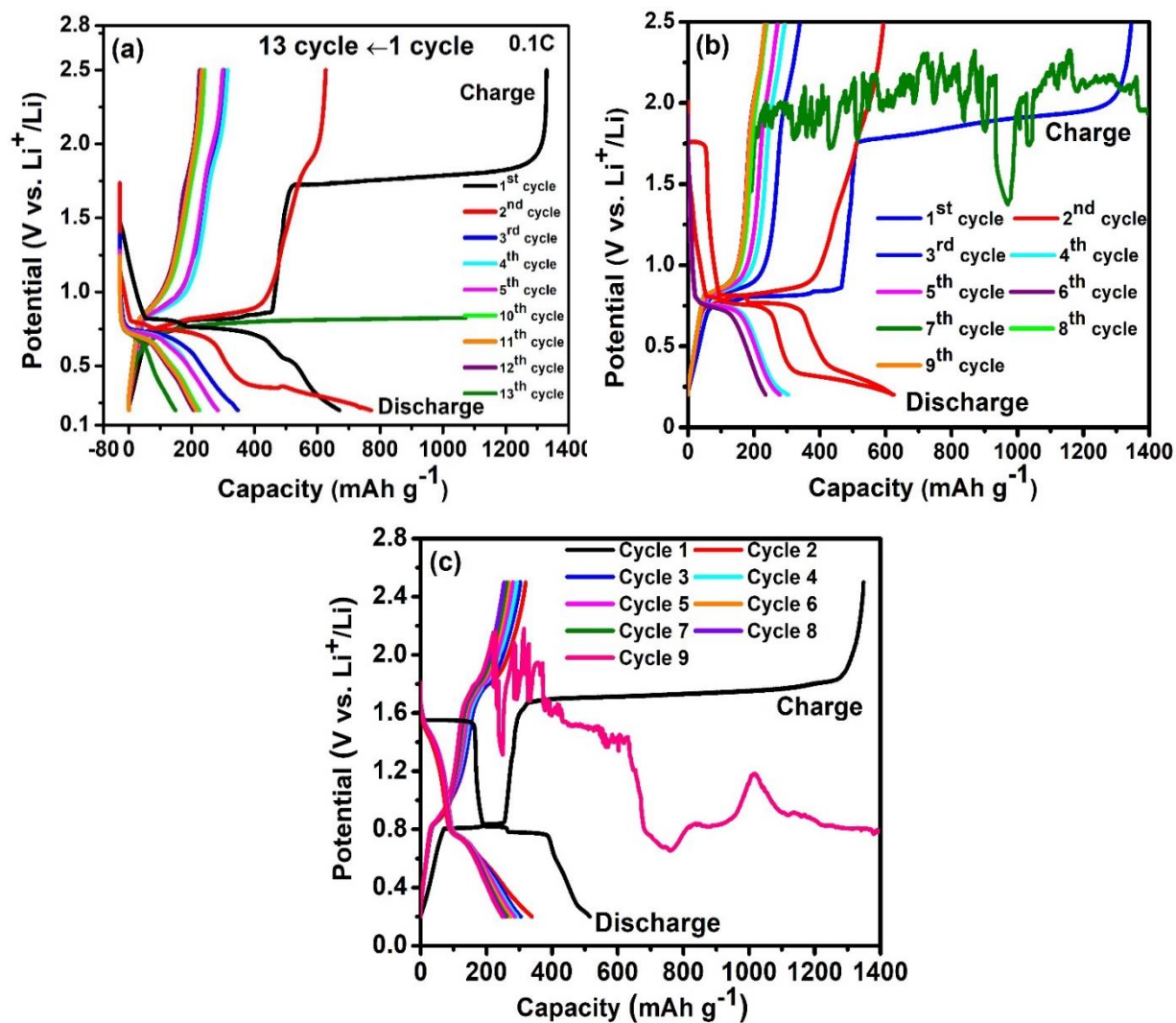


Figure 5.8: Cyclic performance of the bulk (a) Bi₂S₃-LiBH₄-AB (b) Bi₂Se₃-LiBH₄-AB (c) Bi₂Te₃-LiBH₄-AB composite electrode in the voltage range of 0.2-2.5V at temperature 125°C with 0.1C rate.

5.8 Morphological investigations of Bi₂X₃ anode

In order to confirm the side reaction/mechanism mentioned above, morphological observation of the anode surface before and after cycling was done by SEM studies. The SEM images and

elemental mapping confirmed the above proposed thermochemical reaction and exhibited clear evidence of the cracks and crumbling on the electrode surface after cycling (Figure 5.9, Figure 5.10 & Figure 5.11). The elemental mapping suggested that *Bi*, *X*, *Li*, and *B* were present homogeneously throughout the electrode before cycling.

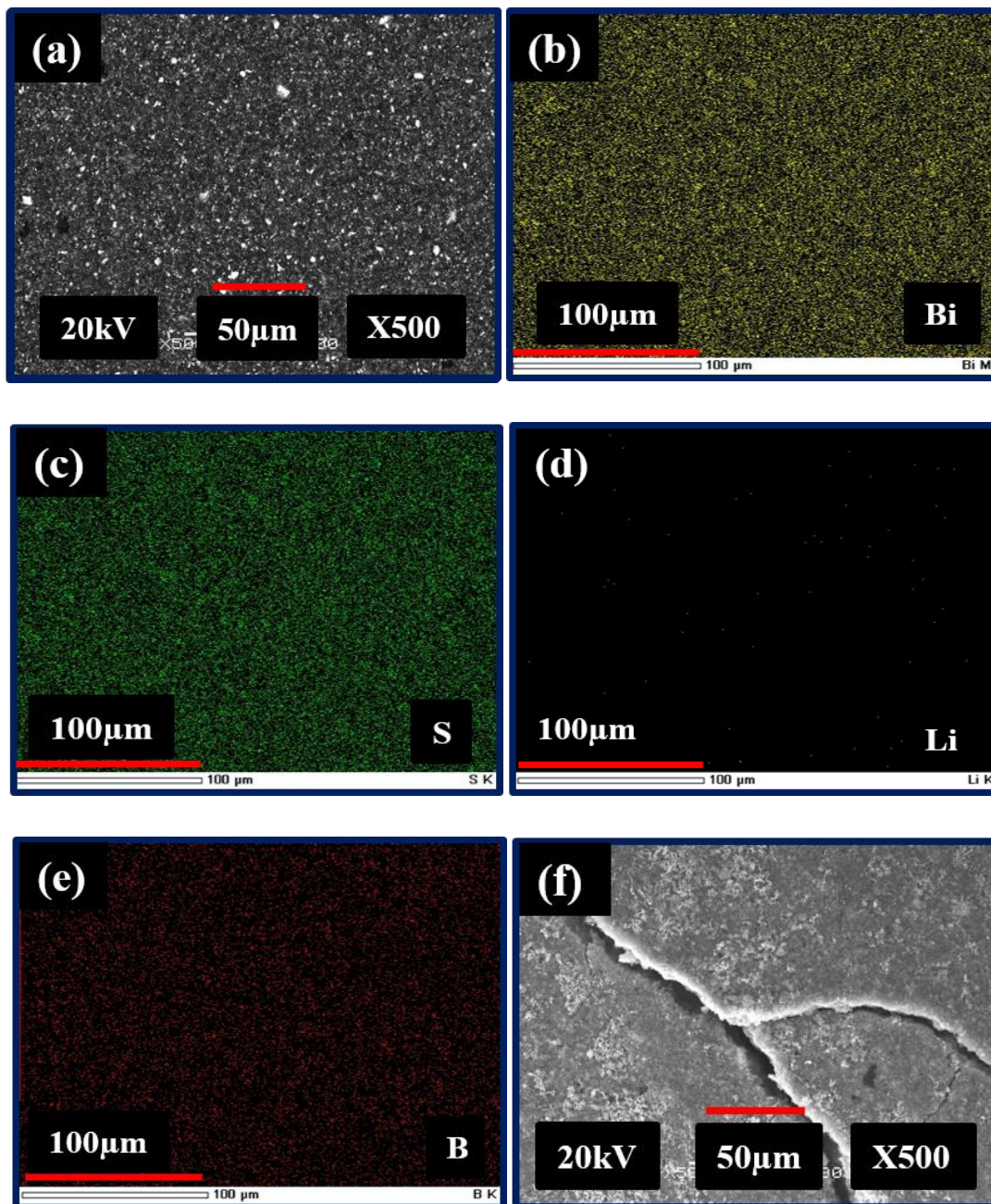


Figure 5.9: (a-e) SEM images and corresponding elemental mapping of Bi_2S_3 in the composite electrode surface before cycling, and (f) after 13 cycles in the voltage range 0.2-2.5V.

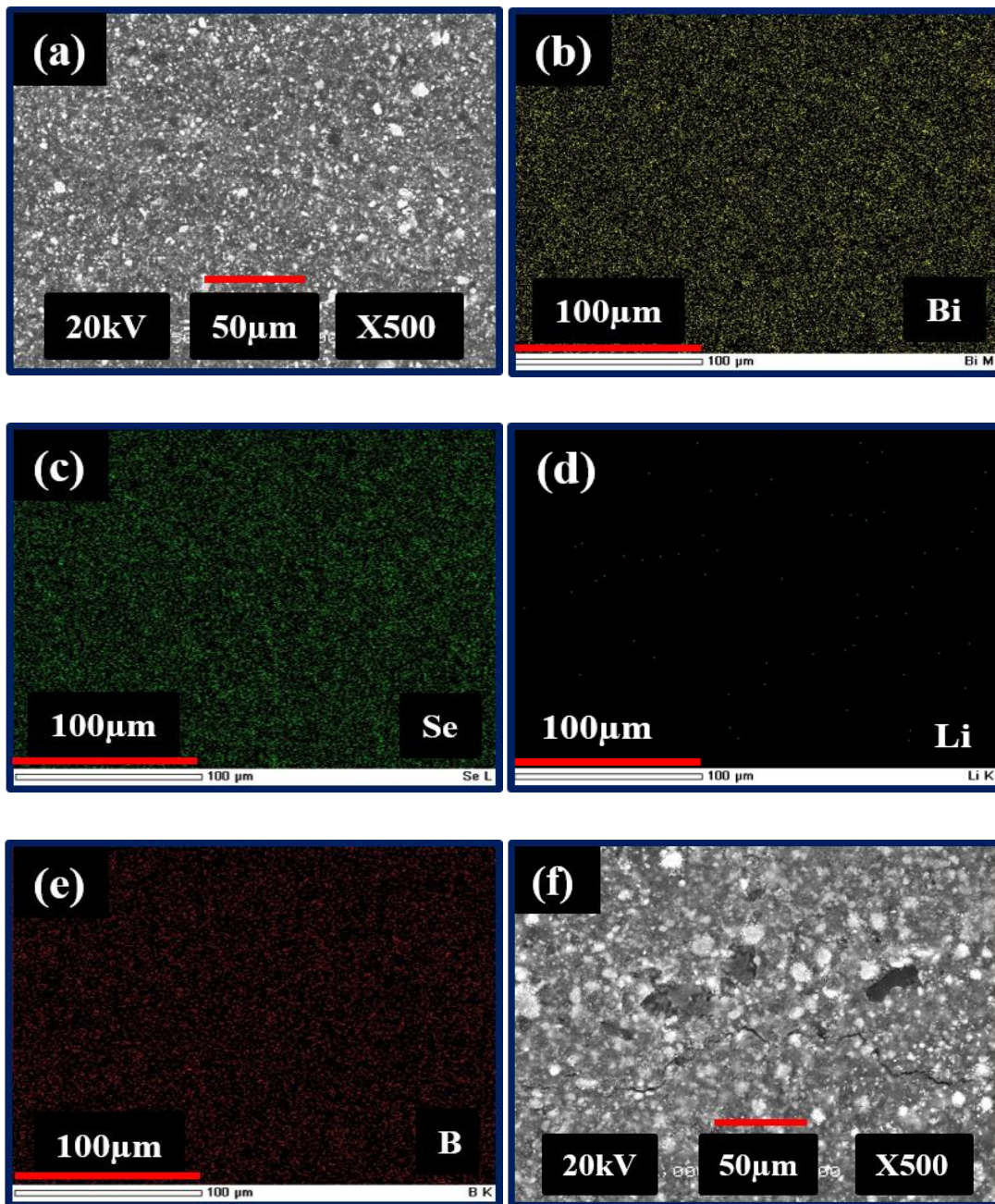


Figure 5.10: (a-e) SEM images and corresponding elemental mapping of Bi_2Se_3 in the composite electrode surface before cycling, and (f) after 9 cycles in the voltage range 0.2-2.5V.

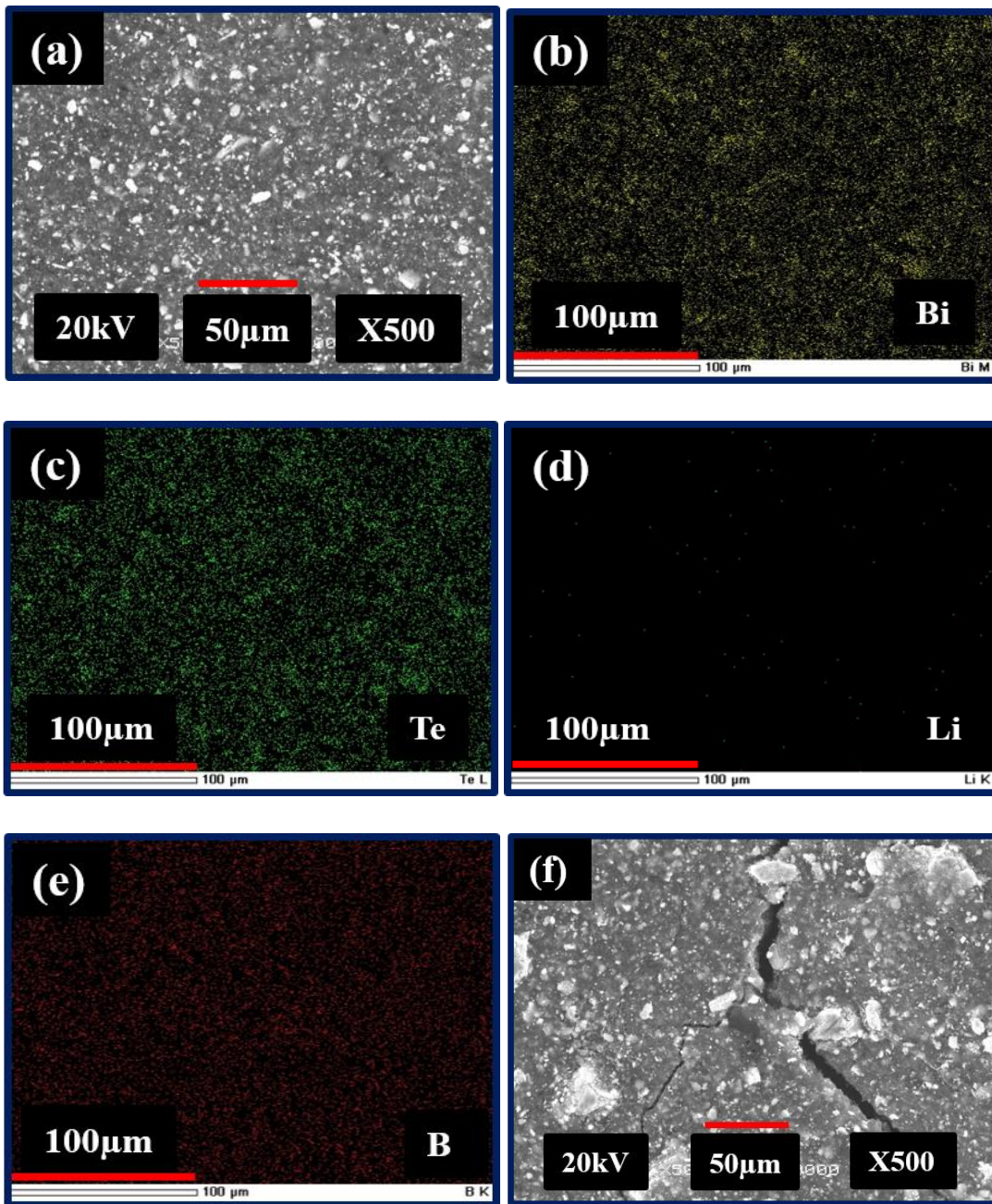


Figure 5.11: (a-e) SEM images and corresponding elemental mapping of Bi_2Te_3 in the composite electrode surface before cycling, and (f) after 9 cycles in the voltage range 0.2-2.5V.

5.9 Cyclic stability measurements under 0.2-1.5V

To avoid the side reaction mentioned above (occurred in between 1.7-2V) and crack formation on the electrode surface, the galvanostatic discharge/charge cycling test up to 50 cycles for Bi_2X_3 electrodes were performed in 0.2 to 1.5 V range at 0.1C, and the profile is shown in **Figure 5.12**. From **Figure 5.12 (a)** it could be observed that the first discharge and charge capacity was found to be 662 mAhg^{-1} and 524 mAhg^{-1} , respectively. The initial capacity dropped to 586 mAhg^{-1} and 485 mAhg^{-1} in the subsequent second cycle, which further reduced down to 311 mAhg^{-1} and 225 mAhg^{-1} respectively with the 47% capacity decay of bulk $\text{Bi}_2\text{S}_3\text{-LiBH}_4\text{-AB}$ composite electrode in comparison to the first cycle. This limited potential window eliminated the formation of the cracks on the electrode surface (as confirmed by **Figure 5.13**); however, it limited the total achievable capacity as well.

In the case of $\text{Bi}_2\text{Se}_3\text{-LiBH}_4\text{-AB}$ to avoid the thermochemical reaction, the galvanostatic discharge/charge cycling was performed between 0.2V – 1.5V at 0.1C, and the results are illustrated in **Figure 5.12 (b)**. It was observed that the electrode delivered a high discharge capacity of about 621 mAhg^{-1} in the first cycle, which was faded down to 397 mAhg^{-1} in the second cycle due to the limited potential window and did not allow the $\text{Se} \leftrightarrow \text{Li}_2\text{Se}$ conversion. The capacity finally reached 306 mAhg^{-1} after 50 cycles, which suggested only 23% capacity decay in 50 cycles. It was evidenced that the electrode material performed well between 0.2V – 1.5V without any side reactions and showed a highly stable *Li* storage capacity than the other reports (already discussed in **chapter 2**) even though the $\text{Se} \leftrightarrow \text{Li}_2\text{Se}$ conversion reaction was not allowed to proceed. The limited potential window also suppressed the formation of the crack on the surface of anode material during discharging/charging cycles (**Figure 5.14**) in contrast to what we observed in the case of 0.2-2.5V potential window.

Figure 5.12 (c) clearly shows that the bulk $\text{Bi}_2\text{Te}_3\text{-LiBH}_4\text{-AB}$ composite electrode delivered a high discharge capacity of 533 mAhg^{-1} in the first cycle, which was faded down to 257 mAhg^{-1} in the second cycle due to the limited potential window and then showed a quite stable discharging/charging capacity with cycling and reached to a capacity of 219 mAhg^{-1} in 50th cycle, which suggested only 15% capacity decay in 50 cycles. It was also observed that the plateau voltage for discharge and charge processes remained nearly the same during cycling, indicating that the composite electrode material worked well between 0.2 and 1.5 V without any side

reactions. Although the capacity was faded down to a lower value in the 2nd cycle due to a limited potential window, however, it was much better than the previous report (as discussed in detail in **Chapter 2**). This stability was also confirmed from the micrographs (**Figure 5.15**) of the composite electrode pellet after 50 cycles of discharging / charging, where no cracks were observed in contrast to the previous cell as described above.

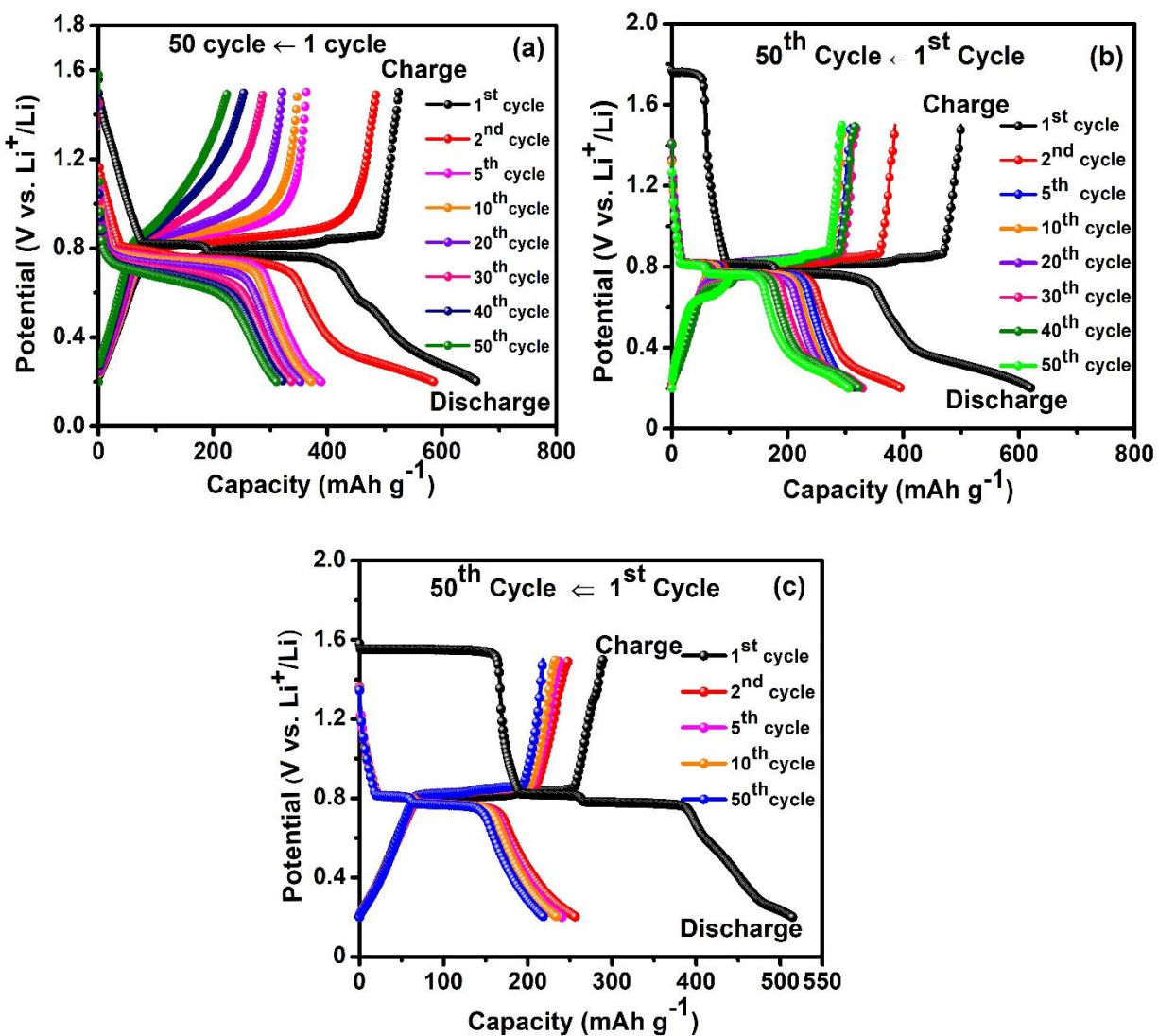


Figure 5.12: Cyclic discharging/charging profile of the bulk (a) $\text{Bi}_2\text{S}_3\text{-LiBH}_4\text{-AB}$ (b) $\text{Bi}_2\text{Se}_3\text{-LiBH}_4\text{-AB}$ and (c) $\text{Bi}_2\text{Te}_3\text{-LiBH}_4\text{-AB}$ composite electrode in the voltage range of 0.2-1.5V at 125°C with 0.1C rate.

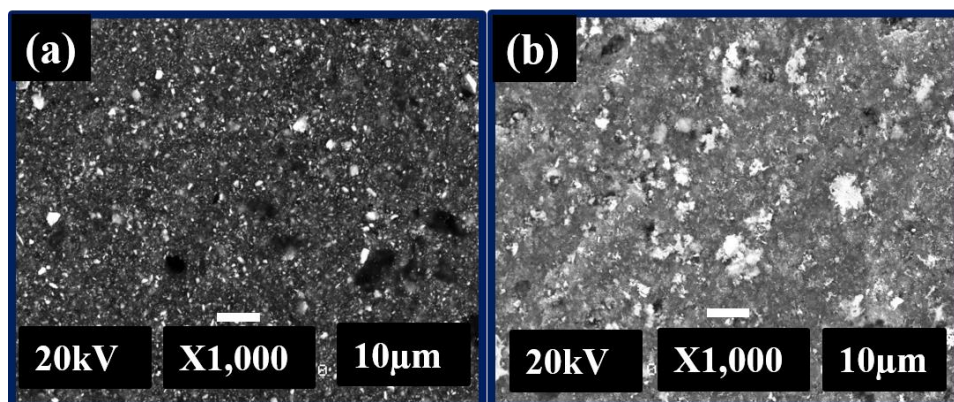


Figure 5.13: FE-SEM images of bulk $\text{Bi}_2\text{S}_3\text{-LiBH}_4\text{-AB}$ composite anode after galvanostatic discharging-charging in the voltage range of 0.2-1.5V (a) 0 cycles and (b) 50 cycles.

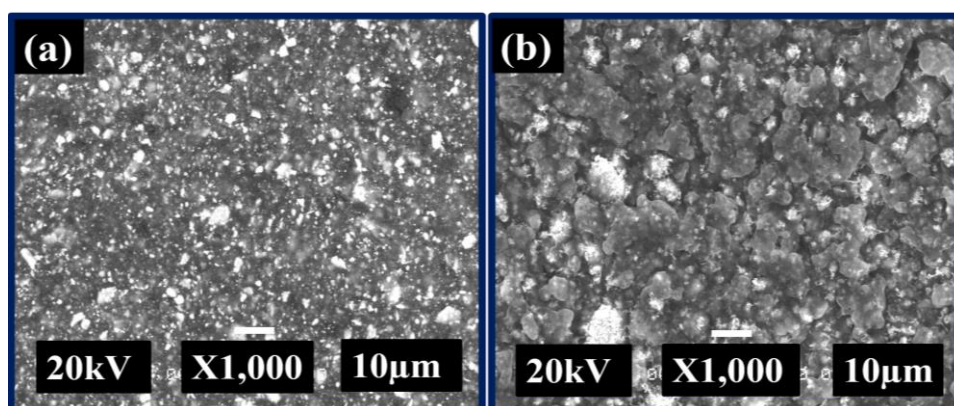


Figure 5.14: FE-SEM images of bulk $\text{Bi}_2\text{Se}_3\text{-LiBH}_4\text{-AB}$ composite anode after galvanostatic discharging-charging in the voltage range of 0.2-1.5V (a) 0 cycles and (b) 50 cycles.

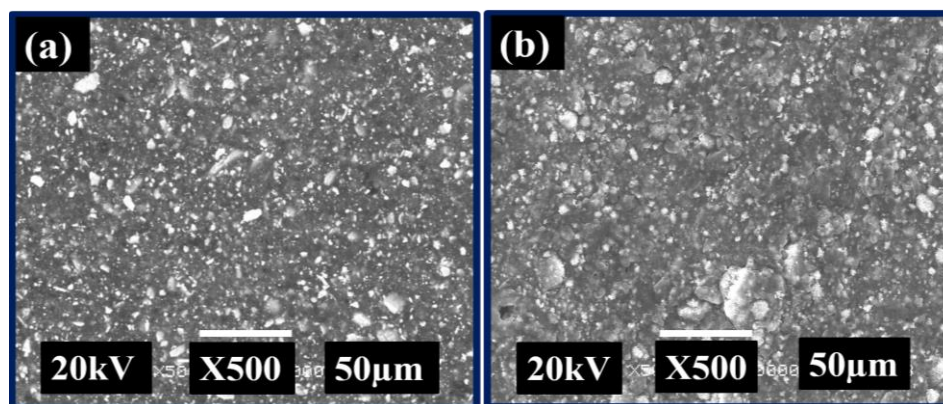


Figure 5.15: FE-SEM images of bulk $\text{Bi}_2\text{Te}_3\text{-LiBH}_4\text{-AB}$ composite anode after galvanostatic discharging-charging in the voltage range of 0.2-1.5V (a) 0 cycles and (b) 50 cycles.

5.10 Summary

In summary, the present chapter clarified the reversible electrochemical mechanism between Bi_2X_3 and Li -ion. An extremely small polarization is particularly remarkable to make these materials as a promising candidate for the negative electrode in all-solid-state LIBs. These anode materials exhibited outstanding volumetric capacity and gravimetric capacity. Although the performance of these anode materials was very high with solid electrolyte LiBH_4 , it reacted with Bi_2X_3 during the second step of charging ($\sim 1.7 \text{ V} - 2 \text{ V}$) which resulted in the loss of physical contact between active material and electrolyte; thus capacity gradually dropped. All the cyclic measurements up to 50 cycles were performed in between $0.2 - 1.5 \text{ V}$ to avoid this side reaction, and excellent stability with high capacity was obtained. However, it reduced the overall achievable capacity. It would be interesting to explore these anode materials as the nanostructured electrodes; as it might enhance the cyclic stability with high coulombic efficiency. Also, these anode materials can be used with other solid electrolytes, *e.g.*, $\text{Li}_2\text{S-P}_2\text{S}_5$ in order to allow the cycling for the full range, *i.e.*, $0.2 - 2.5 \text{ V}$.

Chapter Six

Nanostructured Bi₂X₃ Anode with Highly Stable Electrochemical Performance

6.1 Introduction

The research community is currently appealing in generous efforts to attain effective energy storage strategies which are the keys for the use of alternative energy and thus for the replacement of fossil fuels and traditional energy storage [28]. In this concern, rechargeable LIBs play a vital role due to their gravimetric and volumetric energy density, low self-discharge property, high power density, and long cycle life [160], [161]. Moreover, LIBs have been proven to be the most effective energy storage strategy for a wide range of portable devices such as laptops, cellular phones, and digital electronics [23], [114], [162]. On the other hand, the employment of LIBs in electric vehicles requires 2-5 times more energy density than the present LIBs. Anode materials play an essential role, which can provide high reversible capacity, good ionic and electrical conductivity, high rate of lithium diffusion into active material, low cost along with good cycling life and free from safety concerns. Currently, graphite is the most commonly used anode material due to its excellent features, like good cycle life, low cost, and low working potential vs. lithium. However, it faces a low reversible capacity of 372 mAhg⁻¹ due to the allowance of one *Li*-ion with six carbon atoms, with a resulting stoichiometry of LiC₆ [163], [164]. Also, the diffusion rate of *Li* into carbon materials is between 10⁻¹² and 10⁻⁶ cm²s⁻¹, resulting in batteries with low power density. Hence there is a need to replace graphite anode to the materials with higher capacity, high power density, and energy.

In particular, alloying type anode materials with a larger capacity than that of the commercial graphite anode have been investigated actively as possible alternative anode materials [165]–[167]. Belonging to this family, bismuth (*Bi*) has attracted considerable attention as an anode material with 386 mAhg⁻¹ gravimetric capacity, which is comparable to the graphite anode (372 mAhg⁻¹) and also has the sizeable volumetric capacity as 3800 mAhcm⁻³. Its 4-fold high

volumetric capacity than carbon makes it exciting material since the volumetric capacity is as important as the gravimetric capacity for the practical applications which need less space but large capacities. In order to further enhance the specific and volumetric capacity, *Bi*-based materials such as Bi_2X_3 ($\text{X} = \text{S}, \text{Se}, \text{O}, \& \text{Te}$) have been explored, as the element X also can alloy with *Li* [39], [168], [169]. As per the reversible electrochemical reaction, it is quite clear now that Bi_2X_3 at first transforms to Li_2X through the reaction



followed by the alloying process



Both the alloying reactions contribute to a substantial volumetric augment, which causes particle pulverization and cracks, resulting in a continuous inevitable capacity decay. Thus, improvement of cyclability of the chalcogenide materials remains a crucial challenge to be addressed for the optimization of their *Li*-storage performance. In this sense, promising results and a bright perception is accessible by nanostructured electrodes. The expected advantages of using nanotechnology in LIBs serves a high surface to volume ratio, therefore the growth of the existence of active sites for *Li*-storage. Moreover, the high surface area would provide a high contact area with the electrolyte, hence leading to high *Li*-ion flux across the electrolyte/electrode interface, resulting in a considerable increment of the specific capacity. Nanostructured anodes also improve the *Li*-diffusion due to the reduction of its path length, therefore provide batteries with enhanced power capability.

In this chapter, hydrothermally synthesized Bi_2X_3 nanostructures were used as anode material in all-solid-state LIBs. A comparative electrochemical study between the commercial bulk Bi_2X_3 and Bi_2X_3 nanostructures was examined [155]–[157]. The improvement in the cyclability of all-solid-state LIBs using nanostructured Bi_2X_3 is also discussed herein.

6.2 Morphological studies of the prepared Bi_2X_3 nanostructures

It is commonly hypothesized that the electrochemical performance of a nanostructured electrode depends on their shape, size, and morphology [170], thus it is essential to assess the morphology

of the prepared sample which was done here using FESEM and TEM measurements and the images are illustrated in **Figure 6.1**, **Figure 6.2**, & **Figure 6.3**. FESEM and TEM of the prepared Bi_2S_3 samples are illustrated in **Figure 6.1**. The FESEM image (**Figure 6.1 a**) depicted the flower-like morphology and exhibited that each shoot in this pattern was formed along with a well-arranged assembly of many nanorods [155]. The nanorods have a variation in the diameter and length in the range of 10 – 150 nm and 150 – 400 nm respectively. All the prepared samples were further characterized by TEM, as shown in **Figure 6.1 (b)**. The TEM images of the prepared nanostructures confirmed the above FESEM observations and designated that the flower-like morphology was successfully obtained. **Figure 6.1 (c)** depicts the HRTEM observations of the prepared nanostructure, in which the lattice fringes show interplanar spacing of 0.37 nm, allocated to the (101) plane of Bi_2S_3 . SAED pattern of nanoflowers indicated the polycrystalline nature, as shown in **Figure 6.1 (d)**.

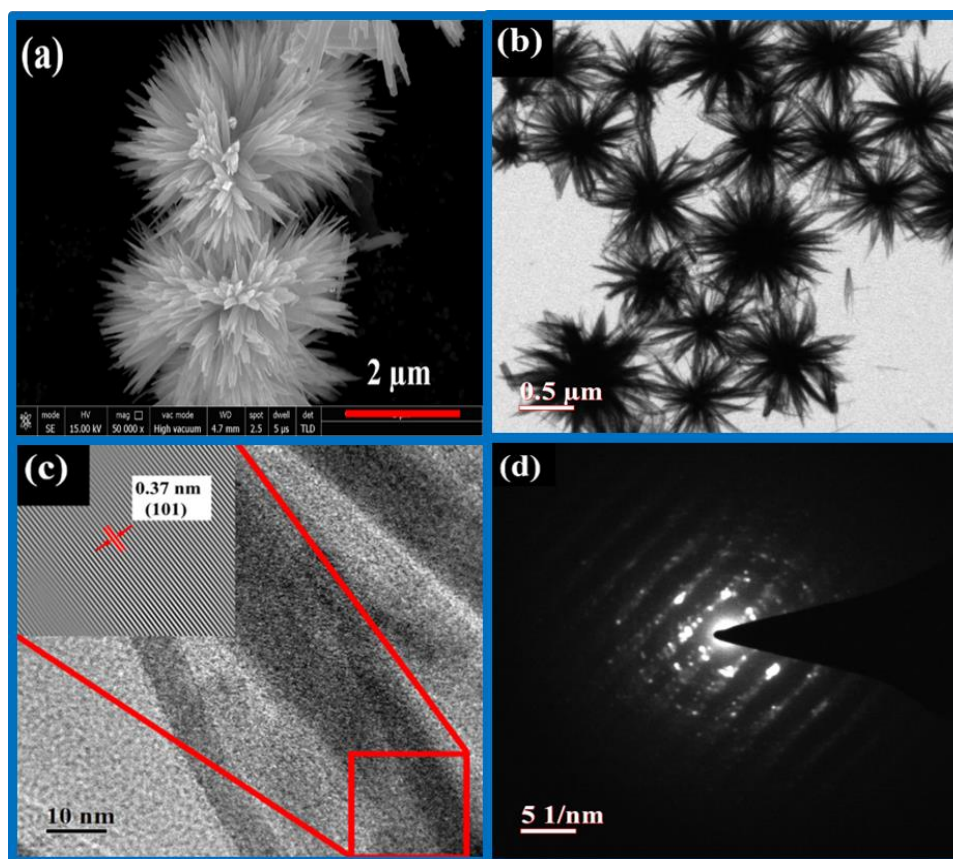


Figure 6.1: (a & b) FE-SEM & TEM images of Bi_2S_3 nanoflowers (c & d) HRTEM & SAED images of nanoflowers.

The SEM and TEM experiments were performed on the prepared Bi_2Se_3 samples, and the obtained morphological information about the product is illustrated in **Figure 6.2**. The low magnification SEM images [**Figure 6.2(a) & (b)**] illustrated that the prepared sample had mixed morphology of nanoparticles and nanosheets [156]. The particle size was calculated to be in the range of 20 nm-150 nm, whereas the thickness of the nanosheets was found to be in the range of 5 – 30 nm. **Figure 6.2 (c)** shows the TEM image of mixed nanosheets and nanoparticles while **Figure 6.2 (d)** exhibits HRTEM image of the prepared product which suggested the interplanar spacing of 0.378 nm, assigned to the (101) plane of Bi_2Se_3 . SAED pattern of a single nanosheet indicated the single crystalline nature [**Figure 6.2 (e)**], whereas, the SAED pattern of nanoparticle showed polycrystalline nature.

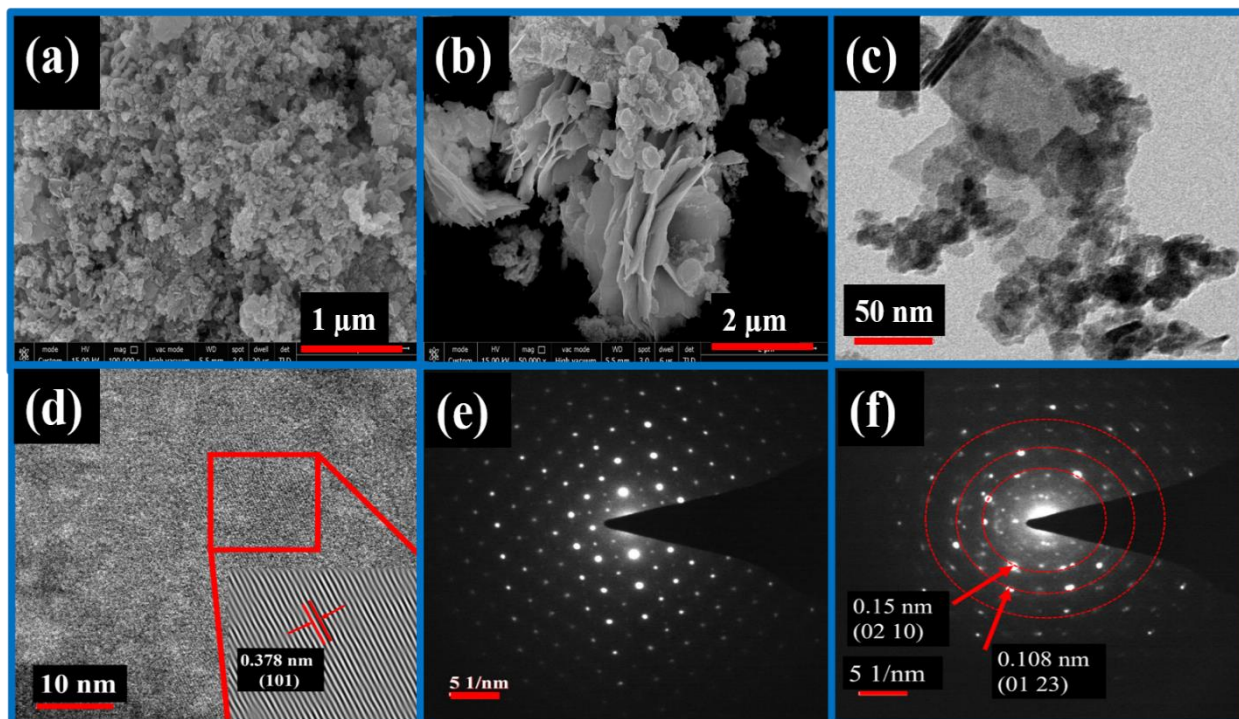


Figure 6.2: (a) & (b) FE-SEM images of as prepared Bi_2Se_3 nanostructures; (c-f) TEM, HRTEM & SAED pattern of nanostructures.

SEM and TEM experiments were performed to evaluate the morphology of the prepared Bi_2Te_3 product. TEM and SEM images of Bi_2Te_3 nanorods are depicted in **Figure 6.3**. The SEM image is

shown in **Figure 6.3 a & b** revealed that Bi_2Te_3 nanorods were successfully synthesized via a hydrothermal process, forming a wide-open structure[157]. TEM observations further investigated more detailed information on their microstructures. TEM experiments revealed the variation in length and diameter of nanorods in the range of 50-400 nm and 20-70 nm, respectively. **Figure 6.3 (d)** presents the high-resolution TEM image of the nanorods with clear lattice fringes, demonstrating its high crystalline nature. The fringe spacing was calculated to be 0.34 nm, which matched well with the d-spacing of the (104) plane of rhombohedral Bi_2Te_3 .

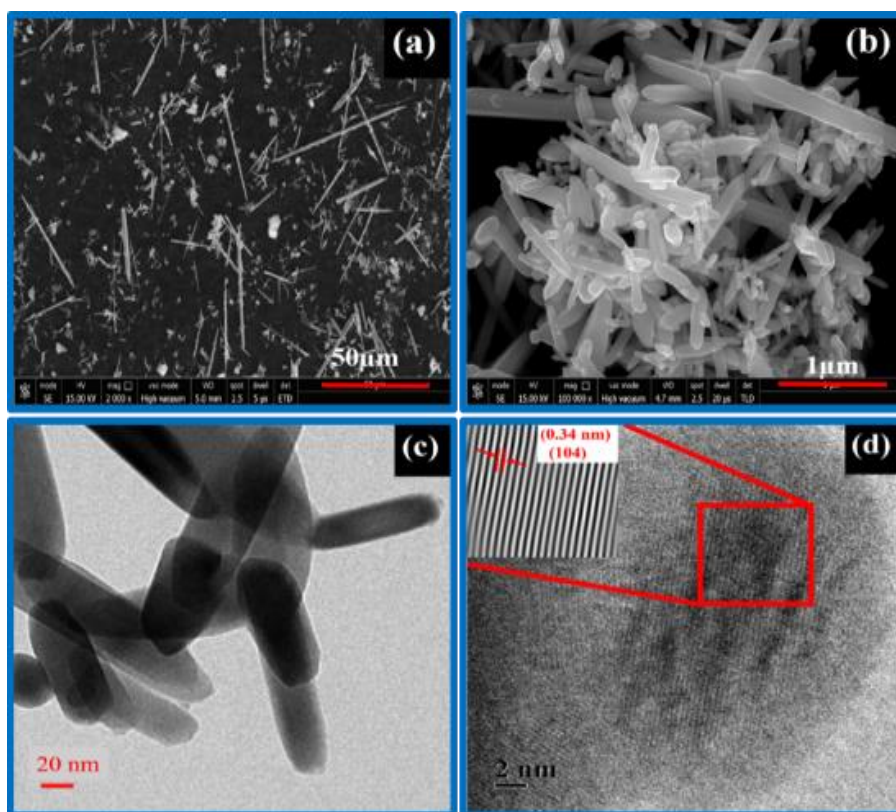


Figure 6.3: (a & b) FE-SEM images of Bi_2Te_3 nanorods and (c & d) TEM, HRTEM images of nanorods.

6.3 Structural investigation of the prepared Bi_2X_3 nanostructures

Figure 6.4 (a) presents the XRD patterns of the synthesized nanostructured Bi_2S_3 samples. All the diffraction peaks could be indexed to an orthorhombic Bi_2S_3 phase (JCPDS card no. 00-006-0333) with Pbnm space group along with some Bi_2O_3 traces. The structural analysis of the obtained Bi_2S_3 pattern designated the lattice parameters $a = 11.15\text{\AA}$, $b = 11.30\text{\AA}$ and $c = 3.9810\text{\AA}$ agreeing well with the literature values. The XRD pattern of the prepared composite anode material with as prepared Bi_2S_3 nanoflowers, heat-treated AB, and heat-treated LiBH_4 is shown in **Figure 6.4 (b)**. It was observed that a partial mechanochemical reaction took place during the milling as evident from the presence of Bi and Li_2S peaks in addition to the starting material, *i.e.*, Bi_2S_3 & LiBH_4 .

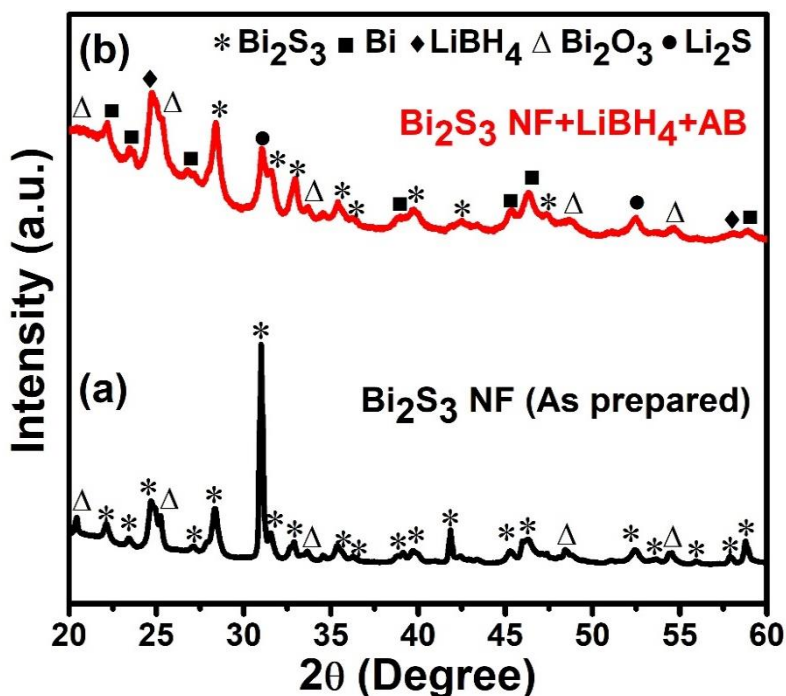


Figure 6.4: XRD pattern of (a) as-prepared Bi_2S_3 nanoflowers and (b) Bi_2S_3 nanoflowers- LiBH_4 -AB composite electrode.

The XRD pattern of as-prepared Bi_2Se_3 nanostructures is shown in **Figure 6.5 (a)**. All the obtained peaks could be indexed to a trigonal Bi_2Se_3 (JCPDS card no. 00-033-0214) with R-3m space group as well as trigonal Bi_3Se_4 (JCPDS card no. 00-029-0245) phases in addition to some

trace of Bi_2O_3 and unreacted Se . The lattice parameters a , b , & c for Bi_2Se_3 phase were calculated as 4.14 Å, 4.14 Å, and 28.63 Å, respectively. The lattice parameters for trigonal Bi_3Se_4 were obtained as, $a = b = 4.23$ Å and $c = 40.40$ Å. The XRD pattern of Bi_2Se_3 - LiBH_4 -AB composite electrode material (**Figure 6.5 b**) confirmed the existence of individual main phases of Bi_2Se_3 , Bi_3Se_4 , and LiBH_4 .

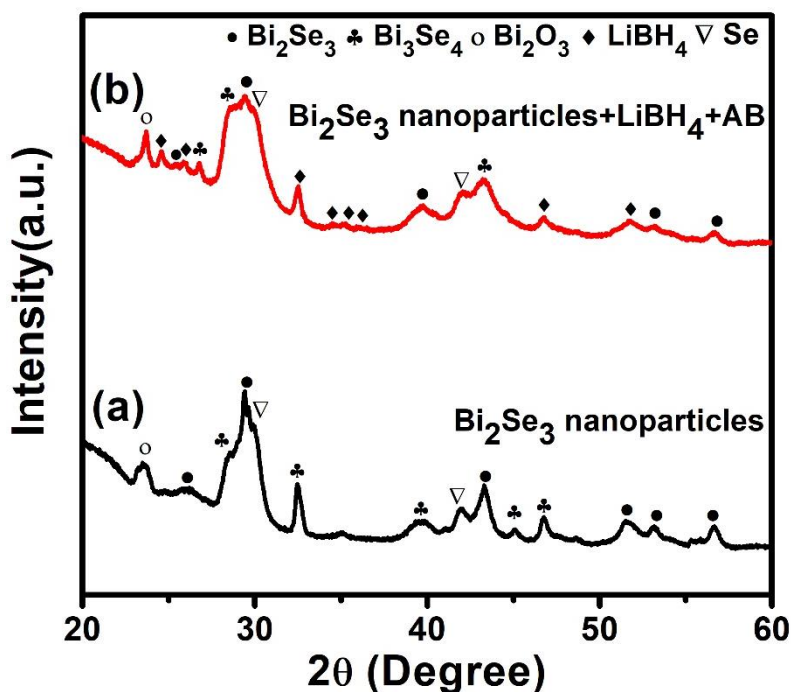


Figure 6.5: XRD pattern of (a) as prepared Bi_2Se_3 nanostructures (b) Bi_2Se_3 nanostructures- LiBH_4 -AB composite electrode.

The crystallographic structure of the synthesized Bi_2Te_3 nanorods was characterized by XRD. As shown in **Figure 6.6 (a)**, the broad peaks of the prepared sample indicated the nanocrystalline nature of the materials and due to the quantum confinement effect. The observed planes correspond to the Bi_2Te_3 polycrystals (JCPDS: 00-015-0863) with rhombohedral ($R\bar{3}m$) symmetry, and the average crystallite size was calculated to be 16 nm using Debye Scherrer formula. Unit cell refined values of nanorods, a , b and c are found to be 4.38 Å, 4.38 Å, and 30.48 Å, respectively [171]. The existence of LiBH_4 and Bi_2Te_3 peaks in the XRD profile (**Figure 6.6 b**) of composite material ($\text{Bi}_2\text{Te}_3/\text{LiBH}_4/\text{AB}$) confirmed that no chemical reaction was occurred in between the components during milling.

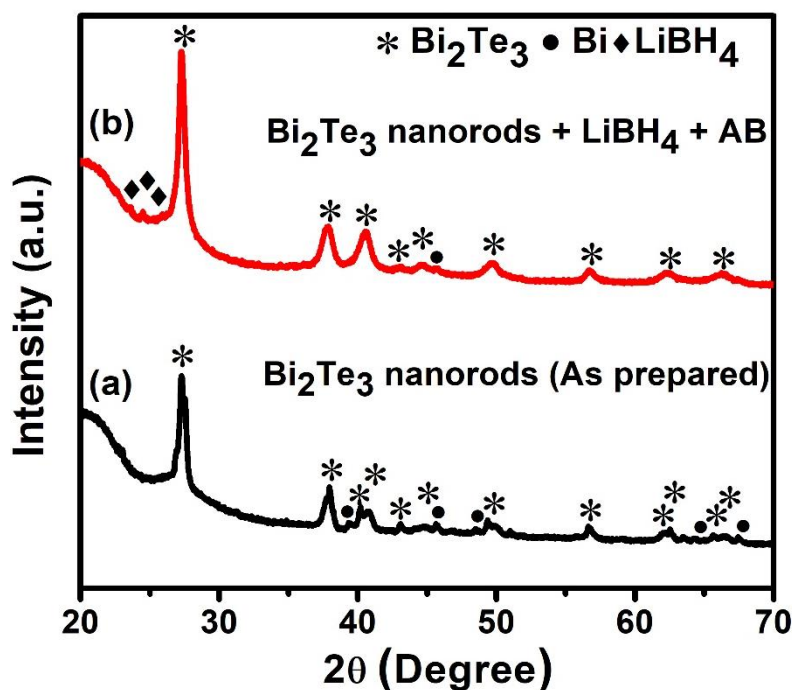


Figure 6.6: XRD pattern of (a) as-prepared Bi_2Te_3 nanorods and (b) Bi_2Te_3 nanorods- LiBH_4 - AB composite electrode.

6.4 Cyclic voltammetry

Figure 6.7 shows the CV curves for the Bi_2X_3 nanostructures in between 0.2 – 2.5 V at a scan rate of 0.1 mVs^{-1} . **Figure 6.7 (a)** exhibits the CV scan profile of Bi_2S_3 nanoflowers. The open-circuit voltage (OCV) of the cell was 1.55 V. In the first cathodic scan of the bulk sample, a weak peak at 1.45V could be ascribed to the Li_2S formation through the reaction of Li ions with the unreacted remaining Bi_2S_3 , while the peaks at 0.79 V and 0.72 V was due to the formation of LiBi followed by Li_3Bi phase. On the other hand, the reverse anodic scan process showed two peaks at 0.85 V and 0.88 V corresponding to the delithiation of Li_3Bi to LiBi and Bi respectively. Further delithiation gave rise to a broad peak in between 1.86 – 2.01 V, which corresponded to the transformation of Li_2S to S . The broad nature of the peak gave rise the possibility of simultaneous additional reaction along with the electrochemical reaction. The first cathodic peak at 1.45 V is weaker than the bulk sample (Chapter 5, **Figure 5.4**), which was quite apparent due to the kinetically fast thermochemical reaction between LiBH_4 and nano Bi_2S_3 , thus converting most of

the nano Bi_2S_3 to Li_2S during the heating process before the electrochemical discharging/charging. The other peaks were found quite similar to that of bulk Bi_2S_3 (as discussed in **Chapter 5**).

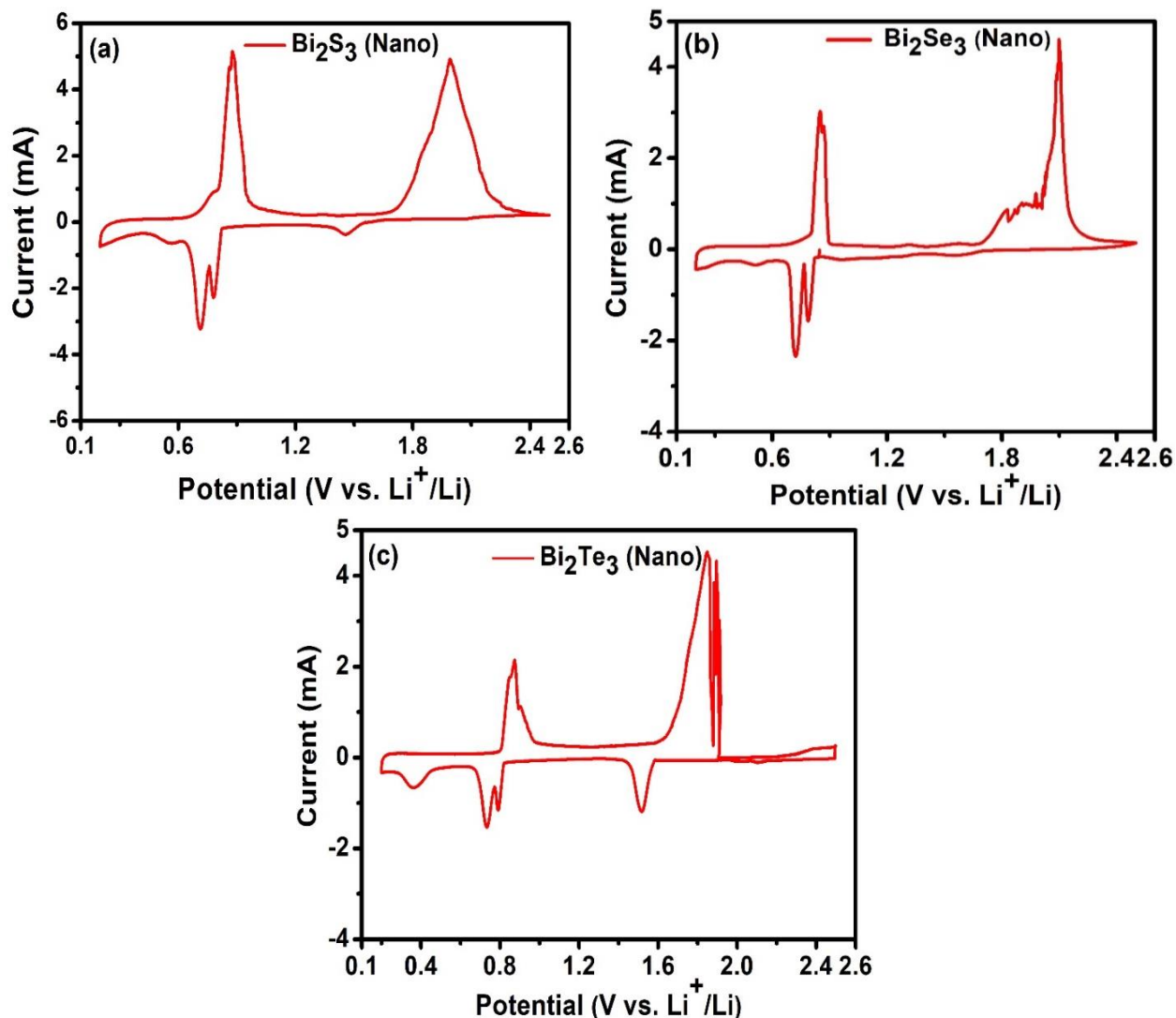


Figure 6.7: Cyclic Voltammograms of (a) Bi_2S_3 nanoflowers- LiBH_4 -AB composite electrode (b) Bi_2Se_3 nanostructures- LiBH_4 -AB composite electrode (c) Bi_2Te_3 nanorods- LiBH_4 -AB composite electrode scanned at 0.1mVs^{-1} .

Figure 6.7 (b) represents the CV profile of Bi_2Se_3 nanostructures. The initial OCV for nano Bi_2Se_3 was observed as 1.71 V after heating the coin cell at 125°C for 3 hours, and no peak corresponding

to Li_2Se formation was observed. This suggested the complete conversion of Se to Li_2Se as a result of a thermochemical reaction between Bi_2Se_3 and LiBH_4 during the heating. The other two peaks corresponding to $\text{Bi} \rightarrow \text{LiBi}$ and Li_3Bi conversion were visible at the same position as for bulk Bi_2Se_3 composite anode (two peaks at 0.79 and 0.72V corresponding to the lithiation of Bi to form LiBi and Li_3Bi successively). During the reverse scan, *i.e.*, charging process, two peaks appeared in the voltage range of 0.84 - 0.86 V corresponding to delithiation of Li_3Bi and LiBi . Significant noise was observed in the broad peak at 1.7-2.0 V, which must be due to the simultaneous electrochemical and thermochemical reaction, as discussed in **chapter 5**.

Figure 6.7 (c) depicts the CV scan profile of Bi_2Te_3 nanorods to optimize a suitable potential window for all electrochemical studies. The OCV voltage for Bi_2Te_3 nanorods was observed as 1.55V. At first, during the lithiation (Discharging) scan of $\text{Bi}_2\text{Te}_3/\text{LiBH}_4/\text{AB}$ electrode, the first cathodic peak located at 1.5 V could be ascribed to the Li_2Te formation, while the other two peaks corresponding to LiBi and Li_3Bi were located at the same position as for the bulk Bi_2Te_3 . Also, during the reverse scan, the same pattern has been followed by nanostructures as that by bulk sample (as explained in **Chapter 5**).

6.5 Cyclic stability measurements under 0.2-2.5V

The first galvanostatic discharge-charge curve of the nano $\text{Bi}_2\text{S}_3\text{-LiBH}_4$ composite anode material is illustrated in **Figure 6.8 a**, which was performed at 125°C temperature with the 0.1C rate. The prepared nanostructures recorded the first discharge and charge capacities as 685 mAhg^{-1} (corresponding volumetric capacity: 4644 mAhcm^{-3}) and 1330 mAhg^{-1} respectively, in the voltage window of 0.2-2.5V. The obtained first lithiation capacity was slightly higher than the theoretical capacity (625 mAhg^{-1}) of Bi_2S_3 ; it could be associated with the contribution of the carbon (AB), which was contained in the anode composite material in sufficient amount (30 wt %). On the other hand, the first charge capacity was found much higher than the discharge capacity, approximately 2-fold higher than the discharge capacity. This is quite similar to the bulk Bi_2S_3 anode, which indicated the existence of simultaneous thermochemical and electrochemical reactions during the delithiation process. The delithiation process at around 1.7V transformed Li_2S to S . However; this freshly generated sulfur might thermochemically be reacted with LiBH_4 (a component of anode

composite material), thus again formed Li_2S . This thermochemically generated Li_2S again took part in the electrochemical reaction and released Li -ion. This cyclic process continued until the full consumption of LiBH_4 . The calculated value of charge capacity (according to the actual amount of LiBH_4 and Bi_2S_3 in anode composite) as per above speculation agreed well with the obtained capacity during de-lithiation. The consumption of LiBH_4 due to this thermochemical reaction should affect the Li -ion mobility through the anode material in successive cycles, which was visible during the discharging charging cycling (**Figure 6.8 a**). The capacity was drastically reduced to around 200 mAh g^{-1} within 12 cycles, and finally, the cell stopped working in the 13th

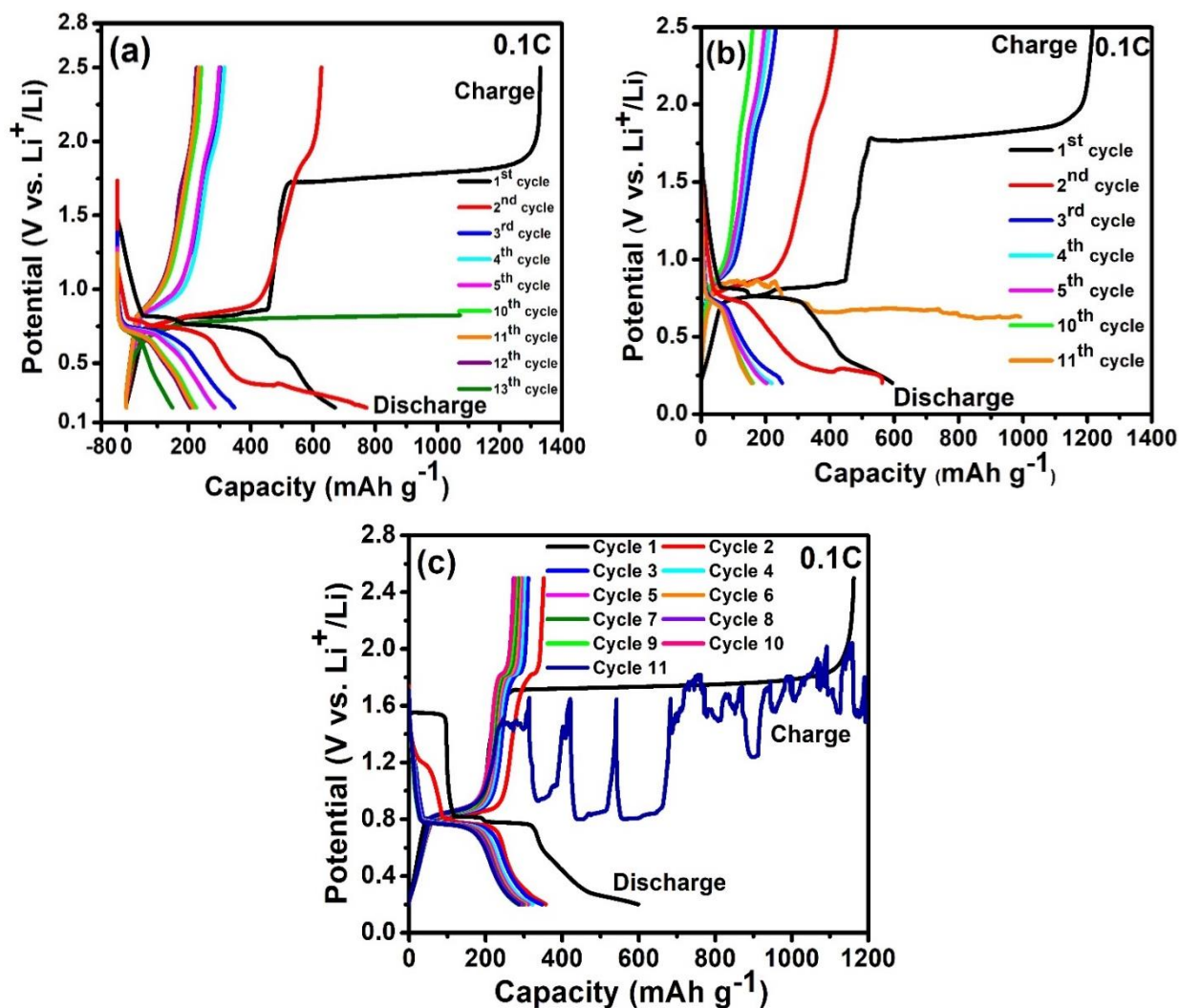


Figure 6.8: Cyclic performance of the nano (a) $\text{Bi}_2\text{S}_3\text{-LiBH}_4\text{-AB}$ (b) $\text{Bi}_2\text{Se}_3\text{-LiBH}_4\text{-AB}$ (c) $\text{Bi}_2\text{Te}_3\text{-LiBH}_4\text{-AB}$ composite electrode in the voltage range of 0.2-2.5V at temperature 125°C with 0.1C rate.

cycle. The above mechanism was also supported by the morphological observation of the anode surface after the cycles, where the cracks and crumbling are observed (**Figure 6.9**). These cracks also confirmed the above-proposed side reaction/thermochemical reaction.

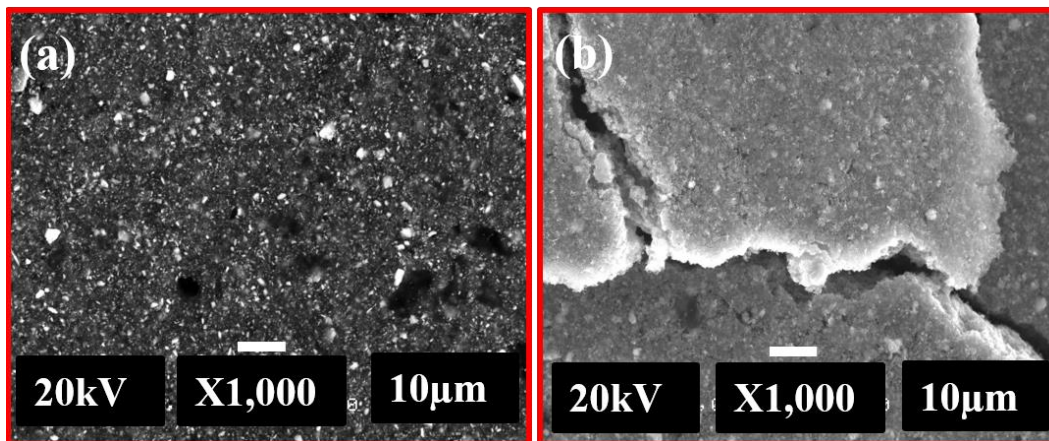


Figure 6.9: SEM images of nano $\text{Bi}_2\text{S}_3\text{-LiBH}_4$ composite anode after galvanostatic electrochemical discharging- charging in the voltage range of 0.2-2.5V (a) 0 cycles and (b) 13 cycles.

The electrochemical discharging/charging profile of nano- Bi_2Se_3 composite electrodes (**Figure 6.8 b**) was found to be quite similar to that for the bulk- Bi_2Se_3 composite electrode. However, the first small plateau at around 1.75V completely disappeared, which must be due to the complete conversion of Bi_2S_3 to Li_2Se and Bi due to the thermochemical reaction as described in **chapter 5**. Similar to the bulk Bi_2Se_3 composite electrode, the nano- Bi_2Se_3 electrode showed a similar cyclic behavior when performed in the potential window of 0.2-2.5V and cell was broken after 11 cycles due to the formation of cracks (**Figure 6.10**) caused by the side reaction.

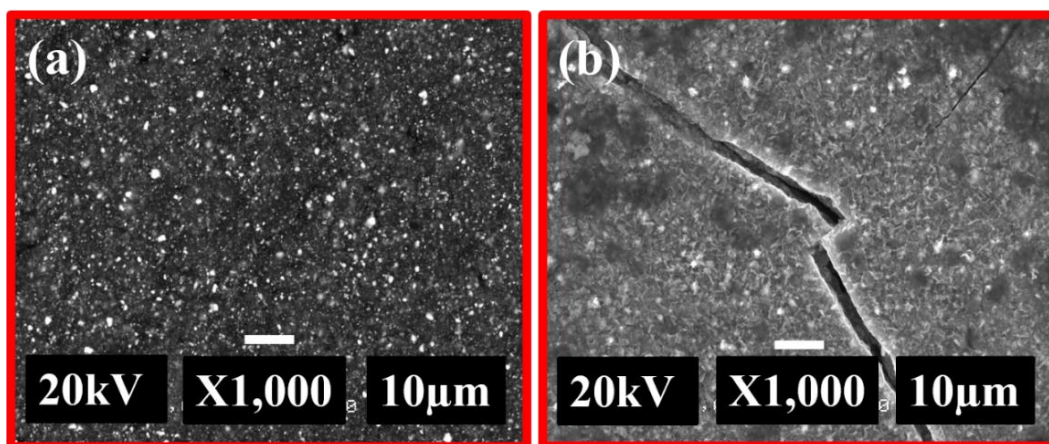


Figure 6.10: FE-SEM images of nano $\text{Bi}_2\text{Se}_3\text{-LiBH}_4$ composite anode (a) before and (b) after 10 cycles of galvanostatic electrochemical discharging-charging in the voltage range of 0.2-2.5V.

The cyclic behavior of Bi_2Te_3 nanorods was also found quite similar to Bi_2S_3 and Bi_2Se_3 nanostructures. After the 11th number of cycle, the cell was broken, and the capacity faded down rapidly (**Figure 6.8 c**). The crack formation on the electrode surface was also visible here (**Figure 6.11**).

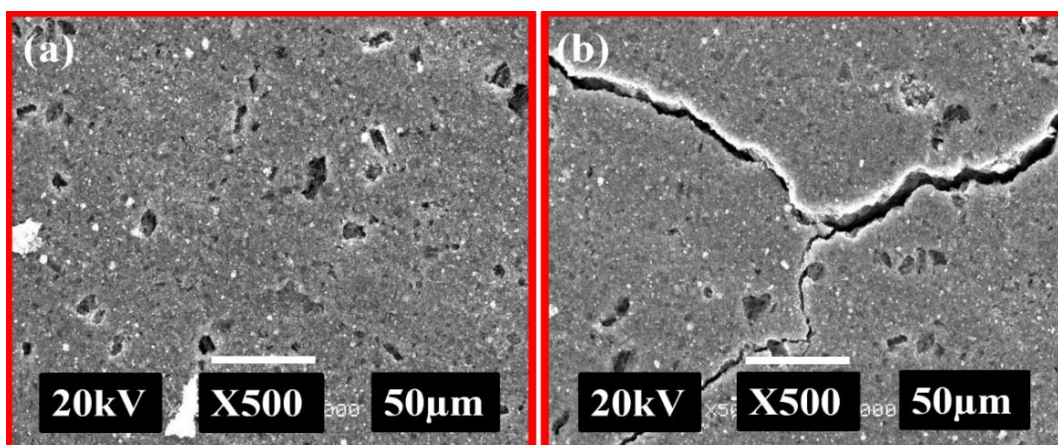


Figure 6.11: FE-SEM images of nano $\text{Bi}_2\text{Te}_3\text{-LiBH}_4$ composite anode after galvanostatic electrochemical discharging- charging in the voltage range of 0.2-2.5V (a) 0 cycles and (b) 10 cycles.

6.6 Cyclic stability measurements under 0.2-1.5V

Based on the galvanostatic discharge-charge and FESEM measurements on the prepared coin cell (by using bulk Bi_2X_3 as well as Bi_2X_3 nanostructures), it was clear that a thermochemical reaction occurred in between Bi_2X_3 and LiBH_4 at around 1.7V-2V. Therefore to avoid this side/thermochemical reaction, the galvanostatic discharge/charge cycling test was performed on nano Bi_2S_3 - LiBH_4 -AB composite electrode in a limited potential window 0.2-1.5V at 125°C temperature with a 0.1C rate as illustrated in **Figure 6.12**. The nano Bi_2S_3 - LiBH_4 -AB composite electrode material delivered the initial discharge and charge capacities of 685 mAhg^{-1} and 494 mAhg^{-1} , respectively, with 95.8% coulombic efficiency. The discharge and charge capacities dropped to 532 mAhg^{-1} and 502 mAhg^{-1} in the second cycle and then reached to 375 mAhg^{-1} (ca. 2543 mAhcm^{-2}) and 352 mAhg^{-1} in the 50th cycle. The obtained capacities were considerably better

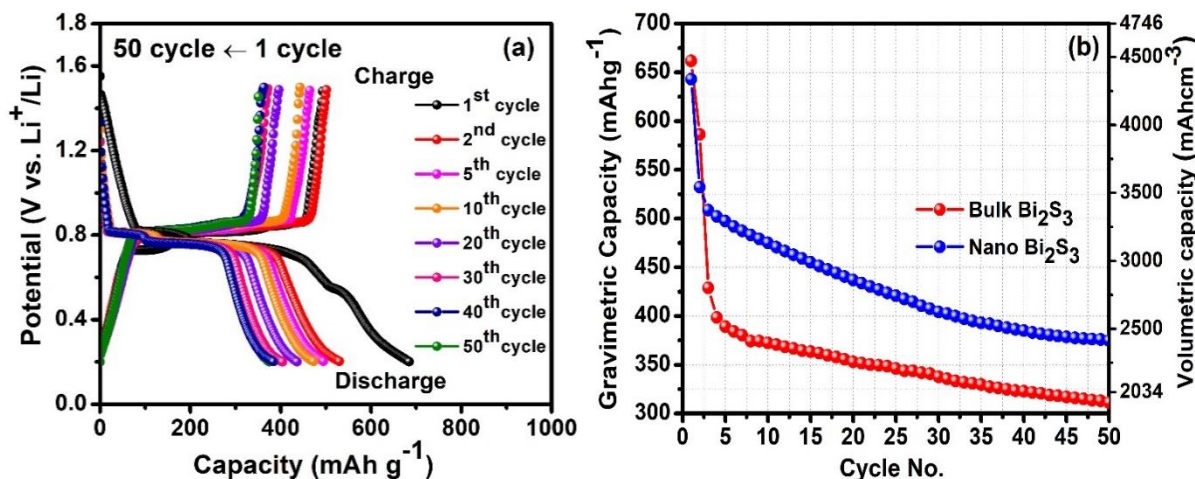


Figure 6.12: Cyclic performance of the (a) nano Bi_2S_3 - LiBH_4 -AB composite anode material, (b) Cyclic stability (Capacity vs. no. of the cycle) of commercial bulk Bi_2S_3 and Bi_2S_3 nanoflowers.

or comparable to a variety of other Bi_2S_3 nanostructures [98], [172]. After the cycling test of composite electrode material, the SEM was also performed to observe the surface condition of the negative electrode. No cracks or crumbling on the surface of anode material were observed even after 50 cycles (**Figure 6.13**) in contrast to the case of cycling between 0.2 – 2.5V where cracks appeared only after 13 cycles. Even though the thermochemical reaction restricted ourselves to

perform the delithiation/lithiation cycles in a limited potential window of 0.2-1.5V, the prepared nano $\text{Bi}_2\text{S}_3\text{-LiBH}_4\text{-AB}$ composite negative electrode showed the excellent cyclic stability over 50 cycles with no electrode damage.

In order to compare the cyclic performance of nanostructured anode to the bulk anode, a curve between the capacities vs. cycle number is plotted and is shown in **Figure 6.12 (b)**. It is evident that the initial capacity of the bulk sample was slightly higher than the nanocomposite anode material. However, the cyclic stability of the nano $\text{Bi}_2\text{S}_3\text{-LiBH}_4\text{-AB}$ composite anode material was found much better than bulk $\text{Bi}_2\text{S}_3\text{-LiBH}_4\text{-AB}$ composite electrode. The nano $\text{Bi}_2\text{S}_3\text{-LiBH}_4\text{-AB}$ composite anode material showed only 29.5% capacity decay from the first capacity, which is much lower than 47% capacity decay of bulk $\text{Bi}_2\text{S}_3\text{-LiBH}_4$ composite electrode. The possible reasons for the better stability of nanoflowers might include high surface area and excellent charge transfer kinetics of the nanostructures due to the shorter diffusion path.

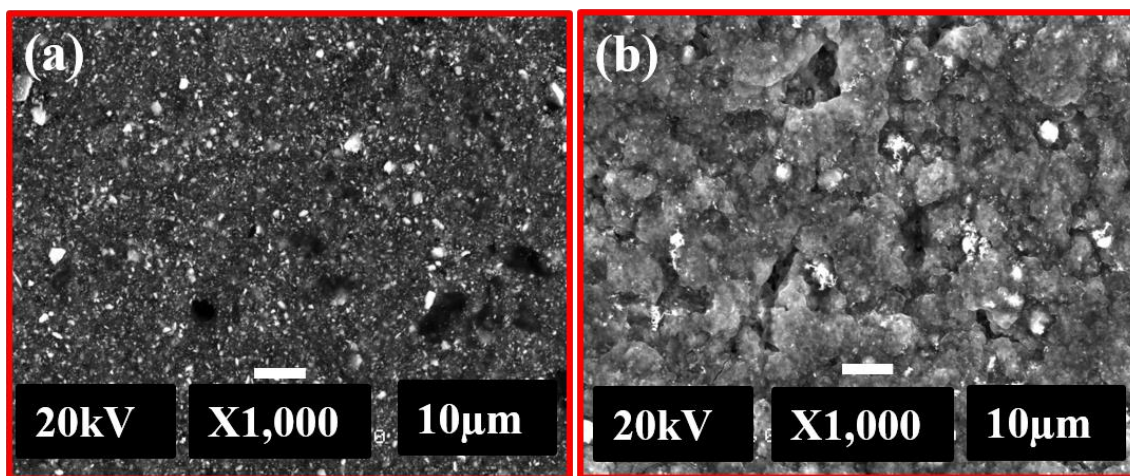


Figure 6.13: FE-SEM images of nano $\text{Bi}_2\text{S}_3\text{-LiBH}_4$ composite anode after galvanostatic electrochemical discharging-charging in the voltage range of 0.2-1.5V (a) 0 cycles and (b) 50 cycles.

For the Bi_2Se_3 nanostructures- $\text{LiBH}_4\text{-AB}$ composite electrode material, the cyclic performance was also evaluated in the potential window of 0.2 – 1.5V at 0.1C (as shown in **Figure 6.14 (a)**), which eliminated the crack formation (**Figure 6.15**). As shown in **Figure 6.14 a**, the first discharge and charge capacity was found to be 594 mAhg^{-1} (with obtained volumetric capacity 4071 mAhcm^{-3}) and 468 mAhg^{-1} respectively, which was faded down to 403 mAhg^{-1} and 384

mAhg⁻¹ in the second cycle due to the limited potential window. The discharge and charge capacity after 50 cycles were found to be 343 mAhg⁻¹ and 340 mAhg⁻¹, respectively. It was evident that the electrode material performed well between 0.2V – 1.5V without any side reactions and showed a highly stable *Li* storage capacity, even though the *Se* ↔ *Li*₂*Se* conversion reaction was not allowed to proceed.

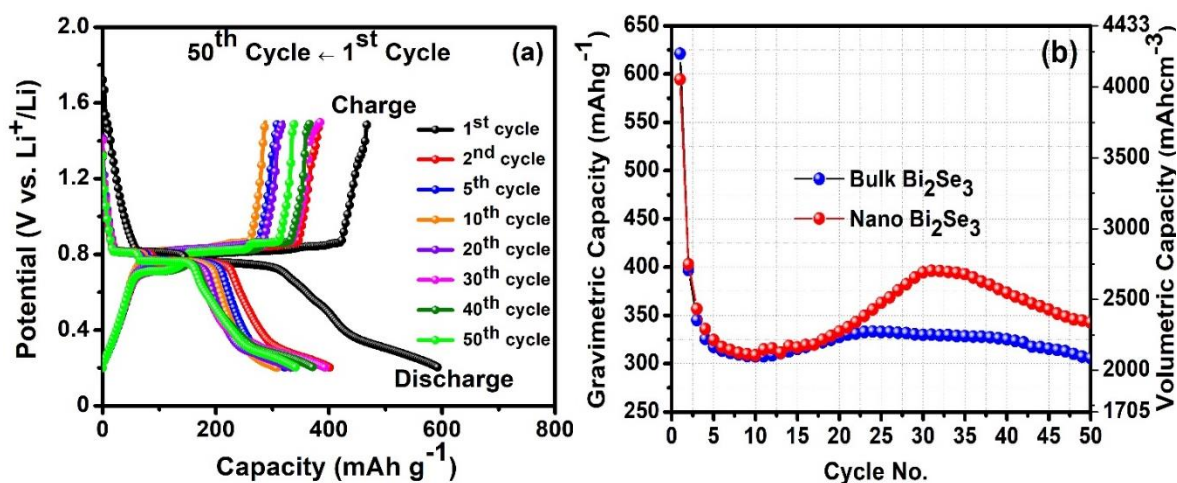


Figure 6.14: Cyclic discharging/charging profile of the (a) *Bi*₂*Se*₃ nanostructures-*LiBH*₄-*AB* composite electrode (b) Cyclic stability (Capacity vs. no. of the cycle) of bulk *Bi*₂*Se*₃ and nano *Bi*₂*Se*₃.

The initial capacity of these nanostructures was less than the commercial bulk sample, which must be due to the complete conversion of nano-*Bi*₂*Se*₃ to *Li*₂*Se* and *Bi* in comparison to the partial conversion of bulk-*Bi*₂*Se*₃ to *Li*₂*Se* and *Bi* as a result of thermochemical electrolyte decomposition. However, the cyclic stability of nano-*Bi*₂*Se*₃ composite electrode was found much better than bulk *Bi*₂*Se*₃ composite electrode with better cyclic stability (**Figure 6.14**) due to the high surface area of the electrode and excellent charge transfer kinetics due to their shorter diffusion path. The nano-*Bi*₂*Se*₃ composite showed only 15% capacity decay from the initial capacity with ~99% coulombic efficiency in potential window 0.2-1.5 V, which is much lower than the 23% capacity decay for the bulk-*Bi*₂*Se*₃ composite electrode. Also, the capacity was found to be increased after 15 cycles and then gradually decreased again. The reason for this unusual behavior is not known completely, but it might be due to some side reaction, which contributed to the overall capacity or may be due

to the anode activation behavior because here anode material has mixed morphology in the form of nanoparticles and nanosheets.

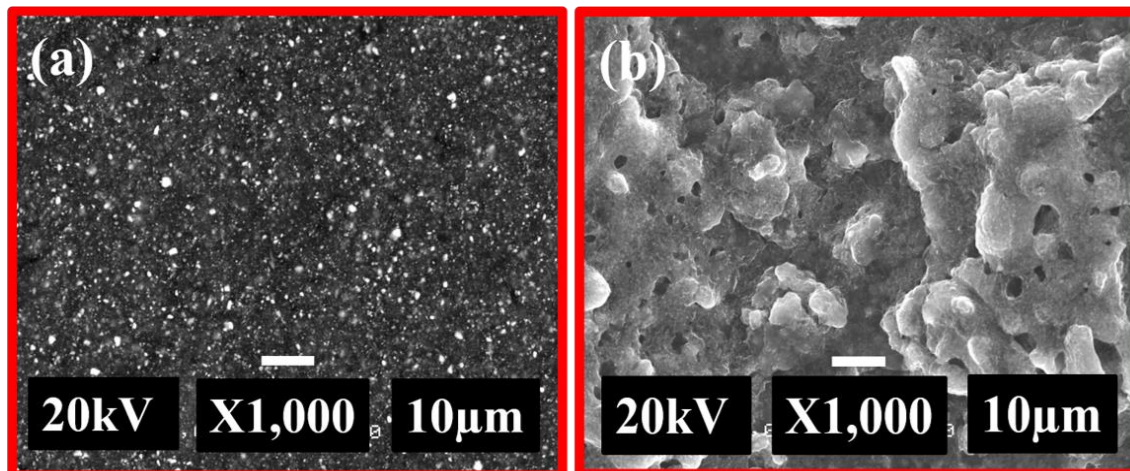


Figure 6.15: FE-SEM images of nano $\text{Bi}_2\text{Se}_3\text{-LiBH}_4\text{-AB}$ composite anode (a) before and (b) after 50 cycles of galvanostatic electrochemical discharging-charging in the voltage range of 0.2-1.5V.

Figure 6.16 (a) shows the discharge/charge curves of the Bi_2Te_3 nanorods- LiBH_4 electrode at 0.1C for 50 cycles and the potential window was kept limited to 0.2-1.5V. The first discharge capacity for the nano- Bi_2Te_3 composite electrode was found to be 489 mAhg^{-1} , which was faded down to 283 mAhg^{-1} in the second cycle due to the limited potential window. The discharge & charge capacities in 50th cycles were found to be 235 mAhg^{-1} & 233 mAhg^{-1} , respectively. Thus the nano- Bi_2Te_3 composite electrode material works well between 0.2 and 1.5 V with a high coulombic efficiency of >95% without any side reactions, which was also confirmed by FE-SEM images as shown in **Figure 6.17**.

On comparing the performance of nanostructured composite with bulk composite electrode, capacity in the 50th cycle was found slightly higher in case of nano than that for bulk Bi_2Te_3 composite electrode (Discharge: 219 mAhg^{-1} & Charge: 218 mAhg^{-1}), which suggested the improved cyclic stability of nano- Bi_2Te_3 composite electrode in comparison to bulk Bi_2Te_3 (**Figure 6.16 b**).

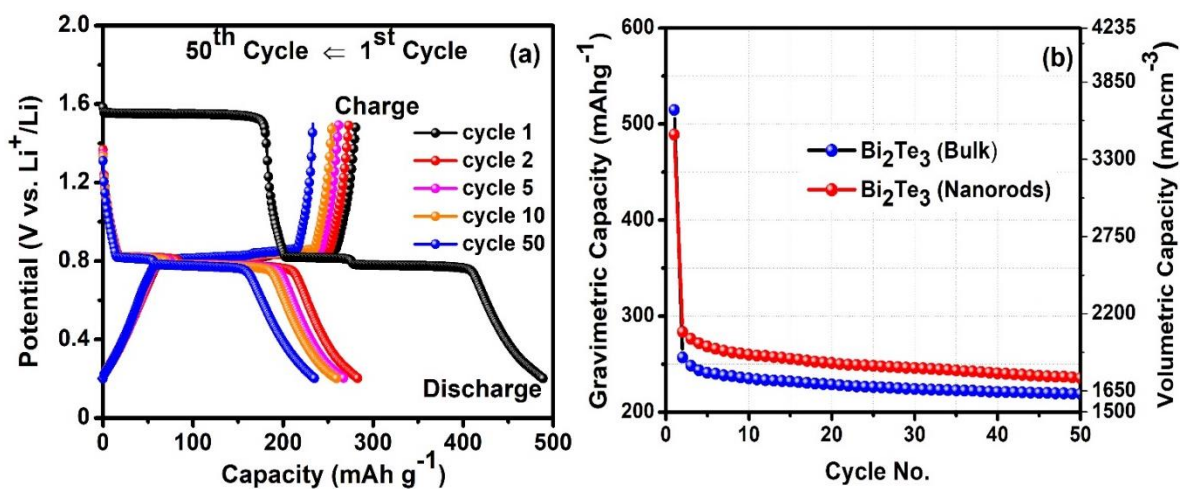


Figure 6.16: (a) Cyclic performance of the Bi_2Te_3 nanorods- LiBH_4 -AB composite electrode (b) (c) Cyclic stability of bulk Bi_2Te_3 (blue curve) and nano Bi_2Te_3 (red curve).

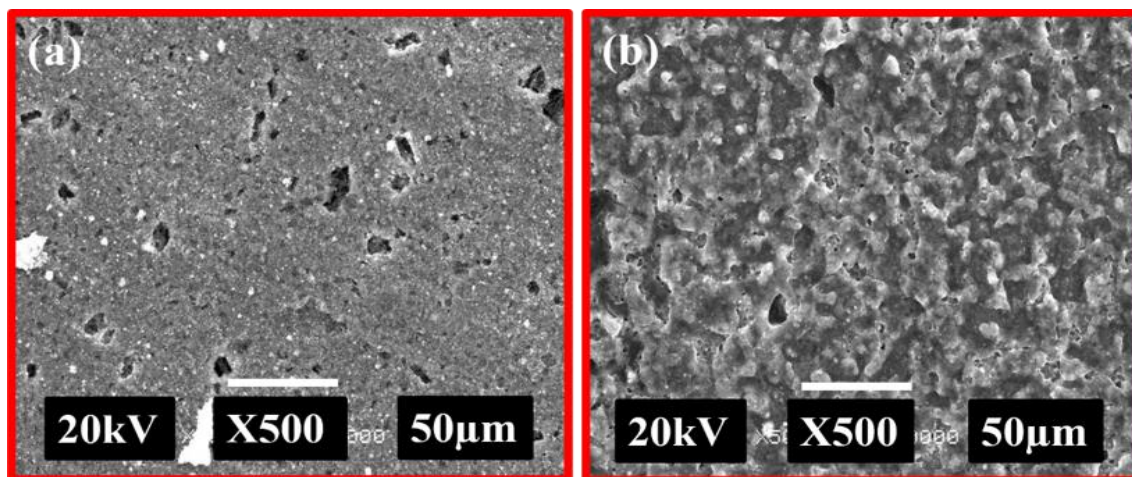


Figure 6.17: FE-SEM images of nano Bi_2Te_3 - LiBH_4 -AB composite anode (a) before and (b) after 50 cycles of galvanostatic electrochemical discharging-charging in the voltage range of 0.2-1.5V.

6.7 Summary

In summary, the present work clarified that the hydrothermally synthesized Bi_2X_3 nanostructures had shown excellent and stable electrochemical performance in all-solid-state *Li*-ion battery. The nanostructured anode has relatively low discharge capacity in the initial cycles compared with commercial bulk Bi_2X_3 anode but showed better cyclic stability over 50 cycles. The values are much higher than the previous reports also (as discussed in **Chapter 2**). An unusual thermochemical reaction between Bi_2X_3 and LiBH_4 was observed for nanostructured anode also similar to that of the bulk electrode during the charging process, which limited the potential window between 0.2 – 1.5 V. Despite this limited potential window, nanostructured electrode attained higher stability and capacity of all-solid-state LIB. The exciting cyclic performance with high capacity, demonstrate the potential of Bi_2X_3 to be used as novel electrode material for *Li*-ion batteries and LiBH_4 as a solid electrolyte.

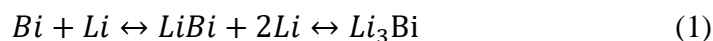
Chapter Seven

Conclusions and Future Scope of Work

7.1 Conclusions

The present thesis focused on establishing the reversible electrochemical mechanism and implementing Bi_2X_3 anode materials in all-solid-state *Li*-ion batteries. An extremely small polarization and outstanding volumetric and gravimetric capacity of *Bi* makes it a promising candidate for the negative electrode in all-solid-state LIBs. In order to enhance the capacity further, *Bi*-based chalcogenides were also successfully employed as anode material. The following conclusions are made based on studies carried out:

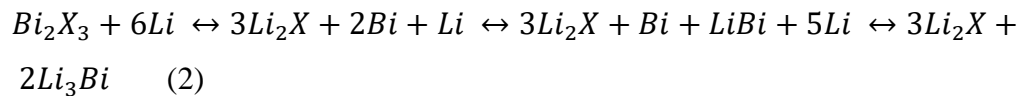
- *Bi* was used as active material in the composite anode having heat-treated LiBH_4 and AB in 40:30:30 weight ratio. The electrochemical performance of the composite electrode was investigated by cyclic voltammetry and galvanostatic discharge-charge measurements at 120°C. The first galvanostatic discharge-charge curves for the *Bi*- LiBH_4 -AB composite electrode between the optimized potential window 0.2 - 1.5 V vs. Li^+/Li at the 0.1C rate exhibited the initial discharge and charge capacity as 4681.7 mAhcm^{-3} (478.7 mAhg^{-1}) and 4510.5 mAhcm^{-3} (461.2 mAhg^{-1}), with an initial coulombic efficiency of 96.3%.
- The *ex-situ* XRD measurements were performed at selected potentials (as obtained by plateau potential through discharging/charging profile) to understand the mechanism behind the obtained plateaus, and based on the XRD results an entirely reversible reaction was obtained between *Bi* and *Li*-ions, as shown in equation 1:



- The cyclic stability of $\text{Bi-LiBH}_4\text{-AB}$ composite anode has also been investigated under 0.2-1.5V for selected no. of cycles up to 100 cycles. The capacity is found to be

decreased down to 3853.3 mAhcm⁻³ (394 mAhg⁻¹) after 100 cycles, which suggest an 82% capacity retention. The stable coulombic efficiency with unchanged plateau potential over no. of cycles also suggest the excellent performance of the coin cell.

- *Bi*-based anode materials exhibit outstanding volumetric capacity and superior stability. The high stability of this system can be attributed to the cushioning effect of LiBH₄ and carbon presented in the composite, which is a feature in addition to their ionic & electrical conductivity, respectively.
- In order to enhance the specific capacity as well as the volumetric capacity of *Bi*-based anode, commercial bulk Bi₂X₃ (X = S, Se, & Te) have been investigated as active material in the anode. All the electrochemical characterizations on Bi₂X₃ electrodes were performed at 0.1C under 0.2-2.5V potential window. Similar to *Bi*-based anode, an electrochemical reaction was established between Bi₂X₃ and *Li*-ion, and based on the *ex-situ* XRD results, the reaction involved in the first charge and discharge verified the excellent reversibility of the alloying reaction. The established electrochemical reversible reaction is shown in equation 2:



- The initial charge capacity of Bi₂X₃ [Bi₂S₃ (discharge: 617 mAhg⁻¹, charge: 1145 mAhg⁻¹), Bi₂Se₃ (discharge: 621 mAhg⁻¹, charge: 1346 mAhg⁻¹), and Bi₂Te₃ (discharge: 515 mAhg⁻¹, charge: 1349 mAhg⁻¹)] was very high as compared to the discharge capacity as well as theoretical capacity, which indicated the occurrence of some side reaction during the charging of coin cell.
- These anode materials exhibit outstanding initial volumetric and gravimetric capacity. The performance of these anode materials is very high with solid electrolyte LiBH₄. However, it reacts with Bi₂X₃ thermochemically during the second step of charging (~1.7 V- 2V), which causes the formation of the cracks on the electrode surface. These cracks result in the loss of physical contact between active material and electrolyte, and thus capacity gradually drops over several numbers of cycles.

- To avoid this thermochemical reaction and to improve the cyclic stability of bulk Bi_2X_3 based composite electrode, the potential window of electrochemical cycling was kept limited to 0.2 – 1.5 V. From cyclic measurements of bulk Bi_2X_3 - LiBH_4 -AB composite anode, it can be clearly observed that the limited potential window gives better stability as compared to previously used potential window as 0.2-2.5V. For Bi_2S_3 - LiBH_4 -AB, first discharge and charge capacity were found as 662 mAhg^{-1} and 524 mAhg^{-1} , respectively. The initial capacity reduced down to 311 mAhg^{-1} and 225 mAhg^{-1} respectively, with the 47% capacity decay from the first capacity. In case of Bi_2Se_3 - LiBH_4 -AB composite anode material depicted a high discharge capacity about 621 mAhg^{-1} in the first cycle, which is faded down to 397 mAhg^{-1} in the second cycle due to the limited potential window and does not allow the $\text{Se} \leftrightarrow \text{Li}_2\text{Se}$ conversion. The capacity finally reached 306 mAhg^{-1} after 50 cycles, which suggest only 23% capacity decay in 50 cycles. Similarly, the bulk Bi_2Te_3 - LiBH_4 -AB composite electrode delivers a high discharge capacity of 533 mAhg^{-1} in the first cycle, which was faded down to a quite stable discharging/charging capacity with 219 mAhg^{-1} in 50th cycle, which suggest only 15% capacity decay in 50 cycles. It is evident that the electrode materials perform well between 0.2V – 1.5V without any side reactions and shows a highly stable *Li* storage capacity than the other available reports.
- The limited potential window also suppresses the formation of the crack on the surface of anode material during discharging/charging cycles in contrast to what was observed in the case of 0.2-2.5V potential window.
- In order to further enhance the stability, Bi_2X_3 nanostructures (Bi_2S_3 nanoflowers, Bi_2Se_3 mixed morphology as nanoparticles & nanosheets, and Bi_2Te_3 nanorods) were synthesized by hydrothermal/solvothermal method.
- The FESEM and TEM image of as-prepared Bi_2S_3 sample depicted the flower-like pattern and also exhibited that each shoot in this pattern was formed along with a well-arranged assembly between many nanorods. The nanorods have a variation in the diameter as 10 – 150 nm with the length in the range of 150 – 400 nm.
- The SEM and TEM experiments were performed on the prepared Bi_2Se_3 sample, and the obtained morphological information about the product described that the prepared sample had mixed morphology of nanoparticles and nanosheets. The particle size is

calculated in the range of 20 nm-150 nm, whereas the thickness of the nanosheets was found in the range of 5 – 30 nm.

- Morphological investigation of prepared Bi_2Te_3 product revealed the successful synthesis of nanorods, which had the variation in length and diameter in a range of 50-400 nm and 20-70 nm, respectively.
- Nanostructured Bi_2X_3 electrode exhibits outstanding volumetric capacity ($\text{Bi}_2\text{S}_3 \rightarrow 4488 \text{ mAhcm}^{-3}$, $\text{Bi}_2\text{Se}_3 \rightarrow 4071 \text{ mAhcm}^{-3}$, & $\text{Bi}_2\text{Te}_3 \rightarrow 4104 \text{ mAhcm}^{-3}$), gravimetric capacity ($\text{Bi}_2\text{S}_3 \rightarrow 662 \text{ mAhg}^{-1}$, $\text{Bi}_2\text{Se}_3 \rightarrow 594 \text{ mAhg}^{-1}$ & $\text{Bi}_2\text{Te}_3 \rightarrow 533 \text{ mAhg}^{-1}$ with superior stability.
- A comparable cyclic study between the bulk electrode and nanostructured electrode was also investigated, and the present work clarified that the hydrothermally synthesized Bi_2X_3 nanostructures had shown excellent and stable electrochemical performance in all-solid-state LIBs. The nanostructured anode has relatively low discharge capacity in the initial cycles compared with commercial bulk Bi_2X_3 anode but shows the better cyclic stability over 50 cycles.
- Despite this limited potential window, Bi_2X_3 nanostructured electrode attained higher stability and capacity of all-solid-state LIB. The exciting cyclic performance with high capacity, demonstrate the potential of Bi_2X_3 to be used as novel electrode material for *Li*-ion batteries and LiBH_4 as a solid electrolyte.

7.2 Future Scope of Work

Based on the findings in the present thesis, the future scope of the work can be proposed as follows:

- Although the performance of these anode materials is very high with solid electrolyte LiBH_4 , it reacts with Bi_2X_3 during the second step of charging, thus limit the cyclic test between 0.2 – 1.5 V, hence reduce the available capacity. It would be interesting to explore these anode materials with other solid electrolytes, *e.g.* , $\text{Li}_2\text{S-P}_2\text{S}_5$, in order

to allow the cycling for the full range, *i.e.*, 0.2 – 2.5V. It may enhance the deliverable capacity as well as the cyclic stability to a much higher value.

- Since LiBH_4 has low ionic conductivity at room temperature and can provide high conductivity with a high-temperature phase, it would be interesting to stabilize its high-temperature phase at relatively mild temperatures. It will allow using these systems at near ambient temperature. It would also solve the problem associated with the thermochemical reaction as Bi_2X_3 react with LiBH_4 thermochemically only at high temperature.
- Herein, Bi_2Te_3 , Bi_2Se_3 , & Bi_2S_3 were used as an anode material; there is a possibility to use their intermixture as a negative electrode to improve their electrochemical performance.
- Fabrication of half coin cell by *Bi*-based anode material approach has been discussed here. So, the same method can be applied for the other chalcogenides, *e.g.* , *Sb* based materials can provide much higher capacity.
- Finally, the optimized system can be employed to *Na*-ion batteries.

References:

- [1] G. Girishkumar, B. Mccloskey, A. C. Luntz, S. Swanson, and W. Wilcke, “Lithium-Air Battery: Promise and Challenges”, *J. Phys. Chem. Lett.*, 1 (2010) 2193–2203.
- [2] A. M. Omer, “Energy and Environment: Applications and Sustainable Development”, *International Journal of Environment and Climate Change*, 1 (2011) 118–158.
- [3] P. Garg, “Energy Scenario and Vision 2020 in India”, *Journal of Sustainable Energy & Environment*, 3 (2012) 7-17.
- [4] D. L. Klass, “A Critical Assessment of Renewable Energy Usage in the USA”, *Energy Policy*, 31 (2003) 353–367.
- [5] A. Demirbas, “Progress and Recent Trends in Biodiesel Fuels”, *Energy Convers. Manag.*, 50 (2009) 14–34.
- [6] S. Dunn, “Hydrogen Futures: Toward a Sustainable Energy System”, *Int. J. Hydrogen Energ.*, 27 (2020) 235–264.
- [7] X. Yan and R. J. Crookes, “Energy Demand and Emissions from Road Transportation Vehicles in China”, *Prog. Energy Combust. Sci.*, 36 (2010) 651–676.
- [8] T. F. Yi, S. Y. Yang, H. T. Ma, X. Y. Li, Y. Q. Ma, H. B. Qiao *et al.*, “Effect of Temperature on Lithium-ion Intercalation Kinetics of $\text{LiMn}_{1.5}\text{Ni}_{0.5}\text{O}_4$ -Positive Electrode Material”, *Ionics*, 20 (2014) 309-314.
- [9] S. Huang, Z. Wen, X. Yang, Z. Gu, and X. Xu, “Improvement of the High-Rate Discharge Properties of LiCoO_2 with the Ag Additives”, *J. Power Sources*, 148 (2005) 72–77.
- [10] R. Rashidi, I. Dincer, G. F. Naterer, and P. Berg, “Performance Evaluation of Direct Methanol Fuel Cells for Portable Applications”, *J. Power Sources*, 187 (2009) 509–516.
- [11] K. Meisterling, “Life Cycle Assessment of Greenhouse Gas Emissions From Plug-in Hybrid Vehicles: Implications for Policy”, *Environ. Sci. Technol.*, 42 (2008) 3170–3176.
- [12] M. Armand and J.-M. Tarascon, “Building Better Batteries”, *Nature*, 451 (2008) 652–657.
- [13] B. Dunn, H. Kamath, and J. Tarascon, “Electrical Energy Storage For the Grid: A Battery of Choices”, *Science*, 334 (2011) 928–936.
- [14] S. J. Harris, A. Timmons, D. R. Baker, and C. Monroe, “Direct in Situ Measurements of *Li* Transport in *Li*-ion Battery Negative Electrodes”, *Chem. Phys. Lett.*, 485 (2010) 265–274.

- [15] A. M. Bernardes, D. C. R. Espinosa, and J. A. S. Tenório, “Recycling of Batteries: A Review of Current Processes and Technologies”, *J. Power Sources*, 130 (2004) 291–298.
- [16] Q. Zhang, S. D. Astorg, P. Xiao, X. Zhang, and L. Lu, “Carbon-Coated Fluorinated Graphite for High Energy and High Power Densities Primary Lithium Batteries”, *J. Power Sources*, 195 (2010) 2914–2917.
- [17] D. Lisbona and T. Snee, “A Review of Hazards Associated with Primary Lithium and Lithium-ion Batteries”, *Process Saf. Environ. Prot.*, 89 (2011) 434–442.
- [18] Z. Chen, Z. Lu, and J. R. Dahn, “Staging Phase Transitions in Li_xCoO_2 ”, *Journal of the Electrochemical Society*, 149 (2002) 1604–1609.
- [19] M. Park, X. Zhang, M. Chung, G. B. Less, and A. Marie, “A Review of Conduction Phenomena in *Li*-ion Batteries”, *J. Power Sources*, 195 (2010) 7904–7929.
- [20] J. Y. Song, Y. Y. Wang, and C. C. Wan, “Review of Gel-Type Polymer Electrolytes for Lithium-Ion Batteries”, *J. Power Sources*, 77 (1999) 183–197.
- [21] E. Environ, V. Etacheri, R. Marom, R. Elazari, G. Salitra, and D. Aurbach, “Environmental Science Challenges in the Development of Advanced *Li*-ion Batteries: A Review”, *Energy Environ. Sci.*, 4 (2011) 3243–3262.
- [22] J. Schwenzel, V. Thangadurai, and W. Weppner, “Developments of High-Voltage All-Solid-State Thin-Film Lithium ion Batteries”, *J. Power Sources*, 154 (2006) 232–238.
- [23] F. Cheng, J. Liang, Z. Tao, and J. Chen, “Functional Materials for Rechargeable Batteries”, *Advanced Materials*, 94 (2011) 1695–1715.
- [24] M. Morris and S. Tosunoglu, “Survey of Rechargeable Batteries for Robotic Applications”, *Florida Conference on Recent Advances in Robotics*, 2012 (1-9).
- [25] M. Morris and S. Tosunoglu, “Comparison of Rechargeable Battery Technologies”, *ASME Early Career Technical Conference*, (2012) 1-8.
- [26] J. Zhang and J. Lee, “A Review on Prognostics and Health Monitoring of *Li*-Ion Battery”, *J. Power Sources*, 196 (2011) 6007–6014.
- [27] J. Chen, “Recent Progress in Advanced Materials for Lithium Ion Batteries”, *Materials (Basel)*, 10 (2013) 156–183.
- [28] S. Goriparti, E. Miele, F. De Angelis, E. Di, R. Proietti, and C. Capiglia, “Review on Recent Progress of Nanostructured Anode Materials for *Li*-Ion Batteries”, *J. Power Sources*, 257 (2014) 421–443.

- [29] R. Chandrasekaran, A. Magasinski, G. Yushin and T.F. Fuller, “Analysis of Lithium Insertion / Deinsertion in a Silicon Electrode”, *Electrochemical Society*, 157 (2010) 1139-1151.
- [30] B. H. Li, Z. Wang, L. Chen, and X. Huang, “Research on Advanced Materials for *Li*-ion Batteries”, *Adv. Mater.*, 21 (2009) 4593–4607.
- [31] F. Yang, F. Yu, Z. Zhang, K. Zhang, Y. Lai, and J. Li, “Bismuth Nanoparticles Embedded in Carbon Spheres as Anode Materials for Sodium/Lithium-ion Batteries”, *Chemistry a European Journal*, 22 (2016) 2333–2338.
- [32] J. Ni, X. Bi, Y. Jiang, L. Li, and J. Lu, “Bismuth Chalcogenide Compounds Bi_2X_3 ($\text{X} = \text{O}, \text{S}, \text{Se}$): Applications in Electrochemical Energy Storage”, *Nano Energy*, 34 (2017) 356–366.
- [33] H. Yin, Q. Li, M. Cao, W. Zhang, H. Zhao, C. Li *et al.*, “Nanosized-Bismuth-Embedded 1D Carbon Nanofibers as High-Performance Anodes for Lithium-Ion and Sodium-Ion”, *Nano Research*, 10 (2017) 2156–2167.
- [34] Y. Zhong, B. Li, S. Li, S. Xu, Z. Pan, Q. Huang *et al.*, “*Bi* Nanoparticles Anchored in N-Doped Porous Carbon as Anode of High Energy Density Lithium Ion Battery”, *Nano-Micro Lett.*, 10 (2018) 56 (1-14).
- [35] Y. Zhao and A. Manthiram, “High-Capacity, High-rate Bi-Sb Alloy Anodes for Lithium-Ion and Sodium-Ion Batteries”, *Chemistry of Materials*, 27 (2015) 3096-3101.
- [36] C. Julien, I. Sararas, and A. Chevy, “Studies of Lithium Insertion in Bismuth Chalcogenide Compounds”, *Solid State Ionics*, 36 (1989) 113–120.
- [37] G. Han, Z. G. Chen, D. Ye, L. Yang, L. Wang, J. Drennan *et al.*, “In-Doped Bi_2Se_3 Hierarchical Nanostructures as Anode Materials for *Li*-Ion Batteries”, *J. Mater. Chem. A*, 2 (2014) 7109.
- [38] Z. Ali, C. Cao, J. Li, Y. Wang, T. Cao, M. Tanveer *et al.*, “Effect of Synthesis Technique on Electrochemical Performance of Bismuth Selenide”, *J. Power Sources*, 29 (2013) 216–222.
- [39] F. Tu, J. Xie, G. Cao, and X. Zhao, “Self-Assembly of Bi_2Te_3 -Nanoplate/Graphene-Nanosheet Hybrid by One-Pot Route and its Improved *Li*-Storage Properties”, *Materials*, 5 (2012) 1275–1284.

- [40] M. Song, S. Park, F. M. Alamgir, J. Cho, and M. Liu, “Nanostructured Electrodes for Lithium-Ion and Lithium-Air Batteries: The Latest Developments, Challenges, and Perspectives”, *Mater. Sci. Eng. R*, 72 (2011) 203–252.
- [41] K. Zaghib, K. Striebel, A. Guerfi, J. Shim, M. Armand, and M. Gauthier, “LiFePO₄/Polymer/Natural Graphite: Low Cost Li-Ion Batteries”, *Electrochimica Acta*, 50 (2004) 263–270.
- [42] K. Amine, R. Kanno, Y. Tzeng, and G. Editors, “Rechargeable Lithium Batteries and Beyond : Progress, Challenges, and Future Directions”, *MRS Bulletin*, 39 (2019) 395–401.
- [43] T. Eriksson, "LiMn₂O₄ as a Li-ion Battery Cathode: From Bulk to Electrolyte Interface", (2001).
- [44] D. Aurbach, B. Morkovsky, G. Salitra, E. Markevich, Y. Talyossed, M. Koltypin *et al.*, “Review on Electrode - Electrolyte Solution Interactions, Related to Cathode Materials for Li-ion Batteries”, *J. Power Sources*, 165 (2007) 491–499.
- [45] W. Zhang, “Structure and Performance of LiFePO₄ Cathode Materials: A review”, *J. Power Sources*, 196 (2011) 2962–2970.
- [46] N. Nitta, F. Wu, J. T. Lee, and G. Yushin, “Li-ion Battery Materials: Present and Future”, *Biochem. Pharmacol.*, 18 (2015) 252–264.
- [47] M. Marcinek, J. Syzdek, M. Marczewski, M. Piszcs, L. Niedzicki, M. Kalita *et al.*, “Electrolytes for Li-ion transport – Review”, *Solid State Ionics*, 276 (2015) 107–126.
- [48] A. Guerfi, M. Dontigny, P. Charest, M. Petitclerc, M. Lagace, A. Vijn *et al.*, “Improved Electrolytes for Li-Ion Batteries : Mixtures of Ionic Liquid and Organic Electrolyte with Enhanced Safety and Electrochemical Performance”, *J. Power Sources*, 195 (2010) 845–852.
- [49] N. Yoshimoto, Y. Niida, M. Egashira, and M. Morita, “Nonflammable Gel Electrolyte Containing Alkyl Phosphate for Rechargeable Lithium Batteries”, *J. Power Sources*, 163 (2006) 238–242.
- [50] Z. Florjan, C. Monikowska, W. Wiczorek, A. Ryszawy, A. Tomaszewska, K. Fredman *et al.*, “Polymer-in-Salt Electrolytes Based on Acrylonitrile / Butyl Acrylate Copolymers and Lithium Salts”, *J. Phys. Chem. B*, 108 (2004) 14907–14914.

- [51] T. Fukunaga, T. Hazama, M. Terasaki, M. Mizutani, and M. Yamachi, “Degradation Mechanism of Alkyl Carbonate Solvents used in Lithium-Ion Cells During Initial Charging”, *J. Power Sources*, 68 (1997) 311–315.
- [52] S. Shiraki, H. Oki, Y. Takagi, T. Suzuki, A. Kumatani, R. Shimizu, *et al.*, “Fabrication of All-Solid-State Battery using Epitaxial LiCoO₂ Thin Films”, *J. Power Sources*, 267 (2014) 881–887.
- [53] B. Kim, K. Takada, N. Ohta, and Y. Seino, “All Solid State Li-Ion Secondary Battery with FeS Anode”, *Solid State Ionics*, 176 (2005) 2383–2387.
- [54] E. Quartarone, and P. Mustarelli, “Electrolytes for Solid-State Lithium Rechargeable Batteries: Recent Advances and Perspectives”, *Chem. Soc. Rev.*, 40 (2011) 2525–2540.
- [55] M. Tatsumisago and A. Hayashi, “Sulfide Glass-Ceramic Electrolytes for All-Solid-State Lithium and Sodium Batteries”, *International Journal of Applied Glass Science*, 235 (2014) 226–235.
- [56] S. Stramare and W. Weppner, “Structure and Conductivity of B-site Substituted (Li, La) TiO₃”, *Materials Science and Engineering B*, 113 (2004) 85–90.
- [57] R. Murugan, V. Thangadurai, and W. Weppner, “Fast Lithium Ion Conduction in Garnet-Type Li₇La₃Zr₂O₁₂”, *Angew. Chem. Int. Ed.*, 46 (2007) 7778–7781.
- [58] E. Hanc, W. Zaj, and J. Molenda, “Synthesis Procedure and Effect of Nd, Ca and Nb Doping on Structure and Electrical Conductivity of Li₇La₃Zr₂O₁₂ Garnets”, *Solid State Ionics*, 262 (2014) 617–621.
- [59] F. Zheng, M. Kotobuki, S. Song, M. O. Lai, and L. Lu, “Review on Solid Electrolytes for All-Solid-State Lithium-Ion Batteries”, *J. Power Sources*, 389 (2018) 198–213.
- [60] J. C. Bachman, S. Muy, A. Grimaud, H. H. Chang, N. Pour, S. F. Lux *et al.*, “Inorganic Solid-State Electrolytes for Lithium Batteries: Mechanisms and Properties Governing Ion Conduction”, *Chem. Rev.*, 116 (2016) 140–162.
- [61] P. E. de Jongh, D. Blanchard and M. Matsuo, T. J. Udovic, and S. Orimo, “Complex Hydrides as Room-Temperature Solid Electrolytes for Rechargeable Batteries”, *Appl. Phys. A*, 122 (2016) 1–6.
- [62] M. Matsuo and S. I. Orimo, “Lithium Fast-Ionic Conduction in Complex Hydrides: Review and Prospects”, *Adv. Energy Mater.*, 1 (2011) 161–172.

- [63] M. Matsuo, Y. Nakamori, S. I. Orimo, H. Maekawa, and H. Takamura, “Lithium Superionic Conduction in Lithium Borohydride Accompanied by Structural Transition”, *Appl. Phys. Lett.*, 91 (2007) 1-4.
- [64] K. Kawahito, L. Zeng, T. Ichikawa, H. Miyaoka, and Y. Kojima, “Electrochemical Performance of Titanium Hydride for Bulk-Type All-Solid-State Lithium-Ion Batteries”, *Materials Transactions*, 57 (2016) 755–757.
- [65] L. Zeng, T. Ichikawa, K. Kawahito, H. Miyaoka, and Y. Kojima, “Bulk-Type All-Solid-State Lithium-Ion Batteries: Remarkable Performances of Carbon Nanofiber Supported MgH₂ Composite Electrode”, *ACS Applied Materials & Interfaces*, 9 (2017) 2261-2266.
- [66] L. Zeng, K. Kawahito, S. Ikeda, T. Ichikawa, H. Miyaoka, and Y. Kojima, “Metal Hydride-Based Materials towards High Performance Negative Electrodes for All-Solid-State Lithium-Ion Batteries”, *Chem. Commun.*, 51 (2015) 9773-9776.
- [67] H. Yin, M. L. Cao, X. X. Yu, H. Zhao, Y. Shen, C. Li *et al.*, “Self-Standing Bi₂O₃ Nanoparticles/Carbon Nanofiber Hybrid Film as a Binder-Free Anode for Flexible Sodium-ion Batteries”, *Mater. Chem. Front.*, 1 (2017) 1615-1621.
- [68] M. Mao, C. Cui, M. Wu, M. Zhang, T. Gao, and X. Fan *et al.*, “Flexible ReS₂ Nanosheets/N-doped Carbon Nano Fibers-based Paper as a Universal Anode for Alkali (Li, Na, K) Ion Battery”, *Nano Energy*, 45 (2018) 346–352.
- [69] J. Liang, C. Yuan, H. Li, K. Fan, Z. Wei and H. Sun *et al.*, “Growth of SnO₂ Nanoflowers on N-doped Carbon Nanofibers as Anode for Li- and Na-ion Batteries”, *Nano-Micro Lett.*, 10 (2018) 1–9.
- [70] M. Endo, C. Kim, K. Nishimura, T. Fujino, and K. Miyashita, “Recent Development of Carbon Materials for Li-Ion Batteries”, *Carbon*, 38 (2000) 183–197.
- [71] Z. Huang, Z. Gong, Q. Kang, X. Yang, R. Liu, X. Lin *et al.*, “High Rate Li-Ion Storage Property of MOFs-Carbonized Derivatives Coating on MnO Nanowires”, *Mater. Chem. Front.*, 1 (2013) 1-3.
- [72] S. Liu, H. Jia, L. Han, J. Wang, P. Gao and D. Xu *et al.*, “Nanosheet-Constructed Porous TiO₂-B for Advanced Lithium Ion Batteries”, *Advanced Materials*, 24 (2012) 3201–3204.

- [73] Y. Zhang, Q. Wang, B. Wang, Y. Mei, and P. Lian, “N-doped Graphene / Bi Nanocomposite with Excellent Electrochemical Properties for Lithium-Ion Batteries”, *Ionics*, 23 (2017) 1407-1415.
- [74] C. M. Park, J. H. Kim, H. Kim, and H. J. Sohm, “Li-Alloy Based Anode Materials for Li Secondary Batteries”, *Chem. Soc. Rev.*, 39 (2010) 3115-3141.
- [75] V. Thangadurai, S. Narayanan, and D. Pinzaru, “Garnet-Type Solid-State Fast Li-ion Conductors for Li Batteries : Critical Review”, *Chem. Soc. Rev.*, 43 (2014) 4714–4727.
- [76] J. Lau, R. H. Deblock, D. M. Butts, D. S. Ashby, C. S. Choi, and B. S. Dunn, “Sulfide Solid Electrolytes for Lithium Battery Applications”, *Adv. Energy Mater.*, 8 (2018) 1800933(1–24).
- [77] F. Han, Y. Zhu, X. He, Y. Mo, and C. Wang, “Electrochemical Stability of Li₁₀GeP₂S₁₂ and Li₇La₃Zr₂O₁₂ Solid Electrolytes”, *Adv. Energy Mater.*, 6 (2016) 1–9.
- [78] M. Matsuo, Y. Nakamori, S. Orimo, H. Maekawa *et al.*, “Lithium Superionic Conduction in Lithium Borohydride Accompanied by Structural Transition”, *Appl. Phys. Lett.*, 91 (2007) 224103 (1-3).
- [79] J. Cabana, T. V. Solis, M. R. Palacin, J. O. Sole, A. Fuertes and G. Marban *et al.* “Enhanced High Rate Performance of LiMn₂O₄ Spinel Nanoparticles Synthesized by a Hard-Template Route”, *J. Power Sources*, 166 (2007) 492–498.
- [80] C. M. Park, S. Yoon, S. I. Lee, and H. J. Sohn, “Enhanced Electrochemical Properties of Nanostructured Bismuth-based Composites for Rechargeable Lithium Batteries”, *J. Power Sources*, 186 (2009) 206–210.
- [81] R. Dai, Y. Wang, P. Da, H. Wu, M. Xu, and G. Zheng, “Indirect Growth of Mesoporous Bi@C Core-Shell Nanowires for Enhanced Lithium-ion Storage”, *Nanoscale*, 6 (2014) 13236–13241.
- [82] J. Lan, Y. Jin, C. Qin, Y. Yu, and X. Yang, “Bio-Inspired Rose-Like Bi @ Nitrogen-Enriched Carbon towards High-Performance Lithium-Ion Batteries”, *Chemistry Select*, 2 (2017) 7178–7184.
- [83] L. Hou, L. Lian, L. Zhang, G. Pang, and C. Yuan, “Self-Sacrifice Template Fabrication of Hierarchical Mesoporous Bi-Component-Active ZnO/ZnFe₂O₄ Sub Microcubes as Superior Anode Towards High-Performance Lithium-Ion Battery”, *Adv. Funct. Mater.*, 25 (2015) 238-246.

- [84] G. Chen, Y. Yu, K. Zheng, T. Ding, W. Wang, Y. Jiang *et al.*, “Fabrication of Ultrathin Bi₂S₃ Nanosheets for High-Performance, Flexible, Visible-NIR Photodetectors”, *Small*, 11 (2015) 2848–2855.
- [85] G. Konstantatos, L. Levina, J. Tang, and E. H. Sargent, “Sensitive Solution-Processed Bi₂S₃ Nanocrystalline Photodetectors”, *Nano Lett.*, 8 (2008) 4002–4006.
- [86] D. Becerra, M. T. S. Nair, and P. K. Nair, “Analysis of a Bismuth Sulfide/Silicon Junction for Building Thin Film Solar Cells”, *J. Electrochem. Soc.*, 158 (2011) 741-749.
- [87] A. K. Rath, M. Bernechea, L. Martinez, and G. Konstantatos, “Solution-Processed Heterojunction Solar Cells Based on p-type PbS Quantum Dots and n-type Bi₂S₃ Nanocrystals”, *Adv. Mater.*, 23 (2011) 3712–3717.
- [88] C. Tang, Y. Zhang, J. Su, C. Wang, and R. Sun, “Synthesis and Photocatalytic Properties of Vertically Aligned Bi₂S₃ Platelets”, *Solid State Sci.*, 51 (2016) 24–29.
- [89] J. Chen, S. Qin, G. Song, T. Xiang, F. Xin, and X. Yin, “Shape-Controlled Solvothermal Synthesis of Bi₂S₃ for Photocatalytic Reduction of CO₂ to Methyl Formate in Methanol”, *Dalt. Trans.*, 42 (2013) 15133–15138.
- [90] Y. Fang, C. Peng, R. Guo, L. Zheng, J. Qin, and B. Zhou *et al.*, “Dendrimer-Stabilized Bismuth Sulfide Nanoparticles: Synthesis, Characterization, and Potential Computed Tomography Imaging Applications”, *Analyst*, 138 (2013) 3172–3180.
- [91] B. Zhang, X. Ye, W. Hou, Y. Zhao, and Y. Xie, “Biomolecule-Assisted Synthesis and Electrochemical Hydrogen Storage of Bi₂S₃ Flowerlike Patterns with Well-Aligned Nanorods”, *J. Phys. Chem. B*, 110 (2006) 8978–8985.
- [92] Q. Wang, X. Wang, W. Lou, and J. Hao, “Ionothermal Synthesis of Bismuth Sulfide Nanostructures and their Electrochemical Hydrogen Storage Behavior”, *New J. Chem.*, 34 (2010) 1930–1935.
- [93] Y. Zhao, D. Gao, J. Ni, L. Gao, J. Yang, and Y. Li, “One-Pot Facile Fabrication of Carbon-Coated Bi₂S₃ Nanomeshes with Efficient Li-Storage Capability”, *Nano Res.*, 7 (2014) 765-773.
- [94] Y. Zhao, T. Liu, H. Xia, L. Zhang, J. Jiang, M. Shen *et al.*, “Branch-Structured Bi₂S₃-CNT Hybrids with Improved Lithium Storage Capability”, *J. Mater. Chem. A*, 2 (2014) 13854-13858.

- [95] H. Jung, C. Park, and H. Sohn, “Bismuth Sulfide and its Carbon Nanocomposite for Rechargeable Lithium-Ion Batteries”, *Electrochim. Acta*, 56 (2011) 2135-2139.
- [96] H. Zhou, S. Xiong, L. Wei, B. Xi, Y. Zhu, and Y. Qian, “Acetylaceton-Directed Controllable Synthesis of Bi_2S_3 Nanostructures with Tunable Morphology,” *Cryst. Growth Des.*, 9 (2009) 3862-3867.
- [97] Z. Zhang, C. Zhou, H. Lu, M. Jia, Y. Lai, and J. Li, “Facile Synthesis of Dandelion-like Bi_2S_3 Microspheres and Their Electrochemical Properties for Lithium-ion Batteries”, *Mater. Lett.*, 91(2013) 100-102.
- [98] J. Ma, Z. Liu, J. Lian, X. Duan, T. Kim, P. Peng *et al.*, “Ionic Liquids-Assisted Synthesis and Electrochemical Properties of Bi_2S_3 Nanostructures”, *Cryst. Eng. Comm*, 13 (2011) 3072–3079.
- [99] W. Liu, K. C. Lukas, K. M. Enaney, S. Lee, Q. Zhang, C. P. Opeil *et al.*, “Studies on the Bi_2Te_3 - Bi_2Se_3 - Bi_2S_3 System for Mid-Temperature Thermoelectric Energy Conversion”, *Energy Environ. Sci.*, 6 (2013) 552–560.
- [100] Y. Sun, H. Cheng, S. Gao, Q. Liu, Z. Sun, C. Xiao *et al.*, “Atomically-thick Bismuth Selenide Freestanding Single-layers Achieving Enhanced Thermoelectric Energy Harvesting”, *J. Am. Chem. Soc.*, 134 (2012) 20294.
- [101] J. Cha, M. Classen, D. Kong, S. Hong, K. Koski, X. Qi *et al.*, “Effects of Magnetic Doping on Weak Antilocalization in Narrow Bi_2Se_3 Nanoribbons”, *Nano Letter*, 12 (2012) 1–5.
- [102] H. Zhang, C. X. Liu, X. L. Qi, X. Dai, Z. Fang, and S. C. Zhang, “Topological Insulators in Bi_2Se_3 , Bi_2Te_3 and Sb_2Te_3 with a Single Dirac Cone on the Surface”, *Nat. Phys.*, 5 (2009) 438–442.
- [103] Y. Zhang, K. He, C. Chang, C. Song, L. Wang and Xi Chen *et al.*, “Crossover of the Three-Dimensional Topological Insulator Bi_2Se_3 to the Two-Dimensional Limit”, *Nat. Phys.*, 6 (2010) 584–588.
- [104] D. Kong, K. J. Koski, J. J. Cha, S. S. Hong, and Y. Cui, “Ambipolar Field Effect in *Sb*-Doped Bi_2Se_3 Nanoplates by Solvothermal Synthesis”, *Nano Lett.*, 13 (2013) 632–636.
- [105] H. He, B. Li, H. Liu, X. Guo, Z. Wang and M. Xie *et al.*, “High-field Linear Magneto-Resistance in Topological Insulator Bi_2Se_3 Thin Films”, *Appl. Phys. Lett.*, 100 (2012) 032105 (1-3).

- [106] P. Larson, V. A. Greanya, W. C. Tonjes, R. Liu, S. D. Mahanti, and C. G. Olson, “Electronic Structure of Bi_2X_3 ($\text{X}=\text{S}, \text{Se}, \text{Te}$) Compounds: Comparison of the Theoretical Calculations with Photoemission Studies”, *Phys. Rev. B*, 65 (2002) 085108 (1-11).
- [107] H. Xu, G. Chen, R. Jin, D. Chen, Y. Wang and J. Pei *et al.*, “Microwave-Assisted Synthesis of Bi_2Se_3 Ultrathin Nanosheets and its Electrical Conductivities”, *Cryst. Eng. Comm.*, 16 (2014) 3965–3970.
- [108] H. Xu, G. Chen, R. Jin, J. Pei, Y. Wang, and D. Chen, “Hierarchical Bi_2Se_3 Microrods: Microwave-Assisted Synthesis, Growth Mechanism and Their Related Properties”, *Cryst. Eng. Comm.*, 15 (2013) 1618-1625.
- [109] R. Jin, J. Liu, Y. Xu, G. Li, G. Chen, and L. Yang, “Hierarchical $\text{Bi}_2\text{Se}_{3-x}\text{S}_x$ Microarchitectures Assembled from Ultrathin Polycrystalline Nanosheets: Solvothermal Synthesis and Good Electrochemical Performance”, *J. Mater. Chem. A*, 1 (2013) 10942–10950.
- [110] X. Chen, H. Tang, Z. Huang, J. Zhou, X. Ren, and K. Huang, “Flexible Bismuth Selenide /Graphene Composite Paper for Lithium-Ion Batteries”, *Ceram. Int.*, 43 (2017) 1437–1442.
- [111] D. Zhang, B. S. Haran, A. Durairajan, R. E. White, Y. Podrazhansky, and B. N. Popov, “Studies on Capacity Fade of Lithium-Ion Batteries”, *J. Power Sources*, 91 (2000) 122–129.
- [112] D. Liu and G. Cao, “Engineering Nanostructured Electrodes and Fabrication of Film Electrodes for Efficient Lithium Ion Intercalation”, *Energy Environ. Sci.*, 3 (2010) 1218-1237.
- [113] J. M. Tarascon and M. Armand “Issues and Challenges Facing Rechargeable Lithium Batteries”, *Materials for Sustainable Energy*, 414 (2010) 171-179.
- [114] J. B. Goodenough and Y. Kim, “Challenges for rechargeable *Li* batteries”, *Chem. Mater.*, 22 (2010) 587–603.
- [115] K. Xu, “Electrolytes and Interphases in *Li*-ion Batteries and Beyond”, *Chem. Rev.*, 114 (2014) 11503-11618.
- [116] Y. Wang and W. Zhong, “Development of Electrolytes towards Achieving Safe and High-Performance Energy-Storage Devices : A Review”, *Chem. Electro. Chem*, 105 (2014) 1–16.

- [117] A. Manthiram, X. Yu, and S. Wang, “Lithium Battery Chemistries Enabled”, *Nat. Publ. Gr.*, 2 (2017) 1–16.
- [118] H. Wang, H. Cao, W. Zhang, J. Chen, H. Wu, C. Pistidda *et al.*, “Li₂NH-LiBH₄: A Complex Hydride with Near Ambient Hydrogen Adsorption and Fast Lithium Ion Conduction”, *Chem. Eur. J.*, 23 (2017) 1–7.
- [119] M. Matsuo, A. Remhof, P. Martelli, R. Caputo, M. Ernst, Y. Miura *et al.*, “Complex Hydrides with (BH₄) and (NH₂) - Anions as New Lithium Fast-Ion Conductors”, *J. Am. Chem. Soc.*, 131 (2009) 16389–16391.
- [120] H. Oguchi, M. Matsuo, T. Sato, H. Takamura, H. Maekawa, H. Kuwano, *et al.*, “Lithium-Ion Conduction in Complex Hydrides LiAlH₄ and Li₃AlH₆”, *Journal of Applied Physics*, 107 (2010) 4-7.
- [121] M. B. Ley, D. B. Ravnsbæk, Y. Filinchuk, Y. Lee, R. Janot, Y. Cho, *et al.*, “LiCe(BH₄)₃Cl, a New Lithium-Ion Conductor and Hydrogen Storage Material with Isolated Tetranuclear Anionic Clusters”, *Chem. Mater.*, 24 (2012) 1654-1663.
- [122] K. Takahashi, K. Hattori, T. Yamazaki, K. Takada, and M. Matsuo, “All-Solid-State Lithium Battery with LiBH₄ Solid Electrolyte”, *J. Power Sources*, 226 (2013) 61–64.
- [123] A. Ha, N. Berti, P. López-Aranguren, J. Zhang, F. Cuevas, C. Jordy *et al.*, “Electrochemical Properties of MgH₂ – TiH₂ Nanocomposite as Active Materials for All-Solid-State Lithium Batteries”, *J. Power Sources*, 397 (2018) 143–149.
- [124] P. Huen and D. B. Ravnsbæk, “All-Solid-State Lithium Batteries – The Mg₂FeH₆-Electrode LiBH₄-Electrolyte System”, *Electrochem. Commun.*, 87 (2018) 81-85.
- [125] L. Farina, S. Brutti, F. Trequattrini, O. Palumbo, S. Gatto, P. Reale *et al.*, “An extensive study of the Mg-Fe-H material obtained by reactive ball milling of MgH₂ and Fe in a molar ratio 3:1”, *Int. J. Hydrogen Energy*, 42 (2017) 22333–22341.
- [126] W. Zaïdi, J. P. Bonnet, J. Zhang, F. Cuevas, M. Latroche and S. Couillaud *et al.*, “Reactivity of Complex Hydrides Mg₂FeH₆, Mg₂CoH₅ and Mg₂NiH₄ with Lithium Ion : Far from Equilibrium Electrochemically Driven Conversion Reactions”, *Int. J. Hydrogen Energy*, 38 (2013) 4798-4808.
- [127] S. Z. Mengfei Zhu, Y. Pang, F. Lu, X. Shi, J. Yang, “In Situ Formed Li-B-H Complex with High Li-ion Conductivity as Potential Solid Electrolyte for Li Batteries”, *Appl. Mater. Interfaces*, 11 (2019) 1-22.

- [128] F. Lu, Y. Pang, M. Zhu, F. Han, J. Yang and F. Fang *et al.*, “A High-Performance Li–B–H Electrolyte for All-Solid-State *Li* Batteries”, *Adv. Funct. Mater.*, 29 (2019) 1809219 (1–7).
- [129] C. J. Tang, Y. X. Zhang, X. C. Dou, and G. H. Li, “Seed-Assistant Hydrothermal Synthesis of 3D Bi₂S₃ Matlike Architecture”, *J. Cryst. Growth*, 312 (2010) 692–697.
- [130] J. R. Ota, P. Roy, S. K. Srivastava, R. P. Biro, and R. Tenne, “A Simple Hydrothermal Method for the Growth of Bi₂Se₃ Nanorods”, *Nanotechnology*, 17 (2006) 1700–1705.
- [131] H. J. Kim, M. K. Han, H. Y. Kim, W. Lee, and S. J. Kim, “Morphology Controlled Synthesis of Nanostructured Bi₂Te₃”, *Bull. Korean Chem. Soc.*, 33 (2012) 3977–3980.
- [132] J. I. Goldstein, D. E. Newbury, P. Echlin, D. C. Joy, C. Fiori, and E. Lifshin, "Electron-Beam-Specimen Interactions: Scanning Electron Microscopy and X-ray Microanalysis", (1981).
- [133] B. Fultz, J. Howe, "Transmission Electron Microscopy and Diffractometry of Materials", (2012).
- [134] A. Guinier, "X-ray Diffraction in Crystals, Imperfect Crystals, and Amorphous Bodies", (1994).
- [135] A. R. Stokes and A. C. Wilson, “A Method of Calculating the Integral Breadths of Debye-Scherrer Lines”, *Mathematical Proceedings of the the Cambridge Philosophical Society*, 38 (1942) 313-322.
- [136] A. S. Feiner and A. J. McEvoy, “The Nernst Equation”, 71 (1994) 493–494.
- [137] P. T. Kissinger, W. Lafayette, and W. R. Heineman, “Cyclic Voltammetry”, *Journal of Chemical Education*, 60 (1983) 702–706.
- [138] S. Pang, J. Farrell, J. Du, and M. Barth, “Battery State-of-Charge Estimation”, *Proceedings of the American Control Conference*, 5 (2001) 1644–1649.
- [139] P. Knauth, “Inorganic Solid *Li*-ion Conductors : An Overview”, *Solid State Ionics*, 180 (2009) 911–916.
- [140] K. Takada, “Progress and Prospective of Solid-State Lithium Batteries”, *Acta Mater.*, 61 (2013) 759–770.
- [141] S. Sartori, F. Cuevas, and M. Latroche, “Metal Hydrides used as Negative Electrode Materials for *Li*-Ion Batteries”, *Appl. Phys. A*, 122 (2016) 122-135.

- [142] M. Yoshio, H. Wang, and K. Fukuda, “Spherical Carbon-Coated Natural Graphite as a Lithium - Ion Battery Anode Material”, *Angew. Chem.*, 115 (2003) 4335–4338.
- [143] Y. Guo, Y. Wei, H. Li, and T. Zhai, “Layer-Structured Materials for Advanced Energy Storage”, *Small*, 13 (2017) 1–22.
- [144] P. Kumari, K. Sharma, P. Pal, M. Kumar, T. Ichikawa, and A. Jain, “Highly Efficient & Stable Bi & Sb Anodes Using Lithium Borohydride as Solid Electrolyte in Li-ion Batteries”, *RSC Advances*, 9 (2019) 13077–13081.
- [145] J. B. Goodenough and K. Park, “The Li-ion Rechargeable Battery : A Perspective”, *J. Am. Chem. Soc.* 135 (2013) 1167-1176.
- [146] R. Singh, P. Kumari, R. K. Rathore, K. Shinzato, T. Ichikawa and A. S. Verma *et al.*, “LiBH₄ as Solid Electrolyte for Li-Ion Batteries with Bi₂Te₃ Nanostructured Anode”, *Int. J. Hydrogen Energy*, 43 (2018) 21709–21714.
- [147] X. Li, Z. Yang, Y. Fu, L. Qiao, D. Li, H. Yue *et al.*, “Germanium Anode with Excellent Lithium Storage Performance in a Germanium/Lithium-Cobalt Oxide Lithium ion Battery”, *ACS Nano*, 9 (2015) 1858-1867.
- [148] C. Yim, E. A. Baranova, F. M. Courtel, Y. A. Lebdeh, and I. J. Davidson, “Synthesis and Characterization of Macroporous Tin Oxide Composite as an Anode Material for Li-ion Batteries”, *J. Power Sources*, 196 (2011) 9731–9736.
- [149] G. Keskar, E. Iyyamperumal, A. Hitchcock, J. He, A. M. Rao, and L. D. Pfefferle, “Significant Improvement of Thermoelectric Performance in Nanostructured Bismuth Networks”, *Nano Energy*, 1 (2012) 706–713.
- [150] D. Su, S. Dou, and G. Wang, “Bismuth: A New Anode for the Na-ion Battery”, *Nano Energy*, 12 (2015) 88–95.
- [151] Y. Shao, M. Gu, X. Li, Z. Nie, P. Zuo, G. Li *et al.*, “ Highly Reversible Mg Insertion in Nanostructured Bi for Mg - ion Batteries”, *Nano Lett*, 14 (2014) 255-260.
- [152] A. Finke, P. Poizot, C. Guéry, L. Dupont, P. L. Taberna, P. Simon *et al.*, “Electrochemical Method for Direct Deposition of Nanometric Bismuth and Its Electrochemical Properties vs Li⁺”, *J. Electrochem. Soc.*, 165 (2018) 167-182.
- [153] J. Ma, J. Yang, L. Jiao, T. Wang, J. Lian, X. Duan *et al.*, “Bi₂S₃ Nanomaterials: Morphology Manipulation and Related Properties”, *Dalton Trans.*, 40 (2011) 10100–10108.

- [154] C. V Subban, G. Rousse, R. Vannier, and C. Laberty-robert, "Search for *Li*-Electrochemical Activity and *Li*-ion Conductivity Among Lithium Bismuth Oxides", *Solid State Ionics*, 283 (2015) 68–74.
- [155] P. Kumari, K. Awasthi, T. Ichikawa, M. Kumar, A. Jain, "Flower-like Bi₂S₃ Nanostructures as Highly Efficient Anode for All Solid State Lithium Ion Battery", *RSC Advances*, (2019) (Under Review).
- [156] P. Kumari, K. Awasthi, T. Ichikawa, A. Jain, and M. Kumar, "Highly Stable Nanostructured Bi₂Se₃ Anode Material for All Solid-State Lithium Ion Batteries", *Solid State Ionics*, (2019) (Under Review).
- [157] P. Kumari, K. Awasthi, T. Ichikawa, A. Jain, and M. Kumar, "Electrochemical Reaction Mechanism for Bi₂Te₃ Based Anode Material in Highly Durable All Solid State Lithium Ion Batteries", *Journal of Alloys and Compounds* (2019) (Under Review).
- [158] P. Kumari, K. Sharma, P. K. Singh, K. Awasthi, A. Jain, and M. Kumar, "The Destabilization of LiBH₄ Through the Addition of Bi₂Se₃ Nanosheets", *Int. J. Hydrogen Energy*, (2019) (Under Review).
- [159] P. Kumari, P. Pal, K. Shinzato, K. Awasthi, T. Ichikawa, A. Jain, and M. Kumar, "Nanostructured Bi₂Te₃ as Anode Material as well as a Destabilizing Agent for LiBH₄", *Int. J. Hydrogen Energy*, XX (2019) XX-XX (In Press).
- [160] R. Marom, S. F. Amalraj, N. Leifer, D. Jacob, and D. Aurbach, "A Review of Advanced and Practical Lithium Battery Materials", *J. Mater. Chem*, 21 (2011) 9938–9954,.
- [161] B. Scrosati, and J. Garche, "Lithium Batteries : Status, Prospects and Future", *J. Power Sources*, 195 (2010) 2419–2430.
- [162] T. Kim, J. Park, S. K. Chang, S. Choi, J. H. Ryu, and H. Song, "The Current Move of Lithium Ion Batteries Towards the Next Phase", *Adv. Energy Mater*, 2 (2012) 860–872.
- [163] N. A. Kaskhedikar, and J. Maier, "Lithium Storage in Carbon Nanostructures", *Adv. Mater.*, 21 (2009) 2664–2680.
- [164] K. Persson, V. A. Sethuraman, L. J. Hardwick, Y. Hinuma, Y. S. Meng, A. Ven *et al.*, "Lithium Diffusion in Graphitic Carbon", *J. Phys. Chem. Lett.*, 1 (2010) 1176–1180.
- [165] M. Winter, J. O. Besenhard, M. E. Spahr, and P. Novák, "Insertion Electrode Materials for Rechargeable Lithium Batteries", *Adv. Mater.*, 10 (1998) 725–763.

- [166] I. Kim, G. E. Blomgren, and P. N. Kumta, "Sn/C Composite Anodes for Li-Ion Batteries", *Electrochem. Solid-State Lett.*, 7 (2004) 44-48.
- [167] Y. Idota, T. Kubota, A. Matsufuji, Y. Maekawa, and T. Miyasaka, "Tin-Based Amorphous Oxide : A High-Capacity Lithium-Ion-Storage Material", *Science*, 275 (2012)1395-1397.
- [168] Z. Deng, T. Liu, T. Chen, J. Jiang, W. Yang, J. Guo *et al.*, "Enhanced Electrochemical Performances of Bi₂O₃/rGO Nanocomposite via Chemical Bonding as Anode Materials for Lithium Ion Batteries", *ACS Applied Materials & Interfaces*, 9 (2017) 12469-12477.
- [169] Z. Li, W. Zhang, Y. Tan, J. HU, S. He, A. Stein *et al.*, "Three-Dimensionally Ordered Macroporous β -Bi₂O₃ with Enhanced Electrochemical Performance in a Li-ion Battery", *Electrochim. Acta*, 214 (2016) 103–109.
- [170] P. M. Ette, K. Selvakumar, S. Murugesan, S. Kumar, and K. Ramesha, "Ordered 1D and 3D Mesoporous Co₃O₄ Structures: Effect of Morphology on Li-Ion Storage and High Rate Performance", *Electrochim. Acta*, 310 (2019) 184-194.
- [171] X. B. Zhao, X. H. Ji, Y. H. Zhang, G. S. Cao, J. P. Tu, "Hydrothermal Synthesis and Microstructure Investigation of Nanostructured Bismuth Telluride Powder", *Applied Physics A*, 80 (2015) 1567–1571.
- [172] Z. Zhang, C. Zhou, H. Lu, M. Jia, Y. Lai, and J. Li, "Facile Synthesis of Dandelion-like Bi₂S₃ Microspheres and Their Electrochemical Properties for Lithium-ion Batteries", *Mater. Lett.*, 91 (2013) 100–102.

List of Publication

1. Rini Singh, **Pooja Kumari**, Rajan K. Rathore, Keita Shinzato, Takayuki Ichikawa, Vibhav K. Saraswat, Kamendra Awasthi, Ankur Jain, and Manoj Kumar,
LiBH₄ as solid electrolyte for *Li*-ion batteries with Bi₂Te₃ nanostructured anode
Published in International journal of Hydrogen Energy, 43 (2018) 21709-21714.
2. **Pooja Kumari**, Khushbu Sharma, Pratibha Pal, Manoj Kumar, Takayuki Ichikawa, and Ankur Jain,
Highly efficient & stable *Bi* & *Sb* anodes using lithium borohydride as solid electrolyte in *Li*-Ion batteries,
Published in RSC advances, 9 (2019) 13077-13081.
3. **Pooja Kumari**, Pratibha Pal, K. Shinzato, K. Awasthi, Takayuki Ichikawa, Ankur Jain, Manoj Kumar,
Nanostructured Bi₂Te₃ as anode material as well as a destabilizing agent for LiBH₄,
Published in International Journal of Hydrogen Energy, 2019
(<https://doi.org/10.1016/j.ijhydene.2019.06.175>).
4. **Pooja Kumari**, Kamendra Awasthi, Takayuki Ichikawa, Ankur Jain, and Manoj Kumar,
Flower-like Bi₂S₃ nanostructures & LiBH₄ system: A highly efficient electrode for all solid state lithium ion battery,
Published in RSC Advances, 9 (2019) 29549-29555.
5. **Pooja Kumari**, Khushbu Sharma, Pankaj Kumar Singh, Kamendra Awasthi, Hiroki Miyaoka, Takayuki Ichikawa, Manoj Kumar, Ankur Jain,
The destabilization of LiBH₄ through the addition of Bi₂Se₃ nanosheets,
Published in International Journal of Hydrogen Energy, 2019.
(<https://doi.org/10.1016/j.ijhydene.2019.09.040>).
6. **Pooja Kumari**, Kamendra Awasthi, Takayuki Ichikawa, Ankur Jain, and Manoj Kumar,
Highly stable nanostructured Bi₂Se₃ anode material for all solid-state lithium-ion batteries,
Under review, Solid State Ionics, 2019.
7. **Pooja Kumari**, Kamendra Awasthi, Takayuki Ichikawa, Ankur Jain, and Manoj Kumar,
Electrochemical reaction mechanism for Bi₂Te₃ based anode material in highly durable all solid – state lithium – ion batteries,
Under review, Journal of Alloys and Compounds, 2019.

Curriculum Vitae

Km. Pooja Kumari

Department of Physics MNIT Jaipur
Rajasthan – 302017, INDIA

Ph: +91 7073502426

Email: malikpooja720@gmail.com,
poojaphysics1991@gmail.com



Personal information

Indian / Female / Single / 20 August, 1991.

Academic Qualification

- 2019 (Pursuing) Ph.D. (Physics) under the supervision of Dr. Manoj Kumar (Assistant Professor, Department of Physics, **Malaviya National Institute of Technology Jaipur, India**) and Dr. Ankur Jain (Associate Professor, **Natural Science Centre for Basic Research and Development, Hiroshima University, Higashi-Hiroshima, Japan**) on the topic entitled “*Bi* and it’s chalcogenides for all solid state *Li*-ion batteries”.
- 2011-2013 M.Sc. (Physics, specialization in Electronics) from R. K. PG College, Shamli, C.C.S. University, Meerut, U.P., India, [71.2%, grade I].
- 2008- 2011 B.Sc. (Phys., Statistics & Math) from R. K. PG College, Shamli, C.C.S. University, Meerut, U.P., India, [68%, grade I].

Language Skills

Mother Tongue: Hindi, **English Proficiency:** Reading, Writing & Speaking – Excellent

Fellowships/Awards Received

- Dec 2018 Best Presentation award in international conference on soft materials.
- July 2015 Research Fellowship from Department of Higher Education, Ministry of Human Resource Development Government of India, MHRD.

Publications

International Journals – 07 (05 Published & 02 Under Review).

Conferences/Workshops

International & National Conferences/Workshops - 17 attended.

